UNIVERSITÀ DEGLI STUDI DELL'AQUILA
DIPARTIMENTO DI INGEGNERIA INDUSTRIALE E DELL'INFORMAZIONE E DI ECONOMIA

Dottorato di Ricerca in Ingegneria Industriale e dell'Informazione e di Economia

Curriculum Ingegneria Meccanica, Energetica e Gestionale

XXXIII ciclo

Titolo della tesi

Thermal energy recovery in ORC-based power unit: experimental and numerical analyses on sliding vane expanders and novel design methodologies

SSD ING-IND/09

Dottorando

Marco Di Bartolomeo

Coordinatore del corso

Prof. Giuseppe Ferri

Tutor

Prof. Roberto Cipollone

A.A. 2019/2020

Ringraziamenti

Ancora un volta mi ritrovo a scrivere dei ringraziamenti al termine di un percorso importante della mia vita. Sono stati tre anni movimentati per molte ragioni e non posso fare a meno di spendere qualche parola per le persone che mi sono state vicino.

Ringrazio il Prof. Roberto Cipollone per avermi guidato in questo percorso e per essere stato sempre foriero di idee e spunti innovativi. I ragazzi del gruppo di ricerca con i quali ho condiviso innumerevoli ore di studio e di lavoro in laboratorio. Gli amici di una vita, Adriano e Roberto, per aver contribuito a quello che sono diventato, non che sia venuto fuori questo grande capolavoro. Emanuele e Marco, amici di cazzotti, per le ore passate dentro e fuori il tatami. Tutti i ragazzi dell'Eagle Fight Team, allievi e amici con i quali ho passato bellissimi momenti di sport. Riprenderemo a viverne di altri. Alla mia famiglia, per avermi supportato e sopportato in questi anni, anche quando ero insopportabile. A Cristina, che da un anno è parte della mia vita e che prova ogni giorno a rendermi più sopportabile. 10^{24}!.

Acknowledgments

Once again I find myself writing acknowledgements at the end of this important period of my life. They've been three eventful years for different reasons and I can not avoid spending some words for the people who stood by me.

I'd like to thank Professor Roberto Cipollone for guiding me through this period and being always full of innovative ideas to develop. The guys of my research group. I spent with them countless hours of study and work in the laboratory. My lifelong friends, Adriano and Roberto, who contributed to make the person I am. Not that it's this great masterpiece. Emanuele and Marco, MMA mates, for the hours spent inside and outside the mats. All the guys of the Eagle Fight Team, students and friends I spent beautiful moments of sport with. We'll have more beautiful ones in the future. My family, for supporting bearing me even when I was unbearable. Finally I want to thank Cristina for being part of my life in the last year, trying to make me more bearable every day. 10^{24}!.

Summary

Organic Rankine Cycle systems represent a promising solution for the recovery of waste heat in Internal Combustion Engines. In such systems a great amount of thermal energy is wasted at different temperature levels in the environment which can be further recovered to increase the overall efficiency.

The main focus of this thesis was the characterization of a sliding vane expander thought for an ORC-based power unit recovering heat from the exhaust gases of a Diesel Engine. The potentialities of a novel intake system consisting in an additional adduction port properly located on the stator have been assessed, analyzing the performances through experimental and numerical activities. The conducted investigation allowed the definition of the advantages and drawbacks of the proposed solution, giving at the same time a thorough description of the fluid-dynamic phenomena characterizing this kind of devices.

The contents of the manuscripts have been divided in the following way: In chapter 1 an introduction on global warming issues has been presented. A special attention has been given to the on the road transport sector focusing on regulations and potential improvement of Internal Combustion Engines through innovative technologies.

Chapter 2 is a thorough review of most relevant studies on Organic Rankine cycles. Main aspects related to working fluid selection criteria, plant layout and components have been investigated. Special attention has been given to evaporators and expanders technologies.

Chapter 3 describes the layout used for the experimental activities. Characteristics of the ORC unit, the engine and measurement instruments have been detailed.

Chapter 4 reports the results of the experimental activity conducted with

the original expander and after the modification introduced for the investigation on the novel intake system. For both options, efficiencies, indicated and mechanical power have been compared.

Chapter 5 describes the numerical model calibrated with the dataset obtained through the experimental campaigns. This instrument has been used to investigate source of losses and analyze the leakage paths contributing to the volumetric efficiency reduction.

In Chapter 6 the numerical model has been used as a design software platform. A new design methodology is proposed for sliding vane rotary expanders with an auxiliary port, showing potential advantages related to the possible downsizing of the machine.

The results of this work show that sliding vane expander performances can be increased through the modifications of the intake of the device. This solution can improve also the reliability and range of operation of the machine, lowering the unit maximum pressure and allowing to elaborate a greater working fluid mass flowrate. An additional advantage can be obtained initially designing a sliding vane expander with a dual port. In this way a sensible downsizing of the device can be achieved reducing weight, size and volume of the machine.

Abstract

Atmospheric CO_2 concentration is increasing rapidly year by year. Most updated data reports that in 2020 its value has reached the unprecedented peak of 414 ppm despite the most recent economic crisis caused by the global pandemic. The accumulation of CO_2 in the atmosphere indeed, is characterized by a complex dynamic nature and small time-scale variations in greenhouse gases emissions do not affect the average CO_2 concentration if not marginally. This aspect involves the need for an energetic transition towards cleaner and more efficient generation systems in the immediate future for a long-term CO_2 limitation in the atmosphere. The maximum concentration set by the Paris Agreement as safeguard limit to avoid severe and irreversible scenarios has been 450 ppm, only 36 ppm above the present concentration. Following a BAU scenario which implies a reference increase close to 2-2.5 ppm per year, before the middle of this century the limit will be reached.

Global energy demand is destined to grow in future years because of the higher living standards and growing access to electricity. Despite this trend, fossil fuel share in the energy mix is still as high as 80 % with solar and wind energy sources and other minor renewable sources accounting for a poor 3%. In this scenario, it is extremely important not only to develop carbon free technologies in all sectors consuming energy but also to improve the efficiency of the existing conversion technologies.

The on the road transportation represents one of the most important sectors to be addressed. Traditionally, the most diffused propulsion system in this sector is constituted by the use of Internal Combustion Engines, (ICEs). In Europe, only the light-duty and heavy-duty vehicles are responsible for 8 % of the total CO_2 emission in 2019. This share increased up to 21 % if passenger cars are considered which takes into account the need of a personal mobility that will be difficult in the short and medium term to modify in a

sensible way. For this reason, more and more stringent regulations have been imposed to circulating vehicles to fulfill severe limitations on specific CO_2 emissions expressed in gCO_2/km and in gCO_2/kWh, depending on passenger and heavy-duty engines. This measure led to the introduction in the ICE's market of vehicles propelled with electrical energy, to reduce fleet average CO_2 specific emissions for each Company of passenger car and light-duty vehicles. However, considering the share of fossil fuel-propelled vehicles and the carbon content of the electricity (which is still greatly dependent on fossil fuels), a real transition toward a sustainable mobility is really far for being achieved. For these reasons, new technologies are needed to increase the energy efficiency of ICEs with the aim to ultimately reduce CO_2 emissions.

Waste Heat Recovery systems have the potential to transform part of the thermal energy streams usually wasted in the atmosphere into useful work and so participate to the propulsion power in a direct or indirect way. It is known that approximately 60% of the chemical energy of the fuel is lost mainly in the exhaust gases and in the cooling circuit. This heat is usually available at low to mid temperature range. Among the different available technologies, conversion systems based on Organic Rankine Cycles (ORCs) appear to be a suitable solution due to their low cost/benefit ratio. In such systems, the thermal energy available (exhaust gases, cooling fluid, oil, EGR cooling) is used to vaporize in a superheated state a high pressure organic working fluid which is subsequently expanded inside an expander, producing mechanical energy. The expander is the most critical component of an ORC-based recovery unit. It has to guarantee good performances in terms of power output and efficiency while ensuring at the same time reliability, ease of operation and safety. Being the control of the ORC-based power unit basically based on organic fluid flow rate changes, the expander has to guarantee an acceptable behavior in a wide range of flow rates. More generally, in a wide range of input conditions being the inlet pressure also depending on flow rate. Two main categories can be distinguished in ORC applications: dynamic and volumetric type expanders. In dynamic ones (turbine), the high pressure fluid expands interacting with the rotating blades: the fluid is accelerated inside the stator passages and it exchanges angular momentum inside the rotating passages, transforming it into mechanical work. In order to reach acceptable efficiencies considering the limited flow rates, a high rotational speed is needed. In addition, they are really sensible to the working

fluid inlet thermodynamic conditions in terms of density and pressure and to the fluid velocity (mass flow rate). The presence of liquid droplet which is a consequence of an insufficient heat exchanged causes damages to the blades and significantly reduces the expansion inside the fixed passages: a reliable control system is strongly needed and flow rate should be kept in a narrow range. On the other hand, volumetric or positive displacement expanders guarantees a higher ease of operation. The expansion is obtained through the evolution of the fluid inside a closed volume which during rotation increases its extent. Lower rotational speeds characterize the rotation of the machine and a really lower sensibility to the inlet thermodynamic conditions. These properties make them the best choice in ORC-based power unit of a small scale applications.

Among the different kind of volumetric expanders, sliding vanes expanders offer a good trade-off between performances, reliability, capability to offset operating conditions. Compared to the other kinds of volumetric machines, main advantages are represented by their simple geometry, compactness, capability to be shaped according to the available space and ease of manufacturing. A good level of maintenance is insured by a moderate lubrication made simply adding lubricating oil inside the machine mixed with the working fluid. On the other hand, they suffer of lower volumetric and mechanical efficiencies which decrease the overall performances of the unit.

In this work a theoretical and experimental activity conducted on an ORC based power unit for the recovery from the exhaust gases of a 3L diesel engine is presented. The recovery unit has been equipped with a sliding vane expander whose performances have been deeply studied to improve volumetric and mechanical efficiency as well as indicated efficiency too. Pressure and temperature sensors have been placed upstream and downstream each component of the recovery unit in order to have a full thermodynamic characterization of the unit. Moreover, three high-frequency piezoresistive pressure transducers have been used to evaluate the pressure evolution inside the expander with the aim to reconstruct the indicated cycle which defines the work exchange between fluid and moving (rotating) vanes. The direct measurement of the mechanical power allowed to set up a procedure to evaluate volumetric, indicated and mechanical efficiencies, so the full performances of the expander . Thanks to a wide testing activity and a deep theoretical prediction of the expander performances, the expander has been modified

in order to improve overall performances represented by the product of the three efficiencies. The application of a second inlet port after the closing of the main one produces a second filling phase improving the volumetric capabilities of the machine. Main by-side effect is also the reduction of the hydraulic resistance of the device which allowed to elaborate a greater working fluid mass flowrate without increasing the expander inlet pressure. For lower flow rates, the double intake port produces a decrease of the inlet pressure at the expander, improving safety and reliability. The result was to increase the range of operation of the expander and the flexibility of the ORC-based unit: this is strongly required considering the frequent off design conditions produced on the recovery unit by the variations of the exhaust gas flow rate and temperature due to engine operation.

A wide set of experimental data have been further elaborated and used to calibrate a theoretical model of the dual inlet port allowing a deep understanding of the indicated and mechanical performances. More generally, the model allowed to understand the different phenomena occurring in the two configurations and the causes of the observed losses having as final goal the improvement of the overall performances of the expander. A thorough analysis of the leakage paths have been conducted showing that the most important leakage happens between adjacent vanes at the blade tips. This leakage is partially recovered because the mass which escapes from one vane to the other, increases the pressure inside the vane. Moreover, the effects of the additional port positioning was deeply examined to further improve the positive effects. The numerical model has been also used as software platform to design the machine. An important aspect was to discover the best diameter/axial length ratio which guarantees, for a fixed mass flow rate, the maximization of the efficiency. The geometrical shaping of the machine influences, in fact, volumetric (filling and emptying of the vanes), indicated (pressure inside the vanes) and mechanical (friction) performances. The study showed that the geometrical optimization (based on global efficiency) is produced by a machine “disk shaped” with respect to a “finger shaped” machine, having both the same geometrical volume of the vanes.

Contents

List of Figures

List of Tables

Chapter 1

Introduction

1.1 Atmospheric carbon dioxide concentration

Nowadays, climate change is the most important challenge humanity has to face. Atmospheric CO_2 concentration has reached in 2019 the unprecedented peak of 409 ppm registering an increase with respect to the previous year of 2.3 ppm. Since the beginning of the measurement in Manua Loa in 1959, an increase of approximately 100 ppm has been observed (Figure 1.1b). The average growth rate has increased from 1.5 ppm/year in the period 1960-1970 to 2.5 ppm/year in the last decade. The results is an exponential increase of atmospheric CO_2. With a Business as Usual (BAU) trend, the limit of 450 ppm will be reached before the middle of the century, with potentially catastrophic consequences caused by the increased average surface temperature. Figure 1.1a shows data reported in [1]. The average concentration of CO_2 in the past 800 thousand years has been reconstructed from the air trapped inside the ice core of Antarctica. Oscillations are caused by glacial eras and warmer periods between them. In the considered range of investigation, the highest peak stood at 300 ppm. It is evident how what is happening nowadays is something the Earth has never experienced in 800 thousand years.

The presence of green-house gases in the atmosphere determines an accumulation of heat which produces a heat imbalance and consequently an increase of the average temperature (figure 1.1c). Compared to the level of 1750, in 2020 the Earth accumulated 3 W/m2 more with a 45 % increase in just 30 years between 1990 and 2020. The result is shown in figure 1.2. The

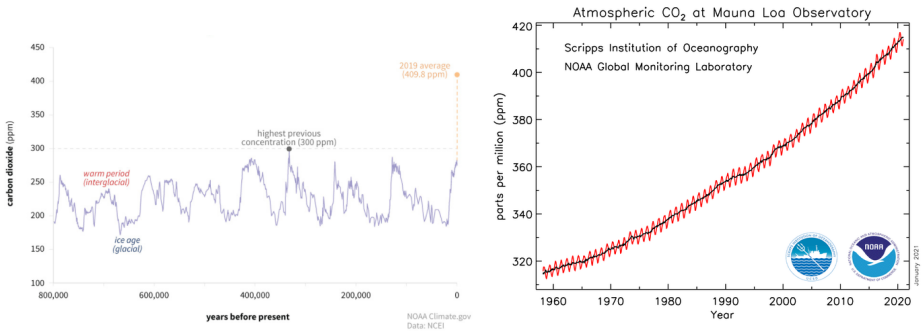

(a)

(b)

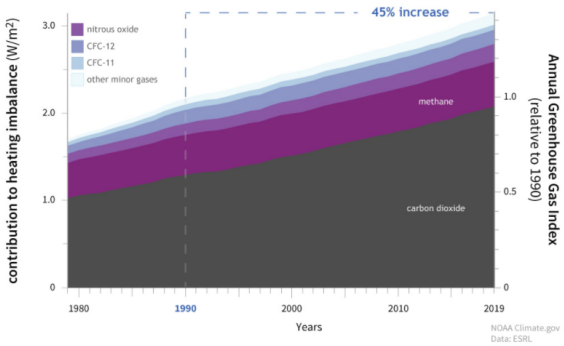

(c)

Figure 1.1: Atmospheric CO_2 concentration [1](a) and (b), heating imbalance (c). (data source: www.esrl.noaa.gov accessed December 2020)

increase in the surface temperature is evaluated as the difference between the average temperature in the 20^{th} century and the yearly average in each year. The figure shows how this temperature anomaly reached 1 °C in the last year with a constant increase starting from 1990.

The Intergovernmental Panel on Climate Change (IPCC) made a point in its 2018 special report on climate change outlining the necessity for pathways to maintain the temperature increase under 1.5 °C in the long term, with overshoots not higher than 2 °C. It is worth observing that a large part of the world population ranging between 20% and 40%, depending on the considered temperature dataset, has already experienced a temperature increase higher than 1.5 °C in at least one season.

The effects of the temperature raise are not straightforward and add up to the ones caused by the atmospheric CO_2 concentration increase itself. Indeed, this latter produces the acidification of the oceans which endangers

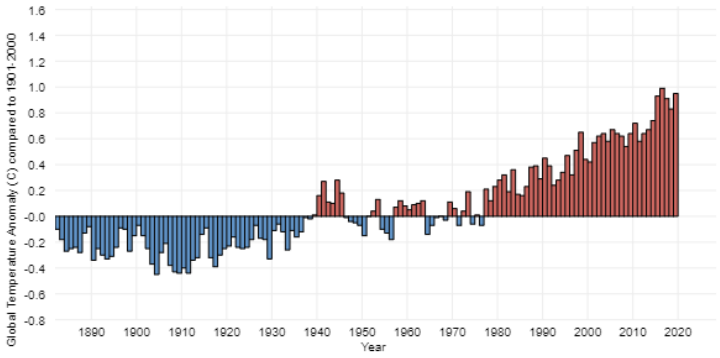

Figure 1.2: Average annual temperature compared to long-term average (1901-2000) (data source :www.climate.gov accessed December 2020).

marine life and varies their carbon uptake, ultimately modifying the carbon cycle. Plant production is also affected by the carbon content of the atmosphere. Temperature increase leads to a greater ocean heat content which causes the destabilization of coastal ice sheets and sea level raise. Moreover, the warmer ocean is responsible for the coral bleaching. Extreme weather events are also increasing in the last decade. A study reported in [2] found that the regional probability in the US Central gulf coast of an extreme three day precipitation increased by 40% due to climate change. Ocean and ambient temperature variations leads also to extreme heat waves [3]. In the study is evidenced how even in the hypothesis of limiting the temperature increase under 1.5 °C, heatwaves like the one reported in [4] (which led to over 700 deaths) can happen every year in India and Pakistan.

Collateral consequences have also an impact on the economy of a region which are usually considered as indirect effects of global warming. Bleaching of corals can reduce tourism in affected areas. Moreover, it has been reported in [5] that the market value of properties near the coast more exposed to sea level rise reduced their value of approximately 10 % in the period between 2010 and 2016 because of the greater awareness of the investors to the global warming issues. Other relevant difficulties are related to the potential impact of ambitious measures taken to face global warming. That is the case for example of biofuels production, either if it is considered for fuel substitution or as a part of bionergy with carbon capture and storage (BECCS) [6]. This solution could potentially cause a land competition which can affect negatively ecosystems.

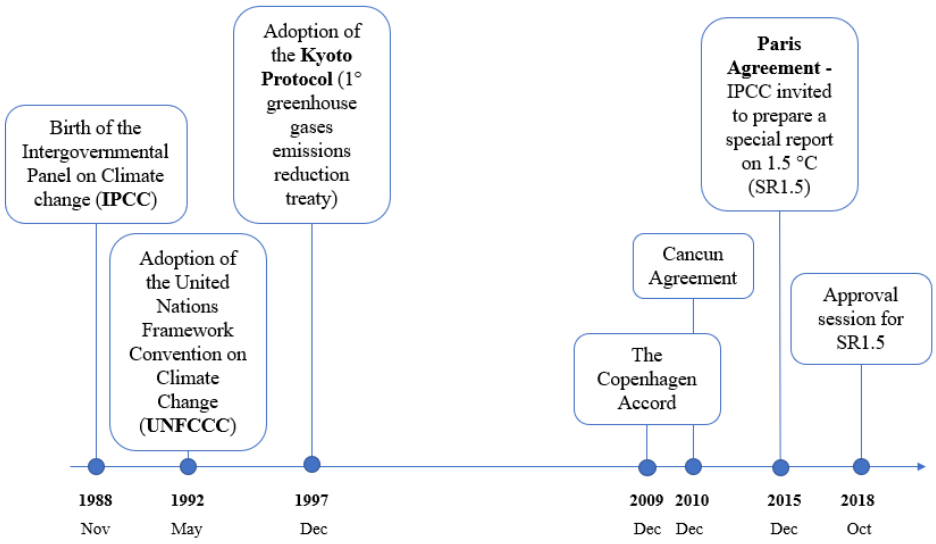

Figure 1.3: Timeline of the most important international agreements on climate change.

1.2 International measures

In order to face the issues related to global warming, several international agreements and cooperations have followed over the years (figure 1.3). Climate change issues have been known for a long time. The Intergovernmental Panel on Climate Change (IPCC) indeed, has been instituted in 1988. Following this first step, the United Nation Framework Convention on Climate Change (UNFCC) has been adopted by multiple parties. The convention claimed for the first time the necessity to limit the average temperature increase. The treaty was not legally mandatory but it opened the possibility for further updates (protocols) to set binding emissions limits. The first protocol was established in 1997 in Kyoto setting binding emissions limits to implement the objectives of the UNFCC on the basis of common but differentiated responsibilities. It became effective in 2005. The greatest part of the adhering Nations respected their limits, also because of the economic crisis of 2009. However, despite the positive results, global greenhouse emissions increased up to 30 % in the same time span. In 2010, during the 16th Conference of Parties (COP), the first document which set the limit of average temperature increase at 2 °C was redacted with the Cancun Agreement. Moreover, a periodical review of the process toward the long-term global goal

is established.

Between 2013 and 2015 the first reviewing process consisted in the Structured Expert Dialogue (SED), a face to face exchange of views between experts and UNFCCC delegates. The final reports assessed that some regions and vulnerable ecosystems will be put in danger for warming above 1.5 °C.

In 2015, during the 21st COP in Paris, the so-called Paris Agreement has been signed by over 190 Parties. The agreement entered into force on November of the following year. With the adoption, the UNFCCC invited the IPCC to provide a special report on climate change which could be used also by policymakers in order to define the most efficient pathways to fulfil the long term global goal of 1.5 °C temperature increase.

1.2.1 The Paris Agreement

The Paris Agreement is an international treaty stipulated by 196 parties in December 2015 and entered into force on November 2016. Main goal of the agreement is to limit global warming under 2 °C and preferably under 1.5 °C compared to pre-industrial levels. In order to achieve this goal, the parties aim to reach the peak of greenhouse gases emission as soon as possible with the intention to achieve a carbon neutrality by the end of mid-century.

This treaty represents a landmark in the climate change challenge since, for the first time, a binding agreement between nations has been stipulated for a common cause. The economic and social transformations needed to implement the Paris Agreement are based on the best available science. The treaty reviewing process is based on a 5 years-cycle in which the actions reported in the Nationally Determined Contributions (NDC) are processed starting from 2020. NDCs are plans in which the parties submit the actions that will be taken in order to limit greenhouse gases emissions. They provide also strategies to build resilience against the inevitable consequences of climate change. Moreover, countries are invited to formulate long term low green house emission development strategies (LT-EDS) starting from 2020. These additional plans are not mandatory as the NDCs, but help providing a direction towards a sustainable future.

Since global warming is a large scale issue, the Paris Agreement offers several instruments to help cooperation between parties. These instruments are needed in order to help vulnerable and economically weaker Nations which are not capable to provide actions strong enough to fulfil their plans.

The support consists of a framework for financial help and transfer and implementation of newer technologies. Moreover, a great emphasis on the support for climate challenge related capacities building is placed.

Progresses are tracked in the enhanced transparency framework (ETF). Under the ETFs, which starts in 2024, parties are invited to report in a transparent way actions taken towards climate change mitigation as well as adaptation measure and support (given or taken). All the informations provided under this framework will be channelled into the Global stocktake which will be useful to observe the efficiency of measures taken by parties. This instrument will help also the reviewing process and the planning of more efficient measures in the following period.

The Paris Agreement correlated the maximum temperature achievable (+ 2°C with respect to pre-industrial levels) with the concentration of CO_2 in the atmosphere: the value is 450 ppm of CO_2 which represents a concentration limit which should not be overpassed. The adoption of this limit, which reflects the need to stay below the + 2°C temperature increase, produces an important concept called "Carbon Budget". This represents the maximum quantity of Carbon which can be emitted in the atmosphere to stay below 450 ppm. The Carbon Budget has important consequences on the future of fossil fuels.

1.3 Primary energy demand

The evolution of primary energy demand can be evaluated as:

$$C(t) = N(t)\, A(t)\, B(t) \tag{1.1}$$

where N represents the total population, A the Gross Domestic Product per capita and B the energy intensity which define the nergy required to produce a unit of GDP. In this sense, the higher is B, the lower is the energy efficiency of a country. From this representation, it is straightforward that in order for the primary energy demand to decrease the energy intensity must reduce at a higher rate with respect to the total population and the GDP. All these quantities can be easily elaborated from statistical data regarding a specific Country and, therefore, aggregations of them.

In addition to that, living standards are destined to increase. An always greater part of the world population is going to have access to electricity and

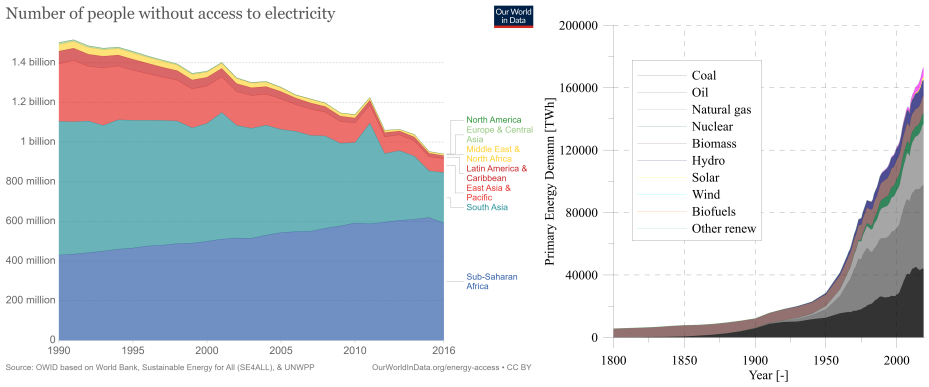

(a) (b)

Figure 1.4: Access to electricity by zone (a) and primary energy consumption by source (b)

increase their energy needs. In 2016, 13 % of people did not have access to electricity which mean one out of seven people. In 1990 the share was 28%, representing 1.5 billion of persons. Even if tremendous improvements have been made in this time span, further actions are needed to guarantee a more sustainable lifestyle to as many people as possible.

Figure 1.4b describes the evolution of the primary energy consumption between the pre-industrial era and 2020 ([7]). In the beginning of the 20$^{\text{th}}$ century, the totality of the energy needs were satisfied through coal. This situation lasted until the mid of the century. After that, first oil and then natural gas were added to the energy mix. Nowadays, despite all the efforts made through the international treaties, the greatest part of the energy demand is still satisfied with fossil fuels. Coal, oil and natural gas combined contribute for over 80 %. The remaining part is represented mainly by nuclear, biomass and hydro with solar and wind energy sources accounting for just 3%. Focusing on the time interval between the Kyoto Protocol (1997) and 2020 the average growth rate of wind and solar energy sources has been 26%. Energy consumption derived from these types of sources increased from 35 TWh to 5333 TWh. Despite this outbreak, numbers are still too low to satisfy a significant part of the energy demand which resulted in a fossil fuel share almost constant between 77% and 80% in the last 30 years. So, the efforts put in place till now to reduce fossil fuel use and to promote renewable energy sources at a global scale gave a very limited contribution.

The results of the aforementioned energy consumption is a increasing

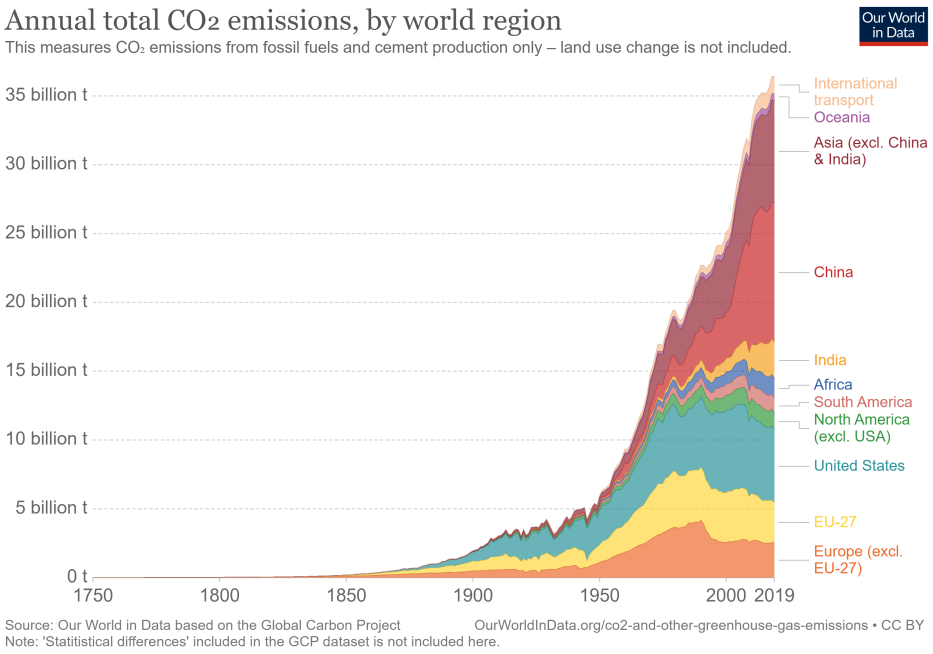

Figure 1.5: Carbon dioxide emissions by country and year

amount of carbon dioxide reversed into the atmosphere. Figure 1.5 shows CO_2 emissions deriving from fossil fuel combustion and cement industry. In 2019, CO_2 emissions amounted at 36.4 Gton. By far, the largest contributors were China and USA, accounting for 28 % and 15% respectively. United States have been the greatest emitter during the 20th century till 2005. After that, the economic growth of China determined the current situation where China is responsible for almost twice the emission of the United States (10.2 Gton against 5.3 Gton).

2019 has shown a 0.2 % increase of CO_2 emissions worldwide compared to the previous year, representing a growth rate much lower than the one registered in the last decade (+1.22%). The Covid-19 pandemic is expected to decrease emission by 7 % in 2020 because of the confinement measures (2.2 Gton CO_2). In order to better understand the meaning of such a reduction, it is worth noting that the observed decrease is much higher than the one evaluated for the second world war in 1945, (-0.9 Gton), the Gulf War in 1992 (-0.7 Gton) and the economic crisis of 2009 (-0.5 Gton).

However, despite the reduction, global emissions are expected to increase to standard levels after this period. Moreover the accumulation of CO_2 in

the atmosphere follows a dynamic response due to the sink capacity of land and oceans [8]. This means that the current atmospheric concentration of carbon dioxide is the product of what has been emitted not only in the previous year, as it would be with an instantaneous dynamic but also in all the years before the considered one. As a result, a time delay between the peak of the emissions and the one of atmospheric CO_2 concentration is expected to occur.

According to the Special Report on 1.5 °C elaborated by the IPCC, the absorption capability of the atmosphere is not endless. With the current rhythm, it is estimated that the remaining cumulative CO_2 emissions that can be accumulated in the atmosphere is about 420 Gton for a 66 % chance to stay under 1.5 °C. For a 50/50 chance the carbon budget increases up to 580 Gton. With the current emission trend, this limit will be reached in just 7 years. This time period increases to 25 years if the threshold is raised up to 2 °C. Even if these predictions are affected by sever uncertainties due to transient climate response to cumulative emissions, they clearly show how important measures are needed in order to avoid the reaching of this limit. These measures need to take into account several aspects related not only to emission reductions actions but also mitigation and adaptation issues.

1.4 Transport sector

The transport sector contributes for approximately 20% to the world primary energy demand, following the industry and the building sector (figure 1.6a and 1.6b). The reasons are explainable considering that, especially the transport on the road, is dominated currently by internal combustion engines propelled by fossil fuels and their derivates.

Compared to other sectors, transport has been much more resistive to adjustments. Making reference to 1990, greeenhouse gases emission continued to grow until 2007, reaching a level in 2014 still 20% higher in Europe (figure 1.6c). Within the transport sector, the greatest contributor to the energy demand and consequently to GHG emissions is the on the road transport which accounts for 73.3 % and 72.8% respectively.

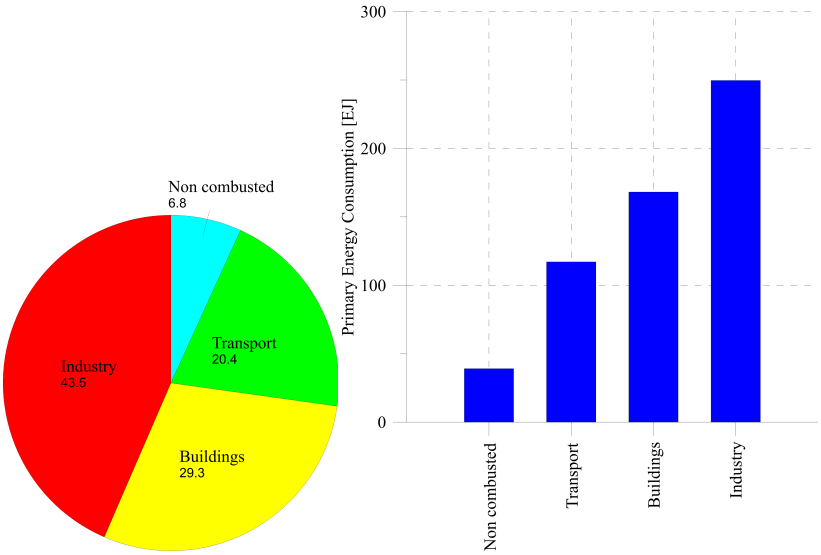

(a) (b)

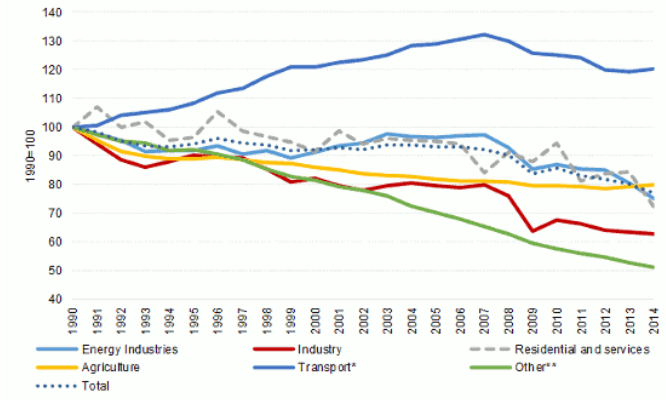

(c)

Figure 1.6: Primary energy consumption by sector in 2018 (BP energy review) and GHG emission evolution compared to 1990 baseline.

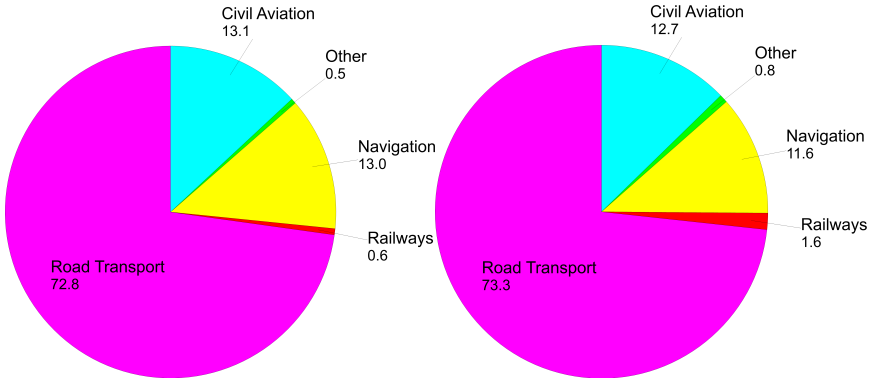

(a) (b)

Figure 1.7: GHG emissions and energy demand share in the transport sector in Europe.)

1.4.1 European regulations

Data collected in the European Union showed that on the Road transport has been responsible in 2017 for 21 % of the overall emissions. 71% of these can be attributed to passenger cars and light duty vans. The remaining part is produced by the heavy duty vehicles.

The European Commission has worked over the years to ensure a progression in the overall efficiencies of vehicles setting always more stringent mandatory limits on specific emissions. The emission limits consist of fleet average emissions. In order to stay under the emission targets, each Company has to ensure that the average of the emissions of vehicles sold is not greater than the binding ones. If this happens, each company pays a fee for each exceeding gram of CO_2 per kilometer on each vehicle sold.

Before 2020, CO_2 emission standards were set through Regulations (EC) 443/2009 [9] for passenger cars. The target was calculated as:

$$CO_{2_{target}} = 130 + a\,(M - M_0) \tag{1.2}$$

where a is a constant coefficient, M the mass of the considered vehicle and M_0 the average mass of vehicles sold in the three previous years. The target CO_2 emissions were measured on the New European Driving Cycle. The regulation became effective starting from 2015. The target was successfully satisfied already in 2013. In 2019 indeed, it has been reported that the average specific emissions in EU28, in Norway and Iceland was 122 g/km.

The fee mechanism amounted to 5 € for the first gram of CO_2 exceeding the target, 15 € for the second, 25 € for the third and 95 € for each subsequent g/km. This fee has to be intended for each vehicle sold by the company. A similar methodology has been considered for vans in regulation (UE) n. 510/2011 [10]. The target specific emissions were evaluated using the same formula with different values for the coefficient a and M_0 and considering a target of 170 g/km instead of 130 g/km.

The previous regulations have been updated in 2019 with regulation (UE) 2019/ 631 [11] which set new emissions standards for passenger car and vans for 2020 starting from 2025 and 2030. Emission targets have been set at 95 g/km and 147 g/km for passenger cars and vans respectively, with the same formulation used in the past. Starting from 2021, a new type-approval cycle will be introduced. The World Harmonized Light Vehicles test procedure will substitute the New European Driving Cycle. Compared to the previous one, WLTP is much longer and characterized by a greater average power. For this reason, for 2021, a correlation between the results of the two test procedures is needed in order to define the emissions target.

$$WLTP_{ref,target} = WLTP_{CO_2} \left(\frac{NEDC_{2020_{target}}}{NEDC_{CO_2}} \right) \tag{1.3}$$

$\mathrm{WLTP_{CO_2}}$ is the average CO_2 emissions in 2020 in the WLTP, $\mathrm{NEDC_{CO_2}}$ is the average CO_2 emissions in the NEDC and $\mathrm{NEDC_{2020}}$ is the specific emission target calculated as in 1.2 considering 95 g/km.$\mathrm{WLTP_{re,target}}$ represents the reference specific emission target. Once known this value, the specific emission target for each manufacturer can be evaluated as:

$$WLTP_{target} = WLTP_{ref,target} + a\left[(M_\Phi - M_0) - (M_{\Phi,2020} - M_{0,2020})\right] \tag{1.4}$$

where a is a proportionality coefficient to take into account the fleet average mass of the manufacturer.

Based on the above methodology, beginning in 2021 new fleet wide reference targets will be evaluated based on WLTP measurements. Based on the results, a reduction of the limits in the periods 2025-2030 and 2030 onwards will be introduced. These reductions are 15% and 37.5% for passenger cars and 15% and 31% for vans.

On the other hand, heavy Duty vehicles are responsible for a quarter

		Sep 2020		YTD 2020		Compliance credit			Status 2020	Target 2020	Target gap
	Target gap	*WLTP*	*NEDC*	*WLTP*	*NEDC*	*PI*	*EC*	*SC*	*NEDC*	*NEDC*	*NEDC*
PSA-Opel	-1%	121	97	124	99	3	0.1	4.7	91	92	-1
Renault	2%	118	100	123	105	3	0.2	7.5	94	92	2
Nissan	2%	135	108	135	108	3	0.1	7.5	97	95	2
BMW	2%	138	114	141	116	3	0.9	7.5	105	103	2
Kia	2%	116	101	123	107	3	0	7.5	97	94	3
Hyundai	3%	115	101	123	108	3	0	7.5	97	94	3
Toyota-Mazda	4%	120	98	125	102	3	0.1	0.6	98	95	3
Ford-Volvo	5%	133	112	136	114	3	0.1	5.9	105	101	4
AVERAGE	5%	126	105	134	111	3	0.2	6.3	101	96	5
FCA-Tesla-Honda	8%	116	97	134	113	3	0.1	7.5	102	94	8
VW Group	9%	133	109	142	116	3	0	7.1	106	97	9
Daimler	13%	134	114	149	126	3	0.7	7.5	115	102	13

Table 1.1: New passenger car fleet average CO_2 emission level, by manufacturer [12]

of the on the road transport emissions. With respect to passenger cars and vans, the test procedure involves the definition of a mission profile an is based on the final destination of the vehicle. For the first time in 2019, regulations have been set to limit CO_2 emissions starting from 2025 and 2030. Emission standards are expressed as a reduction with respect to EU average in the reference period between July 2019 and June 2020. Reductions have been set at 15% in 2025 and 30% in 2030.

Table 1.1 reports the results of the most important manufacturers in the automotive sector in relation to their targets. The target gaps are evaluated considering also bonuses, introduced in the aforementioned regulations and consisting in CO_2 credits for eco-innovations and super credit for vehicles with emission under a certain threshold. Until recently, Volvo was expected to comply with the emission limits (109 g/km) due to its relatively heavy fleet and large share of hybrid and electric vehicles. On the other hand, Ford have been struggling for the opposite reasons. The two manufacturers joined together in a compliance pool with a new target equal to 101 g/km. 4 g/km separates them from the achievement. Almost all manufacturers are within 5 g/km from their respective targets except for VW group, Daimler and FCA-Tesla which are 9 g/km, 13 g/km and 8 g/km away.

Poor results of FCA and other companies are somewhat related to lower sales of electric vehicles in specific regions of Europe. As reported in figure 1.8, even if the share of electric vehicles in Europe is constantly increasing, it is still lower than 4% considering Battery and plug-in. However, their introduction in the market make the average fleet emission drop since there are no CO_2 tailpipe emissions. Given the always more stringent limits, this

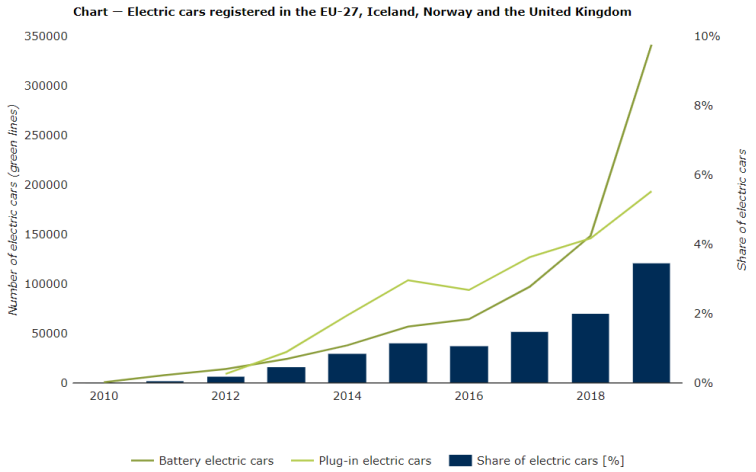

Figure 1.8: Newly registered electric car share in EU27, Island, Norway and United Kingdom [13].

measure has been necessary to reduce manufacturers fleet emissions even if their effectiveness to face climate change is still in doubt [14]. The transport sector in fact, contributes for slightly over than 10 % to the worldwide GHG emissions. In this sense, this is the maximum reduction achievable in this sector if all fossil fuel propelled vehicles would be substituted with electric vehicles supplied with CO_2-free electric energy. Obviously, this consideration does not take into account the related life cycle. Several analyses have reported that CO_2 emitted during manufacturing can be much higher than the one produced for a Diesel Engine [15], [16]. Batteries have a limited life, lower compared to the vehicles, determining management and disposal issues. In addition to that, they require rare material as cobalt and lithium which are located in restricted area of the world. Most of cobalt comes from the Republic of the Congo where lots of artisanal mines make use of child employment for the extraction [17], [18]. The existence of such issues question the sustainability of these measures. Electric vehicles adoption represents certainly a potential innovation in the transport sector but, with the current energy mix still largely dominated by fossil fuel energy sources and the current infrastructures, mainly thought for a vehicle fleet largely composed of internal combustion engines, these engines seems to have a longer future than expected.

Eco-innovations

Eco-innovations are a well known mechanisms introduced even before the last regulation of the European Commission. Its aim is to incentivize the development and uptake of efficiency technologies. In particular, eco-innovations rewards innovative technologies and systems which contributes to lower CO_2 emissions in conditions which go beyond the standardized testing procedure. In this sense, these technologies are also referred as "off-cycle". Eco-innovations certification can be obtained both by manufacturers and component suppliers.

Approval Process In order to be recognize as eco-innovation in the framework of the EU regulations, technologies must satisfy certain requirements. These requirements are the following:

- Technologies must not be part of EU commission strategies to reduce CO_2 emission. This aspect prevents the air conditioning systems, tire pressure monitoring systems, tire rolling resistance measures, gear shift indicators, and bio fuels from being eligible as eco-innovations
- Technologies must be novel. The parameter considered to establish the novelty of a specific technology or system is the market uptake. This latter should not be greater than 3% in 2009.
- Technologies must improve the safety or performances of the vehicles. Comfort related systems are not eligible (e.g. air conditioning systems and entertainment).
- CO_2 savings must be greater than 1 g/km and must be measurable in repeated tests.
- Multiple technologies can be grouped in order to meet minimum requirements of 1 g/km if they are functionally similar.
- The CO_2 emission reductions must be measurable only in test procedure outside the type-approval cycles.
- Technologies which depend on drivers' behaviour are not considered.

Total contribution of multiple eco-innovations cannot exceed 7 g/km of CO_2 reduction. Once fulfilled these requirements, the applicants propose a

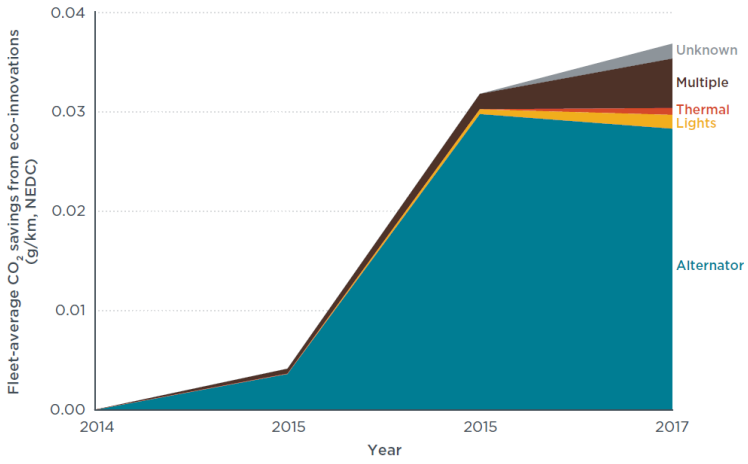

Figure 1.9: Average CO_2 savings from eco-innovations till 2017 [13].

Type	Approved EI	Installed EI	Vehicles registrations	Avg CO_2 saving [g/km]	Fleet-avg CO_2 savings [g/km]
Alternator	10	5	304,986	1,4	0,028
Kinetic	3	1	1	4,1	<0,001
Lights	7	1	20,109	1,0	0,001
Solar	3	0	0	—	0
Thermal	2	2	8,540	1,2	0,001
Multiple	—	—	28,140	2,7	0,005
Unknown	—	—	17,711	1,3	0,002
Total	25	9	379,487	1,5	0,040

Table 1.2: 2017 data on eco-innovations by type.

different test procedure. The vehicle is first tested with and without the eco-innovation. After this first step, a further test on the type approval cycle is done not to double count the potential savings. Once determined the CO_2 emission reduction achievable though this eco-innovation, the result is multiplied by an usage factor to take into account how often the technology is used in real conditions.

Figure 1.9 and table 1.2 report data on eco-innovation from 2014 to 2017. In this timespan, the benefits of eco-innovations in fleet average emissions reduction is increased up to 0.04 g/km. The motivations behind marginal benefits of these novel technologies are to be found in the little market penetration. In 2017, only 9 out of 25 eco-innovations were installed. Moreover, only 3% of newly registered cars were equipped with them. As a results, despite high CO_2 emissions reduction capabilities (up to 4.1 g/km), fleet average CO_2 savings amounted to just 0.04 g/km.

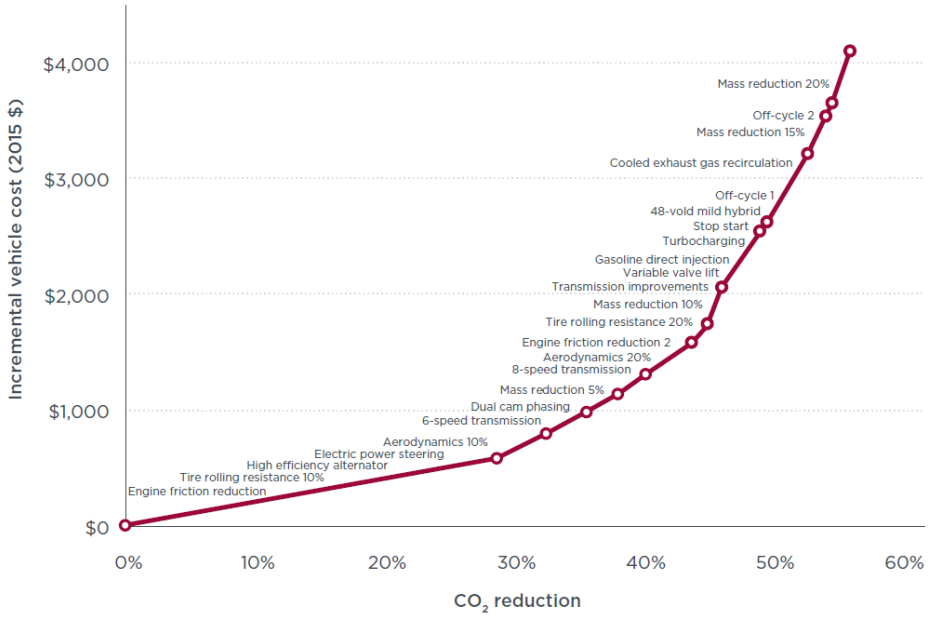

Figure 1.10: Incremental cost of emission reduction technology [19].

Although having a negligible impact, selected vehicles equipped with eco-innovations produce high emission reduction potential which could determine in the future lower fleet average reduction if the market penetration will be higher. This latter aspect is eventually going to get better with the newer emission standards going towards more stringent values in 2025 and 2030.

Energy efficiency technologies

Despite Internal combustion engines have been labelled in recent years as something to get rid of in favour of newly conceived electric vehicles, mainly by political and market driven declarations, several considerations can be done against this thesis. First of all, the demand of primary energy in the on the road transportation is large. It is estimated that there are 1.2 billion Light-Duty Vehicles (LDV) and 380 million Heavy Duty Vehicles (HDV) circulating in the world with growing numbers [20]. In particular, opposite to passenger cars, electrification of these kind of vehicles pose much greater issues related to battery size, weight and cost [21].

Advancement in ICE technologies for the reduction of CO_2 emissions are still achievable. Figure 1.10 reports an analysis conducted by the ICCT

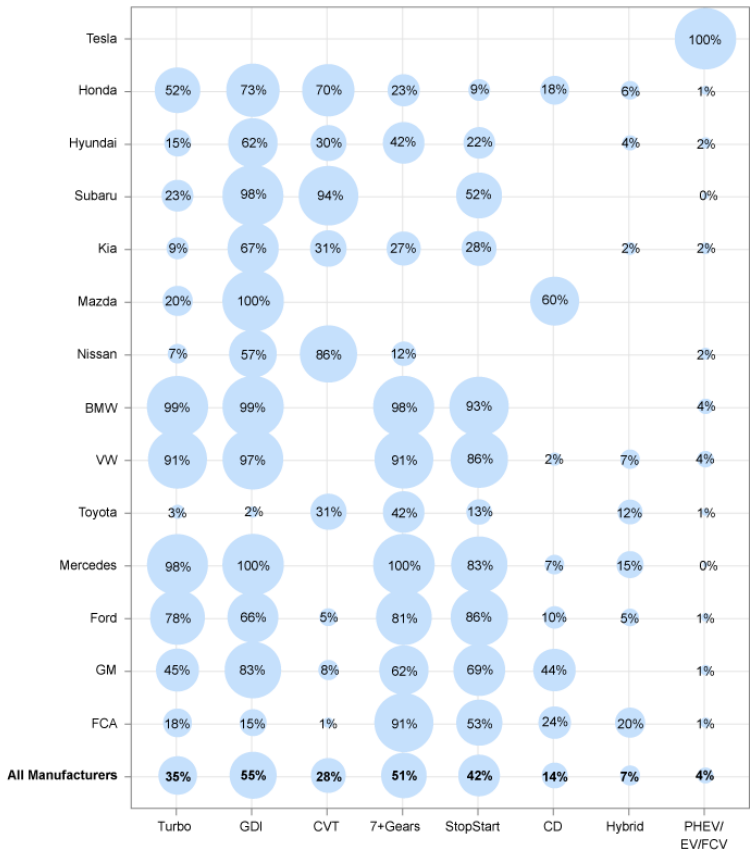

Figure 1.11: Technology share of large manufacturers in 2020 [22]

based on the Environmental Protection Agency data. The x-axis represents the incremental CO_2 reduction achievable with the adoption of several technologies on a LDV representative of the US fleet with respect to model year 2008. The y-axis is the incremental cost associated with that. In 2015, the light truck fleet was approximately in the 21 % reduction range.

The graph shows three different phases characterized by variation of the average specific cost. The first step determines a 28% emission reduction for a moderate cost of approximately 600 $. The group of measures include engine friction reduction, 10% tire rolling resistance reduction, high efficiency alternator, electric power steering, 10% aerodynamic drag reduction, dual cam phasing, more efficient transmission (e.g. 6-speed) and 5% weight reduction. The following step groups similar measures consisting in further reduction of weight, drag resistance and transmission improvements. Ulti-

mate measures on LDVs mainly rely on mild hybridization, turbocharging, exhaust gas recirculation and further mass reduction which are predicted to enhance emission reduction by more than 50% with an incremental cost around 4000 $. It is worth to say that part of the greater capital cost can be recovered during the operation of the vehicle, since lower emissions means lower fuel consumption.

In the passenger car field, innovations are largely dependent on specific manufacturers. Figure 1.11 reports 2020 data related to technology share by large manufacturers. Larger circles correspond to higher adoption rate. Almost all German based automotive companies make use of GDI, turbocharging and start/stop system with 7+ gears. Higher gears transmissions allow the operation of the engine near peak efficiency. A more advanced transmission system is the Continuously Variable Trasmission (CVT), which is adopted mainly by Subaru, Honda and Nissan. It is worth noting how some of these technologies have entered rapidly and consistently in the market. The share of Gasoline Direct Injection vehicles increased from 8% to 50 % between 2008 and 2020.

Mid to long term advancement in ICE will benefit also from the co-design of fuel/engine systems with Homogenous Charge Compression Ignition Engine (HCCI), Reactivity Controlled Compression Ignition Engine and Premixed Controlled Compression Ignition engine making possible the increase of the efficiency and the reduction of emissions and pollutants. State of the art researches have also found the possibility to create synthetic fuels fro the hydrogenation of captured CO_2. Obviously, the process is highly demanding in terms of energy and will be sustainable only in a scenario where the greatest part of the primary energy demand is satisfied with CO_2-free energy sources.

In addition to the aforementioned technologies, a further step forward towards the reduction of GHG emission through the increase of the engine efficiency is constituted by Waste Heat Recovery systems. Indeed, even in the best case scenario, the efficiency of an ICE in nominal operating conditions does not exceed 50%. The remaining part of chemical energy which is not converted in mechanical output is available as thermal energy in the engine cooling circuit, engine exhaust and in smaller part, in the lubrication circuit. Depending on the temperature level of these streams, several technologies have been studied to recover part of the waste heat.

Turbocharging is a well known methodology to recover energy exclusively from the exhaust gases. Engine exhaust thermal energy is converted in mechanical power through a turbine positioned right after the exhaust manifold. The mechanical power produced is used by a compressor on the same shaft which elaborates the intake air, increasing its pressure and allowing the engine to reach a greater power output. In turbocompounding systems, a further power turbine is added besides the turbocharger. The aim of this latter is to use the excess thermal power for a further conversion into mechanical or electric energy. Configurations can vary but mainly they are distinguished in serial [23] and parallel [24]. The most used configuration is the serial one, where the power turbine is placed downstream the turbocharger. This solution is simpler to use but has a greater influence on the engine performances determining high backpressure. On the other hand, in the parallel configuration, the exhaust is divided into two stream acting on a valve. In this way, the excess energy from the turbocharger is used in the power turbine. The advantage is a lower impact on engine performances because of the reduced backpressure. However in this case, the power turbine suffers in low load region due to insufficient inlet thermal energy. Widespread availability of this solution in automotive industry is mainly limited by low energy at low load and variability of the inlet conditions [25].

A totally different technology is represented by Thermo-electric generators. A thermoelectric generator is composed of several thermo-electric modules constituted by elements made of p and n semiconductor materials. These elements are connected in parallel from a thermal point of view and in series electrically. The energy conversion is based on the Seebeck effect, a phenomenon which determines a voltage difference between two semiconductors, proportional to the temperature difference they are subjected. Hot source is represented by exhaust gases or engine cooling circuit. Main advantages of this technological solution are represented by no moving parts and ease of installation. Different geometries can be used in order to fulfil space and volume requirements [26]. The downside is the back-pressure increase when the thermal energy coming from the exhaust gases is used as hot source. The conversion efficiency is between 2% and 5% with electrical power output under 1 kW [27], [28].

The thermal content of waste streams in internal combustion engine can be used by bottoming cycles to produce mechanical power which can be fur-

ther converted into electric power. Several different cycles have been studied over the years for Waste heat recovery applications: Kalina cycles, Stirling engine, Inverted Brayton cycles and Organic Rankine Cycles (ORC). Among all the possibilities, ORC-based power unit have gained a widespread attention in scientific literature because of their high thermodynamic potential, flexibility and low complexity of components [29]. Moreover, ORC systems can rely on a wide know-how since there are different commercial examples for stationary applications in the range of hundreds kW to MW. With respect to other alternatives, they can potentially guarantee higher conversion efficiencies in a wider range of upper temperatures [30]. The definition of a suitable working fluid allows to recover heat from varied waste streams, especially in ICE applications. Different layout are available to maximize the recovery of water jacket system, exhaust gases, intercooler and EGR [31]. Thermodynamic conversion efficiency potentials are strictly related to the quality of the available thermal power in terms of temperature and flowrate. However, lots of efforts must be made in order to make ORC-based unit a viable solution in the kW scale range. In particular, strong improvements are needed in the efficiency of components (expanders in particular) and the overall efficiency of the plant when working in off-design conditions as it happens frequently in ICE applications.

For these reasons, the following chapter will be entirely dedicated to the analysis of research studies on Organic Rankine cycles. First, the most important selection criteria will be discussed. After that, a thorough analysis on the different characteristics and influence on plant layouts will be exposed. Finally, a specific component-level study, highlighting different performances of expanders and heat exchanger is presented.

Chapter 2

ORC systems: State of the art

2.1 Introduction

In this chapter a thorough literature review on the state of the art of ORC systems will be shown. Most important aspects will be treated starting from the working fluid selection criteria in section 2.2. Different plant layout configurations will be exposed in 2.3 showing differences, advantages and downsides. Finally, studies related to ORC components will be discussed in 2.4. Given the amount of publications, the analysis will be restricted to the expander and the heat exchangers given their particular influence on system performances.

2.2 Working fluids

The most peculiar feature of ORC systems is represented by the possibility of selecting the most appropriate working fluid for any given application. As known, traditional power generation plants use steam as working fluid. They are quite conventional in the power generation sector, the upper temperature source is represented by the hot gas produced by a combustion, the lower source by a very large heat exchanger fed at ambient temperature. Reference cycles are either the Rankine or Hirn cycles and all the components, operational choices, management rules are very traditional from a technological point of view. The size of the power justifies complexity, costs, space required as well as the steady state working conditions which guarantee a continuous electrical energy production. ORC-based waste heat recovery

units even though they make reference to almost the same thermodynamic cycle, are a quite different matter. The power size is several orders of magnitude lower and their role is to recover thermal energy which otherwise would be wasted, at a temperature level which depends from different origins but usually much lower than that of a combustion process. Often the thermal source is not steady regarding thermodynamic and fluid dynamic conditions and the temperature difference between upper and lower sources is much reduced. A number of constraints must be respected, first of all the nature of the working fluid which has an organic nature . Selecting a proper working fluid with suitable thermodynamic and thermophysical properties make the thermal recovery from low and mid-temperature energy sources more viable. However several issues need to be considered and addressed during the design phase in order to optimize the overall system performances.

2.2.1 Selection criteria

Scientific literature has studied over the years several procedures and methodologies in order to take into account different parameters to define in a proper way the best working fluid for the specific application. Among the different factors, the criteria of selection involve the evaluation of the saturation curve, its critical temperature, the composition in case of mixtures and other technical factors related to safety and environmental impact issues. In the following sections most relevant studies related to these requirements will be exposed.

Saturation curve

The saturation curve represents the identity card of a working fluid. Once known it is possible to understand several important thermodynamic quantities as the critical pressure and temperature as well as qualitatively evaluate specific and latent heat for specified temperatures and pressures. Moreover, a first classification of working fluids is made based on the shape of the vapour saturation curve. The shape of this curve is evaluated through the parameter ξ defined as $\xi = dS/dT$ which represents the inverse of the vapor saturation curve slope. Making reference to this factor, isentropic fluids are characterized by a value of ξ equal to 0 while wet and dry fluids by a negative and a positive value respectively. Examples of different kind of fluids are

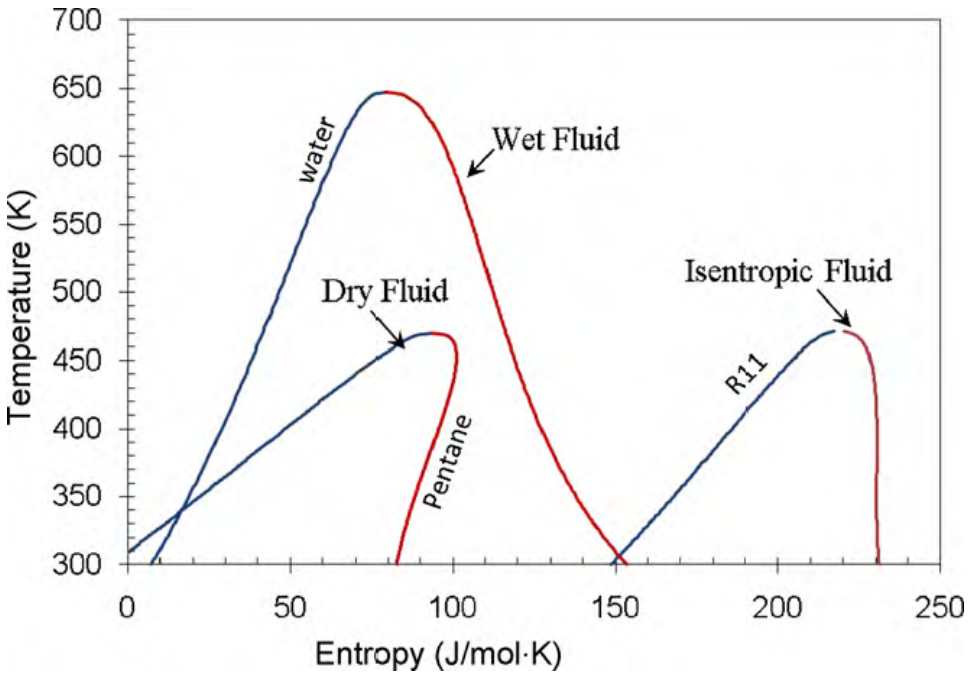

Figure 2.1: Examples of wet, dry and isentropic fluids [32]

represented in figure 2.1. Simplified equations for the evaluation of ξ have been studied in [33], even though actual values calculated using equations of state can show large deviations mainly at temperatures different from the normal boiling point of the fluid, [32].

The shape of the vapour saturation curve directly influences the choice and design of ORC components. Wet fluid are generally avoided, especially in not steady applications because of the issues related to the formation of droplets at the expander outlet which can damage the turbine blades when a dynamic machine is considered [34]. A reduced expansion work is produced when a wet fluid is considered. In order to avoid this phenomenon highly superheated vapour is needed and consequently higher heat transfer surfaces in the evaporator are needed to make possible the thermal exchange between the superheated working fluid and the available hot source. On the other hand, dry and isentropic fluids do not present these issues. The former has the advantage of exchanging heat at the condenser mostly in two phase conditions thus allowing the utilization of more compact heat exchangers [35]. The latter instead determines a low pressure superheated vapour at the expander outlet which increases the thermal load at the condenser. On

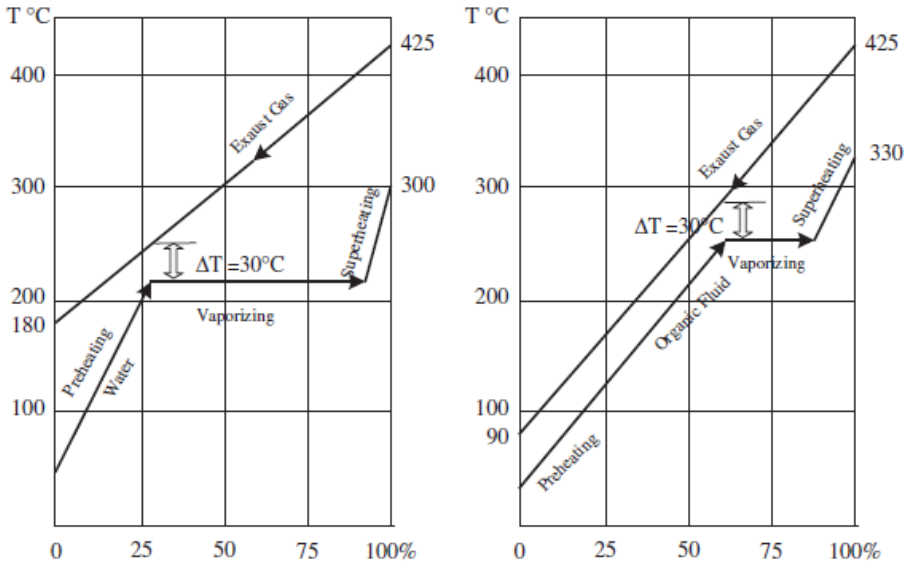

Figure 2.2: Latent heat effects on the evaporator irreversibilities [38].

the other side, this heat can be recovered by means of an internal heat exchanger, increasing the efficiency of the system [36]. However this choice could not be always feasible since the internal heat exchanger suffers from poor heat exchange coefficients given the low pressure of the fluid consequently determining larger capital costs [37].

A further aspect which can be evaluated looking at the saturation curve of a working fluid is the latent heat of vaporization. This parameter represents the enthalpy change from liquid to vapour saturation state and varies for each fluid with pressure (or temperature). However, for a given temperature value, the horizontal segment which characterizes the saturation lines give a qualitative representation of the latent heat extent. In [32] the authors conducted a qualitative analysis on the effect of the latent heat on the potential work output for a given working fluid. Starting from the Clausius-Clapeyron equation and considering an adiabatic isentropic expansion process of an ideal gas, the results show that the greater the latent heat the greater the specific work output of the ideal expansion. This leads to the conclusion that a working fluid with a high latent heat is preferable to increase the power output of the unit. This is supported also by other studies as reported in [39]. On the other hand, a greater enthalpy of vaporization could not be beneficial in low temperature waste heat recovery

applications [40]. In fact, a high latent heat can limit the heat acquisition mean temperature thus reducing the thermodynamic efficiency of the cycle especially when the hot source is low [41]. As a result the mean temperature difference at the evaporator can be high causing irreversibilities and reducing the exergetic efficiency of the system. In these cases, a lower latent heat can help reaching a higher vaporization temperature with a working fluid heating curve that better follows the hot source one (Figure 2.2).

Critical temperature

Critical temperature represents the most important aspect to be taken into account during the selection of the working fluid of an ORC system in the design phase. If its value does not match with the characteristics of the upper thermal source, poor results can be expected both in terms of power output and thermodynamic efficiency. Referring to the aforementioned studies ([41], [32]), when the critical temperature is much lower than the hot source inlet temperature, best efficiency evaporation temperature would be near the critical one where low latent heat is available and consequently lower enthalpy increase in the evaporator. On the other side, when the critical temperature is much higher, the evaporation temperature must be low in order to make the cycle viable and a lower thermodynamic efficiency has to be expected.

Different working fluids belonging to various types have different critical temperatures. In figure 2.3, critical pressure and temperature are shown for some fluids of different kind. CFCs, HCFC, and HFC cover approximately the same area. This is due in particular to the natural substitution of older refrigerants with newer generation ones characterized by lower environmental impacts in order to fulfil the requirements established by the Montreal Protocol first [42] and the Kigali Amendment afterwards ruling the phase down of HFC gases. HFO are represented as well in the same area, having these newer generation organic fluids zero Ozone Depletion Potential (ODP) and low Global Warming Potential (GWP). As reported in [43], given the good environmental performances and the thermodynamic similarities with fluids already in use, they could represent the future for Organic Rankine cycle systems. For these fluid typologies, critical temperature are mostly below 200 °C with varying critical pressures ranging from 30 bar to 60 bar making them suitable for low to mid temperature waste heat recovery. Hydrocarbons instead show larger variations of these parameters. In particular

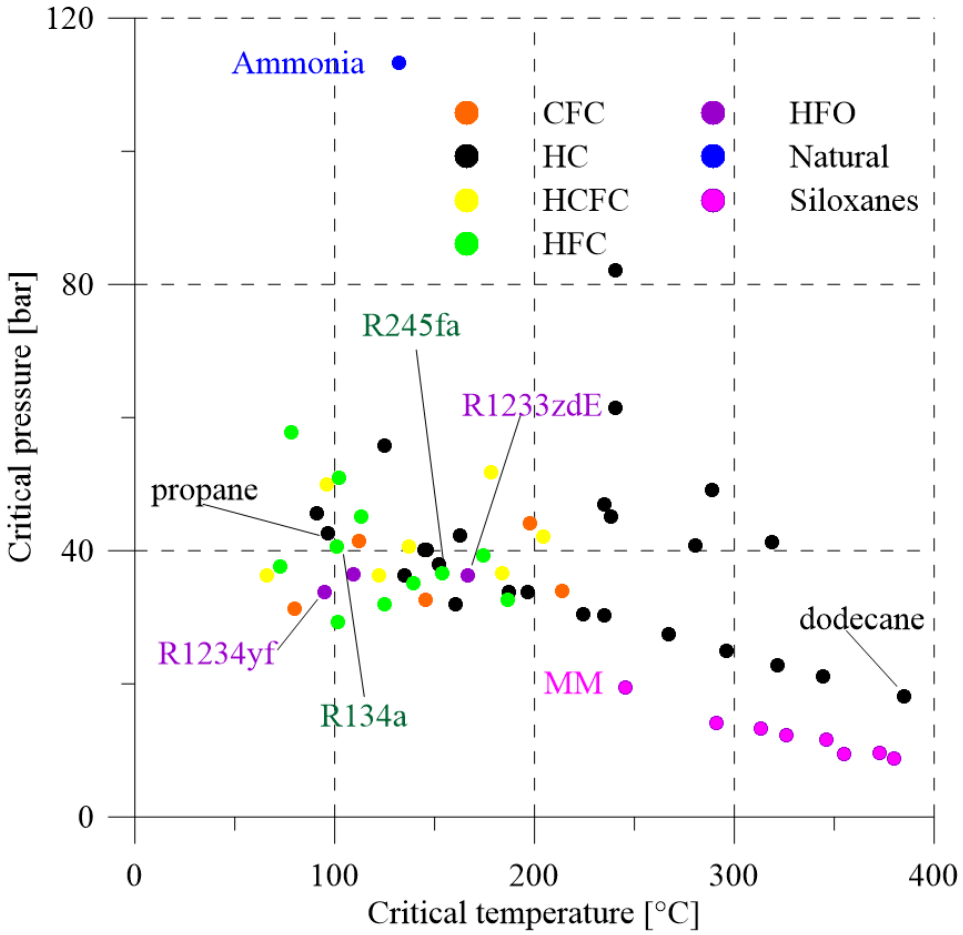

Figure 2.3: Critical pressure vs critical temperature diagram for different kind of working fluids

it is worth noting how they can reach critical temperatures as high as 400 °C which would make them especially suitable in mid to high temperature applications. However, problems related to flammability and autoignition determine the need for special handling that prevent them from being used in every application. Siloxanes are silicon compounds characterized by high critical temperatures (200-400 °C) with lower pressure values with respect to hydrocarbons. This latter aspect can be beneficial in the evaporator where there is the need to have lower operating pressures to reduce heat exchanger cost. However, it also leads to sub-atmospheric pressure at ambient temperature which could involve air infiltration at the condenser, lowering the performances of the system. For these reasons, in the evaluation procedure

presented in [36] the condenser lowest admissible pressure in set at 1 bar. Given their characteristics, siloxanes appear as a promising solution for high temperature applications as reported in [44], having the potential to reach 70% of the corresponding Carnot efficiency for the same hot source inlet temperature [45].

Because of the importance of a proper matching between the critical temperature of the working fluid and the inlet temperature of the hot source, several authors have focused deeply on this issue in scientific literature. Xu et al. [46] found that critical temperature is the only parameter to look at if the objective function is represented by the thermodynamic efficiency of the system. Its optimal value has to be comprised between the hot source outlet temperature and the working fluid one at the evaporator inlet. Moreover, further results show that it is possible to select organic fluids with critical temperature 30 °C below or 100 °C above the upper thermal source inlet temperature. In [47] an optimization genetic algorithm has been used to find the best design parameters of a basic ORC unit bottoming an upper hot source in the range of 50 °C-280 °C. 26 different pure fluids and mixtures have been investigated. Results of the analysis show that pure fluid must have a critical temperature from 30 °C to 50 °C higher that the hot source inlet temperature. Moreover if several working fluids with similar suitable temperatures exist, generally the wet one is favoured. Different criteria exist for mixtures. Optimal critical temperature is 30 °C to 50 °C below the hot source inlet one. Chen et al. [48] elaborated a procedure to define the proper matching with the aim to achieve the best exergetic efficiency. The method is based on the definition of an adimensional temperature as the ratio between the evaporation and critical temperature. Inlet temperature of the hot source is varied between 130 °C and 190 °C. Results show that for an adimensional temperature value of 0.85, best efficiency points are obtained when the hot source inlet temperature approaches the working fluid critical datum. Moreover a correlation is given between the two parameters.

Working fluids mixture

Fluid mixtures represent a valid alternative to pure fluids. A mixture is the combination of 2 or more fluids in specified mixing ratio. According to their behaviour they can be distinguished in:

- Azeotropic: if the mixture doesn't vary its composition and temperature significantly during isobaric phase change. In this case the mixing process determines only a variation of the thermodynamic properties of the components without altering its behaviour during condensation and evaporation processes.

- Zeotropic: if the mixture significantly varies its composition and temperature during phase change. If there is only a slight variation, mixtures are also referred as quasi-zeotropic.

The temperature glide shown by zeotropic mixtures represents the major advantage with respect to pure fluids. In fact, this temperature increase during the phase change process can be beneficial in the evaporator and condenser of the ORC system in order to increase the exergetic efficiency of the system, reducing the irreversibilities in the heat exchangers. Figure 2.4 represents a diagram of a water/ammonia zeotropic mixture. If it is considered a mixing ratio of 50/50 and assuming an heating process, when the temperature reaches the bubble point, vapour is formed. Initially this vapour is composed for the greater part by the most volatile component (ammonia in this case). During the phase change process, temperature increases, and water start vaporizing thus reducing the ammonia concentration in the vapour phase. At the end of the process, in correspondence of the dew point, mixture is completely vaporized and the final concentration of the vapour is the same of the initial one. The temperature difference between bubble and dew point is called glide and depends on several parameters: components, mixing ratio and pressure. The selection of the appropriate mixture has to take into account also the temperature glide in order to properly optimize the cycle

. In [49] a selection criteria based on exergy efficiency has been studied. A correlation between critical temperature and hot source inlet one is presented. Moreover the optimal temperature glide is a function of the temperature increase of the cooling fluid at the condenser as well as the working mixture desired subcooling degree. The same authors further investigated the same procedure adding a thermo-economic analysis in closed heat source conditions namely hot sources with given outlet temperatures. Correlations are given for the optimal mixture based on the extent of the temperature drop of the upper thermal source [50]. The literature study suggest that

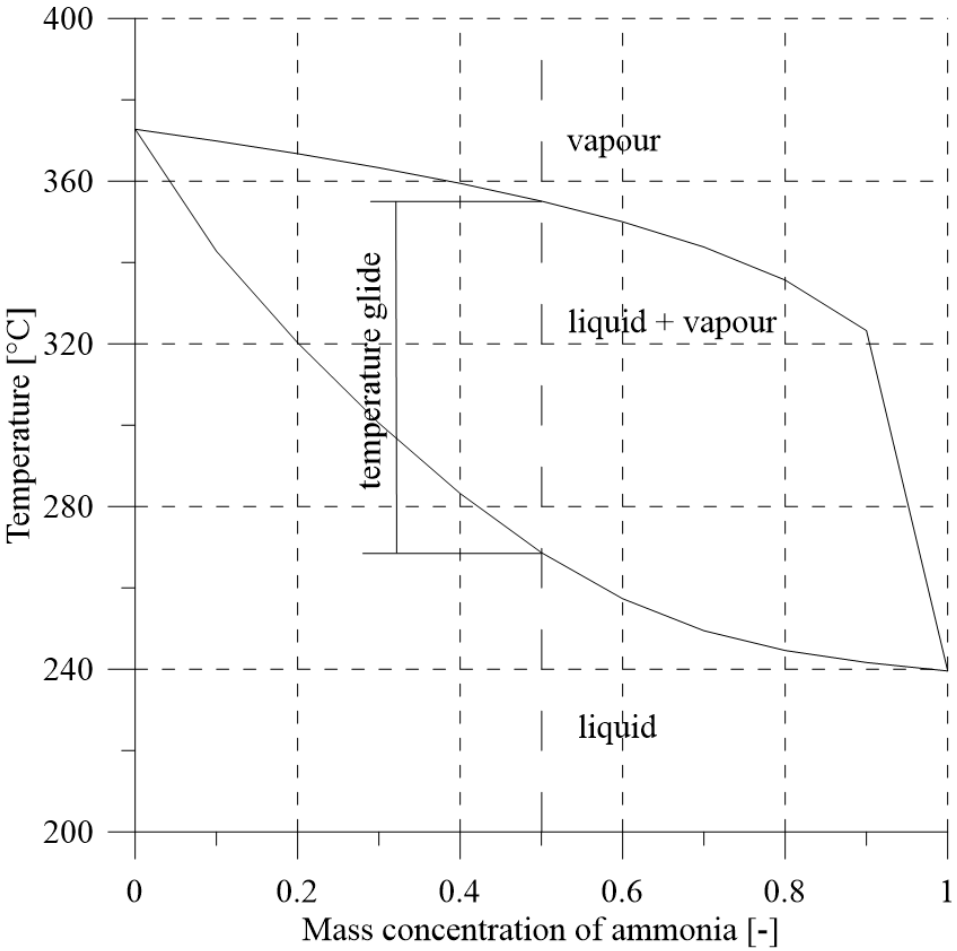

Figure 2.4: Example of water ammonia zeotropic mixture diagram.

the use of mixture can be particularly useful in case of low-mid temperature waste heat. Chys et al. [51] studied their potential in different ranges of hot sources inlet temperatures. Results show that for temperatures below 150°C an improvement of the efficiency and power output of 12 to 15 % is achievable. Same conclusions do not apply for higher temperature heat sources. In fact benefits are halved when considering temperatures up to 250 °C. Lecompte [52] conducted a second law efficiency analysis on the use of mixtures for low temperature heat sources. The improvements with respect to pure fluids are between 7 % and 15 % and they are caused by the reduction of the irreversibilities in the evaporator and a better matching of the heat transfer curve in the condenser. A thermoeconomic analysis is needed in order to select the best working fluid since several optimized mixtures

can produce similar results with efficiencies that show variations under 3 %. In [53] this issue has been investigated. Mixtures of HFC and hydrocarbons have been considered with hot source inlet temperatures between 80 °C and 200 °C. A genetic optimization algorithm has been used showing that a large group of optimized mixtures can achieve similar results. However, the higher the inlet temperature the fewer the mixtures that can achieve better results with respect to pure fluids. In addition to that, an important issue is outlined. The reduction of the irreversibilities in the heat exchangers is determined by a lower temperature difference between the fluids, which ultimately lead to greater heat transfer areas in order to exchange the same thermal power. Mixtures have been studied for high temperature applications too. In [54] the authors theoretically studied a dual loop ORC unit bottoming a six cylinders, turbocharged, Internal Combustion Engine (ICE). Mixtures of siloxanes and R123 have been considered for the high temperature loop to recover heat from the exhaust gases. With this system it is concluded that up to 20 kW can be generated with an overall efficiency greater than 20 %. The recovery of exhaust gases of ICEs has been studied also in [55]. In this case, small concentrations of hydrocarbon like benzene and toluene in mixtures of more conventional organic fluids have been considered. The proposed mixing ratio could help increasing the critical temperature of the working fluid, avoiding the flammability issues related to the use of pure hydrocarbons. The use of benzene in the mixture can increase the efficiency of the system up to 11 %.

These considerations seem to claim the superiority of mixtures with respect to pure fluids but some drawbacks need to be outlined. Most of them are related to practical and technical aspects which are usually not considered in thermodynamic studies. First of all the issues related to the lower heat transfer coefficients of mixtures is well known [56]. In fact, during the operation of the system, mixtures tend to produce vapour earlier with respect to pure fluids, reducing the heat transfer with the external sources both in the evaporator and in the condenser. Oyekale et al. gave further evidence of this in their study [57]. A thermo-economic optimization of a solar biomass ORC power plant has been conducted considering MM and MM mixtures as working fluids. Results show that siloxane mixtures have better thermodynamic performances with respect to pure fluids at the expense of greater investment costs due to a 20 % increase in the overall heat

transfer area of the heat exchangers. Other important factors to take into account when using mixtures are presented in [58]. Thermodynamic data evaluated in software tools through equations of state are not trustworthy in all conditions and could show discrepancies with experimental data. Moreover, evaporation and condensation processes produce mixture fractionation which determine a different composition of the working fluid which is actually elaborated with respect to the designed composition ratio. All these aspects are the cause of the difference between performances experimentally obtained and theoretical expectations.

Technical factors

The proper choice of the working fluid in an ORC unit has to fulfil also important requisites related to other technical factors such as environmental performances, compatibility with the different components of the plant (e.g. oils or plastic materials) and costs. Xia et al. [59] proposed an evaluation methodology for the working fluid selection and parameter design based on a Comprehensive Evaluation Index (CEI) that takes into account the payback period of the system and the annual emission reduction in addition to heat recovery efficiency and exergetic performances. Each of these factors are lumped into one single index which contributes to the variation of the CEI. Results show that the best overall performances are achieved with butane and R1234yf in low temperature applications and R1233zD for higher temperature hot sources.

Wang et al. carried out an analysis in order to define selection criteria for low temperature applications taking into account environmental performances, both for pure fluid and mixtures [61], [60]. In the first case, the evaluation algorithm is based on electricity production cost and green-house gases emission reduction as objective functions. Hot source has been varied up to 230 °C. CO_2 equivalent emissions are grouped in three main categories namely construction, operation and decommissioning. Total amount of them has been further distributed in each component of the unit (figure 2.5). Results show that the evaporator contributes the most to the overall GHG emissions. Moreover, most of them are produced during the operation phase of the system especially for high GWP working fluids. The best environmental performances are obtained instead with iso-butane (R600a). A similar procedure has been applied also for mixtures, confirming in this case

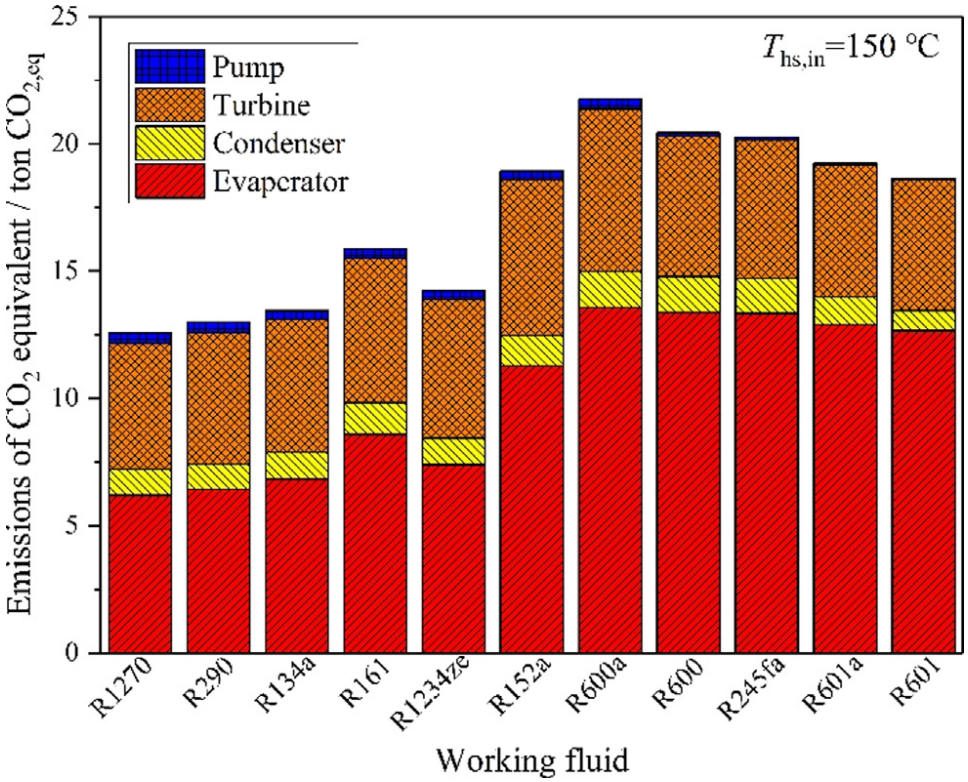

Figure 2.5: ORC component CO_2 equivalent emissions share during life cycle (from [60]).

the environmental impact of heat exchangers. A peculiar conclusion in the study is that environmental and thermodynamic optimum does not coincide for the same mixture. Working fluid definition influences also other technical factors. In [62] it is found that the working fluid can highly influence the inertia of the whole system, making it an even more important aspect to consider especially in unsteady applications. The present issue has been examined through a Simulink model finding that in most cases fluids with higher critical temperature are characterized by higher inertia. Finally, the working fluid choice can deeply influence the design of other components. In [63] it is concluded that the if properly defined, the same working fluid can be used in the same unit in order to satisfy power requests in extended ranges. The study is validated through an analysis of a radial turbine able to generate from 2 kW to 30 kW in the same unit with only slight efficiency variations for different values of thermal power exchanged in the evaporator.

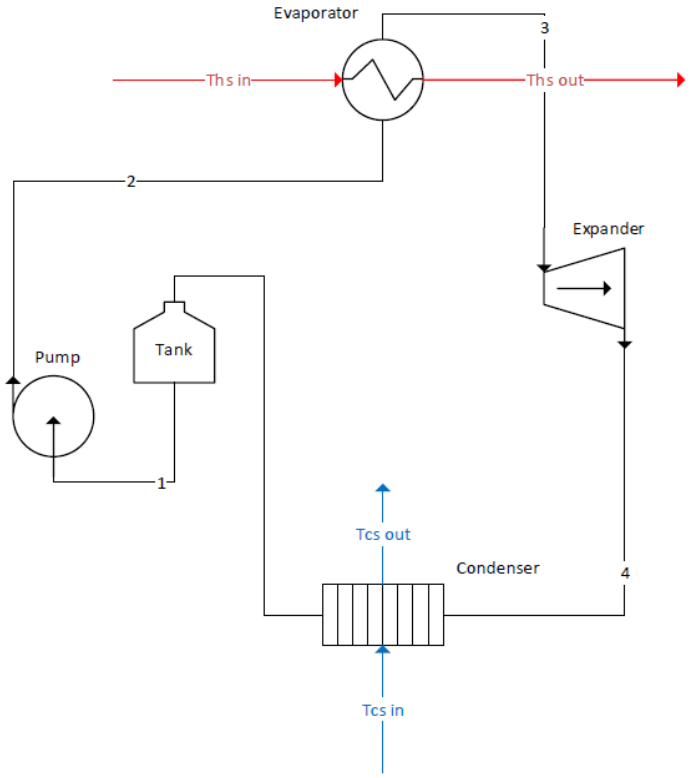

Figure 2.6: Plant layout of a reference ORC system unit.

2.3 Plant layout

In this section different plant layout of ORC systems will be referenced and discussed. Given the amount of theoretical and experimental studies on the subject, bibliographic analysis will be restricted to studies on units bottoming light duty and heavy duty internal combustion engines and on most relevant studies with comparable range of power output.

2.3.1 Reference

What is called in this section a reference layout is the simplest form of a ORC power unit. It is comprised of four components: a pump, an evaporator, an expander and a condenser. The pump pressurizes the working fluid (according to the hydraulic characteristic of the circuit) elaborating a certain quantity of flow-rate which enters the evaporator where it exchanges

heat with the thermal source vaporizing and eventually superheating before entering the expander. In this component the pressurized vapour at higher temperature interacts with its moving parts, producing work on a rotating shaft. The produced mechanical energy can eventually be further converted in electric energy under various forms. In addition to the cited previous components a tank is usually added upstream the pump. This component, even if does not exchange heat or work, is important in order to fulfil several functions. First of all it allows to avoid cavitation phenomena inside the pump, assuring a sufficient input hydraulic head. In addition to that, it increases the overall volume of the plant and lowers the pressure level at the condenser influencing the optimum working fluid charge of the unit and indirectly also the performances of the heat exchangers as reported in [64] and [65]. The advantage of this kind of layout is represented by its simplicity which produces an ease of operation with respect to more complicated layouts. Moreover, the use of a reference layout instead of a recuperative one could allow the maximization of power instead of thermal efficiency which is the purpose of a Waste Heat Recovery Application [66].

Making reference to the waste heat recovery in ICE, several feasibility studies are available. The transport sector in fact is interesting from this point of view given the different sources available for recovery: exhaust gases, EGR and engine cooling circuit. However, the application on board of an ORC unit gives birth to a series of issues that need to be addressed to understand the effective power output achievable in real conditions. Some of them are related to engine backpressure and weight increase [67] which could halve the potential benefits of the unit on the overall power output increase [68]. Moreover if a radiator is considered as the condenser of the system, enough space has to be available at the front of the vehicle [67]. In [69], the recovery of the thermal energy in the engine cooling circuit is investigated on a 62 kW gasoline engine. Up to 4 kW can be recovered using Ammonia in order to keep the flowrate as low as possible. The high values of thermal efficiency presented are the results of a low condensation temperature of the unit (around 30 °C) and unrealistic isentropic efficiencies assigned (80 % for both expander and pump). More realistic values of these parameters could result in much lower benefits. Same considerations are made in [70]. In this case, a genetic algorithm is used in order to optimize a ORC unit with a tube and fins evaporator recovering thermal energy from the exhaust gases of 240

kW Diesel engine. Maximum power output is claimed to be around 12 kW at a condensing temperature lower than 30 °C which is hardly achievable in real driving conditions. Several studies investigated many aspects of ORC units using this kind of reference layout: electric load influence [71], grid vs off-grid operation [72], R245fa/R134a mixture potential in low temperature range [73], and extension of operation range through two expanders operating in parallel [74]. In the ICEs applications, Galindo et al. [75] tested an ORC unit bottoming a gasoline engine in a range of 5 kW to 30 kW at the evaporator. Given the high temperatures involved, ethanol was chosen as working fluid allowing high condensation and evaporation temperatures (approximately 90 °C and 160 °C). Results show a recovery of 3.8 kW with a thermal efficiency of the unit equal to 6 %. It has to be outlined how all the aforementioned experimental studies show thermal efficiencies below 8 % which are far from the data assumed in theoretical studies.

2.3.2 Recuperative heat exchanger

A recuperative heat exchanger is a component able to recover heat available at the expander outlet in order to preheat the working fluid exiting the pump (2.7). It allows to increase the thermodynamic efficiency of the cycle and lower the thermal load both at the condenser and the evaporator. Despite its theoretical advantages, the use of recuperative heat exchanger poses several issues to be addressed. First of all, it increases the capital investment needed for the unit. This aspect is even more true considering that no phase change occurs inside the exchanger resulting in lower heat exchange coefficients and higher heat transfer area per unit of exchanged thermal power. Moreover, the feasibility in the utilization of such component is dependent on the characteristics of the selected working fluid. As previously observed, wet fluids have to be strongly superheated in order to have a temperature high enough at the expander outlet to make the heat exchange viable. Dickes et al. studied the effects of working fluid charge on system performances both theoretically [64] and experimentally [65] on a recuperative 2 kWe ORC power unit. The results of the studies show that thermodynamic conditions of evaporator and condenser in terms of pressure, superheating and subcooling degree are strictly connected and depends on the charge distribution of the unit. Regarding the recuperative heat exchanger, the unit is much less sensible to his presence since the mass inside

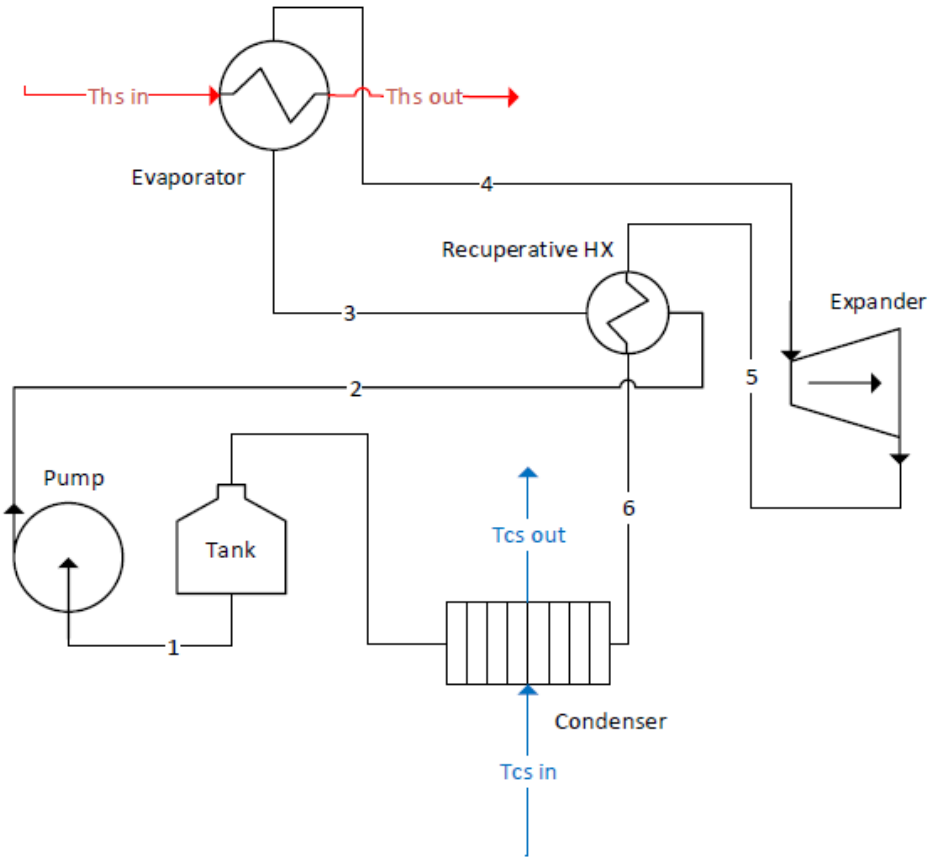

Figure 2.7: Plant layout of a ORC system unit with recuperative heat exchanger.

it does not change significantly during the operation. Moreover the charge of the system is identified as a parameter to be optimized. If its value is too high the liquid receiver is flooded with liquid resulting in an increase of the condensation pressure and subcooling degree. On the other hand, if it is too low, it can trigger cavitation and instability phenomena in the pump as reported also in [76].

The modelling aspect for the determination of the system operating points in off-design conditions are further studied in [77]. Three different modelling methods are compared. Best results can be achieved through semi-empirical models which have the edge over polynomial fitting based methods and constant efficiency methods. In these latter cases the ability to describe the system and the single components performances are poorer

since such methods do not consider the physics of the system. Semi-empirical models are also used in [78] where a 11 kWe ORC-based unit equipped with a double screw expander is investigated. Input parameters of the model are represented by hot and cold source inlet conditions, expander speed and pump speed. Output calibration parameters are the working fluid mass flow rate and the evaporation and condensation pressures. Subcooling degree has been fixed in this case. Deviations are lower than 1 % for the output parameters and 2 % for the prediction of the expander power. Other experimental studies investigated the effects of superheating degree and cold source inlet temperature [79] on turbine performances and the use of MDM siloxane for high temperature waste heat recovery [80].

2.3.3 Double evaporator

In what is called here a double evaporator layout, two heat exchangers are used in order to recover the waste heat from the hot source either in series or in a parallel configuration 2.9. The literature review has shown that few studies investigated the performances of such configurations especially in ICE applications which are inevitably not steady. This double heat exchanger allows a better utilization of the waste heat, especially if it is available at high temperature or in form of different sources. The drawbacks of this layout is related to the additional cost of the evaporator which is the most critical component of the ORC units, the backpressure effects on the exhaust line of the ICE (especially in the series configuration) which need to be carefully assessed in order not to decrease the efficiency of the engine [81] and the control issues related to the actuation of valves to split the working fluid flowrates according to the available thermal energy. Guillame et al. [82] conducted a wide thermo-economic analysis on different architectures and working fluids for heavy duty diesel engines. Results of the analysis show that among the different architectures, the EGR/EG recovery in series or parallel configuration can achieve best performances from a cost and thermodynamic perspective. Xu et al. [83] modelled a WHR unit with a parallel configuration recovery heat from EGR cooler and tailpipe gases. The unit makes use of two pumps in series and a turbine expander mechanically coupled to the engine shaft through an high speed transmission. No absolute values of power output are presented but the unit is assured to be capable of recovering more than 90 % of the recoverable cumulative energy on the eight mode AVL cycle.

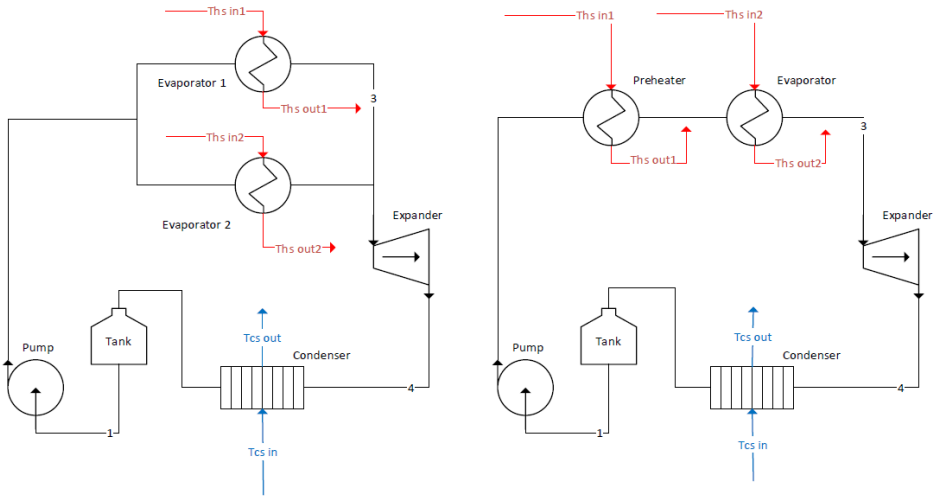

Figure 2.8: Plant layout of a ORC unit with double evaporator, series and parallel configuration

In [84] a series layout recovering heat from exhaust gases of an heavy duty diesel engine has been tested experimentally. Three different configurations have been analysed: EGR, EGR plus tailpipe gases and tailpipe exhaust gases only. Ethanol has been chosen as working fluid due to lower cost and lower evaporation pressures which decrease the cost associated to the manufacturing of the evaporators. Results show that best power outputs are achieved recovering heat from the exhaust gases only. However the EGR/EG configuration has been preferred because of better waste heat utilization and lower backpressure effects on the ICE. Maximum indicated power of the turbine expander peaked at 9 kW.

2.3.4 Dual loop

Dual loop ORC-based units are composed of two systems operating at different temperatures. A high temperature (HT) loop and a low temperature (LT) one are connected through an heat exchanger. Usually the waste heat of the HT-loop condenser is used to heat up the working fluid used in the LT-loop evaporator. The complexity of the whole system is undoubtedly higher as well as the potential heat recovery and exergetic efficiency. Given the number of components and the weight associated with them, focusing on the on the road transport sector, these applications are limited to large engine with multiple waste heat streams. In [85], the same working fluid

has been considered for both loops. The HT one recovered heat from the exhaust gases while in the LT loop multiple HXs in series recovered heat from charge air, HT-loop condenser and jacket water. Maximum thermal efficiency is 5.4 % with about 28 kW of output power. The efficiency and brake specific fuel consumption improvements in a six-cylinder Diesel Engine stands at 13 % and 4 % respectively. Similar results are obtained in [86] where the top system is represented by a 210 kW CNG engine. Newer HFO refrigerants R12133zD and R1234yf are used as working fluids in the bottom system which consists of a supercritical HT-loop and a subcritical LT one. Optimization results show that an improvement of more than 8% of the BSFC can be achieved in most part of the operating map of the engine with the supercritical system outperforming the subcritical one. Shu et al. [87] studied the same kind of system evaluating the possibilities to use Hydrocarbons in the HT-loop in a 243 kW HDDE. 34 kW and 10 % thermal efficiency are the performances achievable by the bottom system with a 16 % increase of the overall engine efficiency. Waste heat recovered was represented by exhaust gases, EGR, charge air and jacket water. The same authors further analysed the system from an economic point of view evidencing critical aspects related to the jacket water heat exchanger and the LT-loop expander cost. Summarized results evidence the unsuitability of such WHR units for commercial purposes [88].

An experimental study of a cascaded steam / organic Rankine cycle WHR unit is presented in [89]. Also in this case an HDDE is considered with the bottom unit recovering heat from the exhaust gases only. Both expanders are replaced by expansion valves with the consequence that the maximum power output is just an estimate based on assumed expander isentropic efficiency. The potential increase of the power output of the engine is of 5.6% with the cascaded system contributing with 12.7 kW. It has to be outlined however that such positive results are also derived from assumptions on low condensation temperature which are hardly achievable on board [67].

2.4 Plant components

2.4.1 Heat exchangers

Heat exchanger (HX) are responsible for the heat transfer between the external sources and the working fluid of the ORC-based unit. Among the

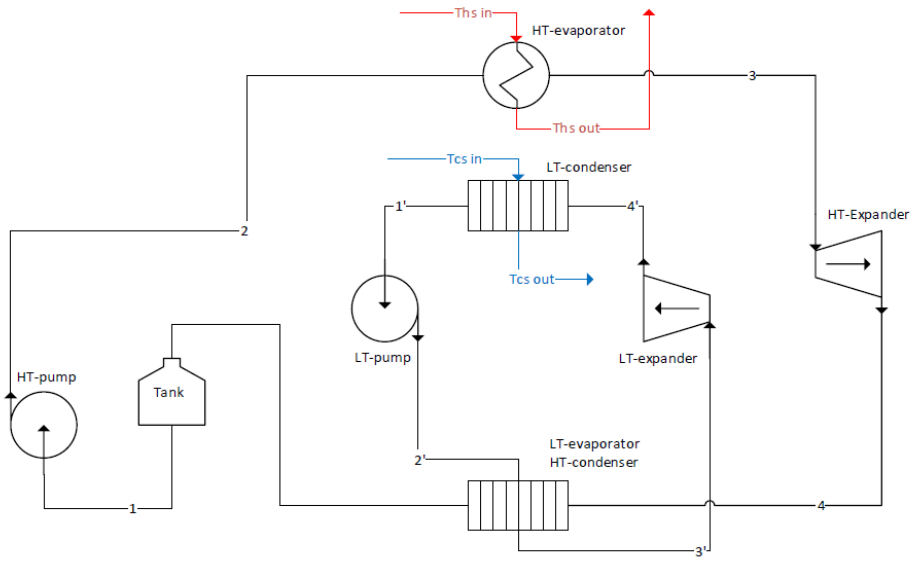

Figure 2.9: Plant layout of a dual loop ORC unit.

different HXs of an ORC system, the evaporator assumes a greater importance with respect to other components. The evaporator has the role of thermally energizing the working fluid before it enters the expander where it can produce mechanical energy. Thermodynamic conditions at the expander inlet are defined in this component which has to satisfy several conditions. First of all, it has to guarantee a superheated state in most applications. Liquid droplets in dynamic turbines wear out the turbine blades. Volumetric expanders instead can tolerate such conditions. However, except for different applications as Trilateral Flash Cycles (TFC) and Organic Flash Cycles (OFC), they are usually designed to work with vapour and the presence of a liquid phase decreases the inlet density causing a performances drop. Additionally, in small scale applications, there could be space limitations and the evaporator has to fulfil constraints related to size and volume while assuring also high heat transfer coefficients and low pressure drops for both fluids.

Plate Heat Exchangers (PHX) satisfy all these requisites in most applications. They are characterized by multiples plates in parallel. The working fluid enters the inlet port and is split according to the number of channels. Each channel is delimited by two plates with corrugations on theirs surface in order to increase turbulence and heat transfer coefficients. This kind of

configuration ensure a pure counter current heat exchange. Desideri et al. [90] experimentally studied the heat transfer and pressure drop characteristic of a brazed plate HX in flow boiling conditions for a low temperature WHR application. The analysis of the experimental tests showed a proportionality of the pressure drop with respect to the mean quality of the fluid, with heat transfer performances weakly dependent on the saturation temperature. A further result of the study is the similarity of R245fa and R1233zD regarding heat transfer characteristics, making them interchangeable. In [91] the effects of corrugations on PHX performances are studied. The application they are designed for is a LT-WHR on the water jacket system. The results show a strong correlation between chevron angles and heat transfer coefficients. A study on a novel technology applied to PHX is reported in [92]. A metal foam structure in presented. It allows to further reduce the size and weight of the component and increase the heat transfer coefficient. Main drawback is the greater pressure gradient which does not nullify the enhanced performances of the ORC unit.

Pressure drop has to be carefully evaluated being the HXs the most resistive components from a hydraulic point of view. This aspect is in contrast with the majority of thermodynamic optimization studies where pressure drop are usually neglected in the early stage. This issue is treated in [93] where the effect of pressure drop on ORC performances are evaluated considering a WHR application on thermal oil at low temperature. The results show that pressure drops can reduce the overall efficiency up to 20 % with respect to the ideal case. Similar conclusions have been derived from a different study considering shell & tube HX in place of PHX [94]. In this case it is outlined how also the economic performances can be greatly overestimated without any considerations on the hydraulic performances of the HXs.

Pressure gradients in fact are the main downside of PHX when at least one of the fluids crossing them is in vapour phase. The cross sectional area can be too small and the corrugations increase the resistivity of the component. The result is that main applications of this kind of HXs in ORC systems is limited to the thermal recovery of oil, water and generally liquid streams. In case of on hot source in vapour phase as it happens in the waste heat recovery from the exhaust gases of an internal combustion engine, other options are preferred. The use of conventional PHX in fact increases the backpressure of the engine, sensibly reducing its performances

compromising the power output increase due to the recovered heat. In [95], an optimization procedure has been conducted for an ORC based unit bottoming the exhaust gases of an ICE. In this case, plate and fins (P&F) and finned tube evaporators are considered. The study focuses on the trade-off between power output and total heat exchange area, showing that a little decrease in the first is able to reduce greatly the latter with consequent economic advantages. In another study [96], P&F HX are considered for a similar application. A direct evaporation layout is compared with an indirect one using an intermediate oil circuit. The first one is characterized by a lower footprint. The drawback is the lower thermal inertia which can cause the degradation of the working fluid due to hot spots in the heat exchanger. However, the latter issue can be avoided taking it into account during the design phase. Thermal inertia in fact can be varied in order to dampen thermal fluctuations.

Finned tube heat exchangers represent an improvement of conventional shell and tube HXs specifically designed for applications involving vapour streams to reduce pressure gradients. Exhaust gases in this case face a larger cross sectional area, which facilitates the passage while heat transfer characteristics are improved through finned surfaces fixed on the tubes outside diameters which increase the heat transfer area as well as turbulence. In [70] they are considered for an optimization study on a WHR application on an internal combustion engine with the aim to minimize the power per unit of heat exchange area and exergy destruction rate. Thermo-economic viability of these components is also confirmed in [37] where the combination of finned tube evaporator and PHX condenser shows the best performances from this point of view.

As aforementioned, dynamic response of HXs and evaporator in particular is important to develop model based control strategies in non steady or unsteady applications. Usually, modelling methodologies of the dynamic behaviour of these components are of two different types: moving boundary methods and finite volume methods [97]. In moving boundary methods, the working fluid is divided into 3 different zones corresponding to a different thermodynamic phase: liquid, 2-phase, superheated. Mass and energy conservation laws are applied in each zone which has a moving boundary in order to define a system of differential equations. The thermodynamic state of each zone is lumped into one single node. In this way the evolution of

the wall temperature, the thermodynamic state of the working fluid in the zone as well as the hot/cold source can be determined. In finite volumes method the heat exchanger is divided in a finite number of control volumes with mass and energy conservation equations applied on each of them. The formulation is similar but the computational efforts and the accuracy are different. In [98], Galuppo et al. developed a dynamic model of an ORC unit considering the dynamic response of a P&F evaporator using a finite volume method. An innovative control strategy of the condenser pressure is introduced acting on a compressed air storage linked to the tank upstream the pump. In [99] and [100] comparisons between finite volume and moving boundary modelling approaches have been made. In the first case the models have been applied to a helical coil HX for an ICE application. Results of the analysis show that moving boundary methods achieve slightly lower accuracy performances with respect to finite volume methods while ensuring a lower computational effort. A third approach, namely 0-d method, has been introduced with good results in term of accuracy and computational efficiency. In this case, the mass of the HX has to be corrected with a calibration coefficient. Comparable conclusions are achieved in the second case for a S&T evaporator. A different simulation approach has been considered in [101]. In this case a moving boundary method has been applied to a PHX for the thermal recovery of exhaust gases. The difference is in the evaluation of heat transfer coefficient which does not make use of physical correlation but instead consider the heat exchange coefficient proportional to the involved mass flowrates through some calibration coefficients experimentally evaluated.

2.4.2 Expanders

Dynamic

Dynamic expanders have a long tradition in power generation systems being them widely used in MW-scale power plants. However, their use is still limited in ORC unit under 50 kW nominal power. They offer high pressure ratio as well as volumetric and isentropic efficiencies. This leads to higher thermodynamic power outputs. However, a large part of this power is often dissipated in electromechanical losses because of the high rotational speed needed to operate such machines. This issue determines the need

for lubrication with a separate lubricating oil circuit in addition to possible vibrations, especially in non-stationary applications. In these devices, the expansion work is produced through the evolution of the working fluid inside turbine blades correctly shaped. These latter have a full 3-d development which make their geometry hard to obtain from a manufacturing point of view given also the stringent tolerances needed. This complexity increases costs.

Depending on the flow arrangement two main categories can be distinguished: radial and axial turbines. Guillame et al. [102] studied the performances of 3.5 kWel radial inflow turbine in a non-recuperative ORC-based unit thought for WHR on truck application. A comparison between R245fa and R1233zdE is presented. The peculiar feature of the device is the absence of a lubricating oil circuit. Lubrication and cooling needs are achieved with the same working fluid elaborated in the plant. Best performances are achieved with R245fa, reaching an overall efficiency of 32 %. An thorough characterization of the different energy losses show that the bearing system and the electro mechanical conversion greatly reduce the thermodynamic performances which tops 70 % adiabatic efficiency. In [103] a similar device is studied. Rotational speed effects are analysed in a WHR unit recovering heat from thermal oil. It is observed that mass flowrate and power output increase with speed which varies from 20 kRPM to 55 kRPM. Isentropic efficiency reaches its maximum (83.6%) at 35 kRPM. Cooling water also plays a significant role, lowering the condenser pressure and increasing pressure ratio and power output. Alshammari [104] tested a radial turbine in an ORC-based unit bottoming an HDDE with an intermediate oil circuit. Steady state tests have been conducted reaching a maximum isentropic and electromechanical efficiency of 88 % and 35% respectively. Maximum power output reached 6.3 kW with a cycle efficiency of 4.3 % at 40% engine load. The same authors designed a back-swept radial turbine for high pressure ratio. Modelling activities have been carried out with Novec649 as working fluid for an ICE-WHR application. Numerical results show that 13.6 kW can be produced at 73% efficiency. In [105] a radial turbine in a micro CHP application is tested. The ORC unit recover heat from thermal oil with HFE7100 as working fluid. The study focused on the effect of the supply system configuration. The addition of a second inlet produced a 36% internal efficiency increase of the turbine which improved from 52% to 71%.

Literature review has shown similar results in terms of power output and efficiency for axial turbines. Sun et al. numerically studied the performances of axial turbines focusing on the effects of working fluid mixtures [106] and nozzle types [107]. In the first case mixtures of R245fa and R123 are studied using Ansys CFX as virtual platform. Best performances are achieved using pure R245fa yet. In the second one instead, modelling activities are conducted on an axial impulse turbine varying the total number and type of nozzles (convergent vs de Laval). It is found the convergent nozzle are better for lower mass flowrates but supersonic ones are able to achieve better efficiencies. Axial impulse turbines are also studied in [108]. Experimental test have been carried out on a WHR unit for ICEs applications. The high isentropic efficiencies have been deteriorated by the electromechanical performances with overall efficiencies of 50-55 %. A comparison between an axial and a cantilever radial turbine is reported in [109]. The aim of the study was to evaluate the potential of such devices in application with nominal outputs below 15 kW also at off-design conditions. Results show that both turbine types are able to work at isentropic efficiencies higher than 70 % in a wide range of operating conditions. Radial turbines showed higher performances but are more susceptible to rotational speed.

A totally different concept of turbine is presented in [110]. In this case a Tesla turbine, a concept known since a long time, is reintroduced to understand its feasibility in small-scale ORC-based unit. This kind of devices are constituted by convergent nozzle which direct the working fluid from the external radius of several parallel plates which constitutes a bladeless rotor. The power transfer is given by the frictional phenomena between parallel plates. The device has the advantage to operate at lower rotational speed. However, despite the innovative concept, experimental results show that lot of work needs to be done in order to improve the efficiencies which reached a poor 30 % isentropic efficiency.

Volumetric

Volumetric expanders are by far the most used expansion devices in ORC-based unit with nominal power output below 50 kW. The expansion process is governed by the specific geometry of the machine which varies depending on the considered type. However, despite the different geometries, in every case the working fluid expansion is obtained through the evolution of a closed

volume (chamber) which traps a certain amount of fluid at the end of the suction process. During the expansion this volume expand producing useful work. This aspect allows the device to elaborate even fluid in the two phase region without interfering or compromising its functionality thus allowing a much easier operation of the ORC-based unit. With respect to dynamic type, much lower rotational speeds are needed which allow a direct coupling to electric generators without the use of gears. This aspect determines also higher conversion efficiencies from mechanical to electric power. The downside is represented by the lower volumetric performances which inevitably affect the expander as well as the ORC-based unit performances. Given the nature of volumetric expanders a differentiated literature review is presented in the following paragraphs.

Screw Screw expanders represent a valid alternative when considering volumetric type machine in ORC-based applications. They are obtained from compressors used in the air compression sector. Among the different types, two main categories can be distinguished, at least considering the studies related to their application in ORC unit: single screw expander (SSE) and twin screw expander. In the first case, the evolving chamber volume is constituted by the coupling of a screw rotor with several grooves and 2 gaterotors which follow the rotation of the main one. In twin screw expanders instead, two screw rotors, a male and a female one, are coupled in order to constrain the working fluid inside the chamber. An example of the two devices is reported in figure 2.10. With respect to other type of volumetric expanders they are characterized by an increased complexity related to the manufacturing of the screws geometry. In order to reduce wear phenomena, lubrication is of extreme importance and a separated oil lubrication circuit is often needed. In addition to that, given their increased size and volume, they seem suitable in the upper part of the 1 kW to 10 kW scale ORC-based unit. Major advantage is the larger technical maturity with respect to vane and scroll machines which make them the best choice in certain WHR applications [111].

Desideri et al. [112] experimentally tested an 11 kWel SSE in a recuperative unit using Solkatherm as working fluid to recover heat from a thermal oil circuit heated by a 250 kW electric boiler. Maximum isentropic efficiency achieved is 63 % with values ranging from 13% depending on the pressure ratio. A peculiar aspect outlined in the analysis is that the expansion device

shows a constant efficiency for pressure ratio above 5 which is a value close to the nominal value of the expander. Similar trends can be observed in [113]. In this case, an SSE is integrated in a basic ORC unit using thermal oil as upper thermal source. A separate oil lubrication circuit is used for wear prevention and leakages issues. Maximum power output is 8.35 kW with a total efficiency of 56%. Volumetric efficiencies showed a constant trend at different pressure ratios. Ziviani et al. have a long experience with these kind of machines. The same ORC-based unit comprising a recuperative HX, a multistage centrifugal pump and an 11kWel SSE have been tested in [114] and [115]. Main objectives of the studies were the performances variation of the unit with different fluids (Solkatherm and R245fa), the evaluation of the energy loss sources in the device through the calibration of a semi-empirical model and the elaboration of a simplified system model with a view to define a feed forward model predictive control. The empirical model showed in [114] has been compared by the same author to a deterministic model in [116] showing lower computational effort and errors on mass flowrate, power output and expander outlet temperature of 5%, 10% and 5 K respectively. Starting from the results of the analyses, Giuffrida [117] further improved the model performances, enhancing the modelling of mechanical and thermal losses reaching an error below 2% for all the parameters considered above. In a previous study, the aforementioned deterministic model has been used in order to compare the performances of an ORC unit for residential applications equipped with an SSE or a scroll expander. The results show that the SSE is able to produce a higher power output despite a lower isentropic efficiency of the plant. Nikolov et al. [118] tested a small scale twin screw expander. In this case oil is mixed within refrigerant R245fa. Compared to previous publications the expansion device is much smaller, with a maximum power output of 1.2 kW at an isentropic efficiency equal to 67%.

Few studies considered such devices for ICE-WHR applications. One of them is reported in [119]. The investigated ORC unit makes use of an SSE with R123 as working fluid for the recovery of thermal energy in the exhaust gases of a 270 kW diesel engine. In the considered range of operation, the exhaust inlet temperature varied between 420 °C and 480 °C. The SSE has been coupled to a dynamometer to understand the different behaviour at several torque values. Maximum power output reached 10.3 kW determining a break specific fuel consumption increase up to 1.5% demonstrating the

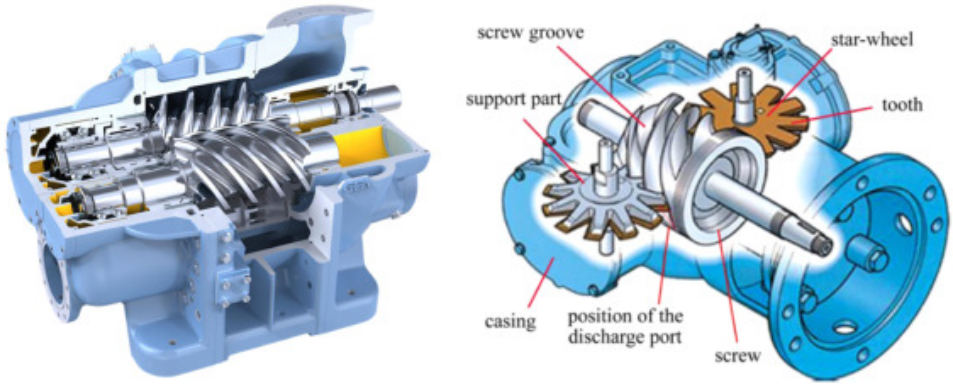

Figure 2.10: Single screw vs twin screw.

feasibility of such ORC unit in heavy duty engines. Totally different aspects have been investigated in [120]. In this case, experimental data taken from a SSE for a ICE-WHR application have been used in order to train a Back Propagation Neural Network for prediction and optimization purposes. The model has been coupled also to a genetic optimization algorithm to define best thresholds and weights of the model.

Possibilities of improvement in the geometry and design of twin screw expanders have been studied in [121] through CFD modelling tools. Transient calculations by means of a dynamic mesh modelling have been conducted considering air and R245fa as working fluids and different equations of state used. The indicated diagram has been reconstructed making possible the evaluation of leakages path and energy loss sources. It is outlined how geometry enhancements in this kind of devices have to be done on the suction port which are responsible for throttling losses. A different numerical approach has been followed by Bianchi et al. in [122] and [123]. A combined 1d/0d model built in GT-Suite platform has been considered for the evaluation of the indicated cycle. The aim of the studies was to investigate the capability of twin screw expanders to be used in TFC applications. In these cases a much greater mass flowrate is needed together with the capability of expanding a working fluid in saturated liquid or 2-phase conditions.

Scroll As almost every volumetric expander types also the scroll one is derived from its compressor counterpart. Scroll compressors in fact are known since a long time and are widely used in air compressor units, HVAC systems and air conditioning. In a not so recent review [124] scroll expanders

are classified based on their derivation in hermetic and open drive. In the first case the scroll compressor and its motor drive have a common shaft and are enclosed in the same casing while open drive compressors are usually used in a A/C conditioning unit on board and are mechanically coupled to the engine shaft.

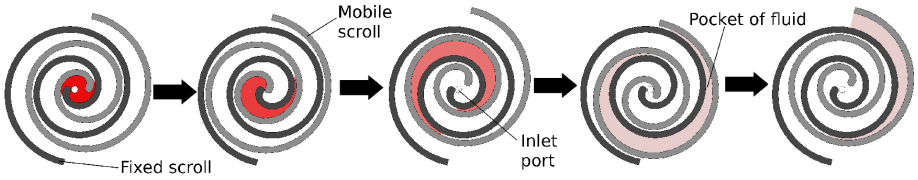

Figure 2.11: Scroll expander working principles. Fixed and orbiting scroll.

Working principle of scroll devices is illustrated in figure 2.11. In such machines a fixed and a orbiting scroll coexists. The relative movement between the two of them make the fluid evolve from the intake located at the center towards the exhaust, moving radially through the expanding chamber volume.

Further differentiation can be done based on the nature of the relative motion and the scroll geometry. In fact, the orbiting scroll representing the rotor of the expander is coupled to a camshaft. This coupling can be constrained geometrically determining a fixed clearance between the static and rotating scrolls. On the other side by means of a different mechanical coupling the orbiting scroll can be designed in order to move freely radially. In this way the sealing of the chamber volume is guaranteed by the centrifugal force which puts in contact the fixed and moving part. The result is an increased volumetric efficiency. The downside a greater need of lubrication to avoid wear phenomena. Researches related on the field of geometry are focused on variable wall thickness of the scroll and scroll tips shape which highly influences the efficiency of the intake phase [125].

Several experimental studies have been published over the years evaluating the performances of different kind of scroll expanders. Campana et al. [126] tested an open drive scroll expander in a reference ORC unit using thermal oil as hot source and R245fa as working fluid. Maximum isentropic efficiency reached 45 % at a shaft power output of 650 W. The experimental activities showed a low influence of the superheating degree on the expander performances. Moreover, it is found that rotational speed does not affect

the isentropic efficiency if the expander is operated at specific volume ratios near the nominal one. Ziviani et al. [127] evaluated the performances of a 5kWel open drive oil-free expander for a CHP application using water in the 85-100 °C range as hot source. Rotational speed of the expander have been varied between 800 RPM and 3000 RPM. Optimum point is achieved at 2500 RPM with 3.5 kWel produced for a specific volume ratio of 6.55. Experimental tests have been used to calibrate a semi-empirical model which showed that up to 20 % of shaft power is lost because of friction. In [128] an ORC unit recovering heat from thermal oil heated by a 40 kW boiler is evaluated. The novelty is represented by an innovative layout which make use of two scroll expanders in parallel operated in a similar manner. Up to 1.4 kWel are produced at 2700 RPM with a filling factor equal to 1.4 and a isentropic efficiency of 84 %. Further analyses show that thermal insulation of the system can increase the performances up to 30 %. The influence of Environmental conditions has been also investigated in [129]. Ambient conditions varies the cooling tower behaviour which in turn has effect on the expander outlet pressure and on its power output. Maximum power output has been 2.65 kW with an overall efficiency of the system equal to 5.5 %. However, it is assessed that the optimization of the cooling circuit could lead to a 100 % increase of the produced mechanical power. In [130] the generator of an oil free scroll expander is connected to a variable resistive load in order to understand the influence on its performances. It is found that best efficiencies are obtained for an optimal value of pressure ratio. This latter varies with the resistive load connected to the generator. Best efficiencies are achieved at 3500 RPM with a pressure ratio equal to 3.6 and a resistive load of 18.6 Ω. 565 W of electrical power have been produced with volumetric and isentropic efficiencies equal to 83% and 78% respectively. Declaye et al. [131] tested an oil free scroll expander in a wide range of operating conditions varying inlet and outlet pressures between 9-12 bar and 1.5-4 bar respectively. Maximum power and isentropic efficiencies are 2.1 kW and 75.7 %. Quoilin et al. [132] tested an hermetic scroll expander in order to calibrate a semi-empirical model of an ORC system. In the study is shown that it is possible to achieve a power output of 1.8 kW with an expander and system efficiency of 68 % and around 8% using hot air as hot source at 150 °C. Fanti et al. [133] evaluated the effect of flank clearances testing two scroll expanders with different values of this parameter using compressed air. The exhaust has been faced

to the atmosphere while the inlet pressure of the compressed air has been varied in order to fix the pressure ratio. Results show that higher clearances determine a lower volumetric and isentropic efficiency.

Modelling studies have also been used to study sources of loss in scroll expanders. As mentioned above, there are mainly three types of modelling approaches: semi-empirical, deterministic and CFD. One of the most popular one can be found in [134] where an extensive experimental campaign has been used to calibrate a semi-empirical model of a scroll expander. In this study, a simplified representation of the thermodynamic phenomena occurring in the device is used in order to evaluate with satisfying accuracy the mass flowrate, the shaft power and the outlet temperature. In second instance, the model can be used also to understand the mechanical and thermal power losses as well as the internal leakages. The same modelling approach has served as a basis in [135], where a further reduction of calibration parameters at the expense of the accuracy is found or in [136] where the same model is used in order to evaluate the possible replacement of conventional refrigerant with HFO or 4th generation ones.

Deterministic models are more difficult to elaborate but can give a greater information on the evolution of the fluid inside the chamber volume [137]. In [138], such modelling approach is used for the design of a scroll expander for ICE-WHR applications. The script is divided in two sub functions, each one responsible for a specific task: elaboration of the geometry and evaluation of the thermodynamic parameters. The required computational effort has been reduced with the use of lookup tables to lower the computational time required for the calculation of thermodynamic quantities.

CFD approaches are certainly more computationally demanding especially when applied to volumetric devices. In these cases, dynamic meshing and transient evaluations are required in order to capture intrinsic unsteady phenomena. However, given the qualitative representation of the phenomena and the information that can be extrapolated from them, they have been applied for intake optimization [139], radial leakages influence evaluation [140], asymmetric pressure gradients and unsteady suction process definition [141]

Vane and multi-vane Multi vane expanders are rotary volumetric expanders constituted by a stator and an eccentric rotor. The working fluid gets aspirated through a inlet port positioned radially or axially on the sta-

tor surface. During the intake, the working fluid entering the chamber see a increasing volume realizing an ideally iso-enthalpic, isobaric and isothermal transformation. Once the intake phase is finished, the expansion one takes place thanks to the eccentricity between the rotor and the stator. The closed volume full of fluid, during the rotation increase up to its maximum value right before the outlet port where the fluid exits during the exhaust phase. The sealing of the revolving closed volume is assured by sliding blades properly placed on guides obtained in the rotor block. During the rotation, the blades slide on the surface guides because of the centrifugal force. In this way the vane tip makes contact with the stator inner surface ideally sealing the system and preventing the working fluid leakage from a vane to the adjacent. The total number of vanes as well as the blades can vary as a function of the specific application and nominal power since a different trade-off between mechanical and volumetric aspects can exist due to this parameter.

Multi vane expanders are known since the 80s. In this period, scientific interest towards expansion machines for kW scale power systems was impelled by the first generation of Organic Rankine Cycles. Badr et al. was the first to describe this kind of expander [142] from a geometric a kinematic point of view. After that, several other studies followed regarding the intake and exhaust phases [143], mechanical issues [144], effects of lubricant and vane design [145], and operating conditions and optimization, [146], [147]. After this first outbreak, the interest towards energy efficiency measures gradually disappeared because of the revamped reliance on fossil energy sources. Only more recently the environmental issues related to the global warming caused by the increasing anthropogenic emissions of carbon dioxide into the atmosphere shifted the scientific attention towards new ways of producing energy and utilizing waste heat streams differently. Consequently also the studies on small scale expansion machines (i.e. rotary vane ones) for ORC power units reappeared. Vane expanders have the advantage of a simpler geometry with respect to other types as scroll and screw machines. The number of components is limited and this aspect determines a lower need for maintenance and a greater reliability of the expansion device.

Several experimental studies on different applications have been conducted over the years. Kolasinski et al. [148] tested a 300 W vane expander in a CHP unit for the recovery of the waste heat from hot water in the range of 55 °C to 80 °C. The experimental tests have been used to validate a CFD

model of the device in order to understand major sources of loss. Results show an indicated efficiency from 17.2% to 58.3% depending on the thermodynamic conditions of the working fluid at the expander inlet. Mascuch et al. [149] presented a design methodology for a CHP application. Legal and technical aspects are considered which are often neglected in numerical or experimental scientific studies. The ORC unit uses a 2 kWel vane expander with MM as working fluids. Preliminary tests on the pilot unit show a 3 kW maximum power produced with an overall efficiency of the unit around 2.5 %. Lubricating oil in air compressor units can reach temperatures high enough to be considered for a WHR application [150], [151], [152]. In [150] a 3 kW vane expander has been tested in a recuperative and a reference layout using R236fa refrigerant. Maximum power output reached 3.3 kW and 3.6 kW respectively. Reconstruction of the indicated cycle allowed the determination of the mechanical efficiency which varied from 70 % to 80%. In [151] the authors evaluated the expander performances variations due to leakages between the blade side and the stator comparing experimentally two expanders of the same type with different gaps. It is shown that higher gaps can reduce the expander mechanical power up to 20 % . In [152] instead, the effect of different thermal recovery is investigated. Mass flowrate of the refrigerant is varied, showing a local maximum in the expander and system performances. Overall efficiencies up to 8 % are achieved with 1.5 kW of produced mechanical power. A 180 W vane expander for a micro CHP unit is presented in [153] and [154]. Sensitivity analyses at different water inlet temperatures and expander rotational speeds are presented with R141b as working fluid. Maximum power output is achieved at the highest temperature of 90 °C and 4000 RPM. No expander efficiencies are reported. However, a 1.5 % overall efficiency of the system is reached.

Modelling and numerical activities have focused on several aspects and needs of this kind of expander in order to understand sources of energy losses and potential improvements. CFD tools are commonly used to understand the extent and the effects of leakages in the different gaps between the blades and the stator inner surface as well as between rotor faces and stator. The application is not straightforward since User Defined Functions are needed to adapt the mesh of the fluid volume domain which continuously evolve during the rotation. Examples are reported in [155], [156] and [157]. In the latter case, a 3D approach is used for a desalination application in a dual

chamber rotary vane expander to study cavitation phenomena.

Different methodologies consider 0D and 1D approaches. The advantage of these kind of tools are represented mainly by a lower computational cost. Moreover the definition of a 0d model allows its integration in much more complex systems involving several other components. Main disadvantage is the need for semi-empirical equations and coefficient which need experimental data in order to be properly calibrated. Vodicka et al. [158] developed a 1D model which has been further refined in [159]. The model is able to reproduce the real behaviour of the expansion device also thanks to a wide range of experimental data taken from a CHP unit using MM as working fluid. Leakages are described with an isentropic nozzle representation. In the first study it is outlined how the isentropic efficiency is not a functional parameter in order to describe the performances of a volumetric expander whose filling ratio has to be carefully assessed prior to any additional consideration. The refined model has been used to understand the performance decrease with different clearances. The study aims at evaluating the possibility to increase the tolerance range to reach a lower capital cost with little decrease in the efficiency of the machine. In [160] the evolution of leakages during the rotation of the expander are assessed through the use of a GT-Suite® model. Main findings are represented by the evaluation of the pressure - mass flowrate relation at different volumetric efficiencies as well as the pressure ratio - leakage one.

Different technologies have been studied in order to increase the performances of such devices especially regarding the range of operation extension. In [161], a variable expansion ratio rotary vane expander has been model through a 1D approach. The device can vary its expansion ratio acting on the discharge volume by means of a mechanical actuation. The study aims at defining the best operating conditions for different inlet pressures for a WHR-ICE application. A different approach has been used in [162]. In this case, an auxiliary injection port is considered in order to increase the indicated power. A genetic optimization algorithm is used to maximize power varying the dual port area and its radial angular position. The technology can be useful to increase the thermal recovery of the waste stream when the inlet pressure of the expander cannot exceed certain limits. Several other studies followed after this one comparing the original manufactured machine with the dual injection one at fixed pressure [163] and fixed mass flowrate

[164]. Finally the possibility to consider this kind of technology in the design phase rather than retrofitting a conventional existing one is considered in [160]. The main advantage of such choice would be the downsizing of the expander with similar performances which can be a useful feature in space-constrained applications. Results of these latter studies will be further described in the following chapter of these manuscript being them the results of experimental and theoretical activities conducted during this PhD period.

Piston In piston expander the evolution of the chamber volume is realized through an alternative motion of a piston inside a cylinder. The intake and exhaust phases are determined with the use of mechanically or electrically controlled valves which are able to vary the internal pressure ratio based on their actuation. Among the different kinds of piston expanders there are two main configurations namely reciprocating expanders and free-piston expander. In the first case the alternative motion is transformed into a rotation of a shaft through a camshaft. This latter can be coupled to an electric generator to produce electric energy. Free-piston expanders instead follow the same principle except that they make use of a linear alternator to produce electricity. In this way the use of a camshaft is avoided. The linear alternator produces an alternate current which can be rectified and connected to an electric load to vary the expander behaviour.

Piston expanders show decent isentropic efficiency and are able to utilize high pressure ratios exerted in the plant. However, several downsides exist. First of all, especially in reciprocating piston, the motion conversion can cause noise and vibration. Moreover, in both cases encumbrance can be really high which make it unfeasible for on-board applications. An additional feature which cannot be underestimated is that reciprocating expanders need a starter for the start up which adds up one more component to an already complex system which needs controls for the admission and exhaust valve actuation.

Wronski et al. [165] experimentally tested a reciprocating expander with servomotors for displacement-based valve control. They evaluated its performances using n-pentane as working fluid in an ORC-based WHR unit utilizing thermal energy of hot oil. Results show that the expander is able to operate at around 70% isentropic efficiency for a wide range of pressure

ratios.

Several feasibility studies have been conducted in order to understand the potentiality of free-piston expander but very few of them have been integrated in a working ORC unit. Li [166] tested a micro scale free-piston expander using compressed air. A reducer is used to fix the intake pressure and an intake timing control strategy has been implemented. The assembly is coupled to a linear alternator with a rectifier in series and a variable electric resistance. Effects on expander behaviour are studied at different loads and intake pressure showing an isentropic efficiency up to 30 %. Similar analyses, using micro scale free-piston expander using compressed air, can be found in [167] and [168]. In the latter case, a combined genetic algorithm and artificial neural network modelling approach has been used and validated against experimental data. Moreover it is found that velocity, output voltage and power output are proportional to supply pressure and electric resistance load. Gusev and Ziviani [169] tested a prototype of free-piston expander in a 10 kW scale ORC unit. The aim of the study was to identify the cogging and frictional force, which are hardly evaluable analytically, to define a control model based on mapping of experimental data. No power output and performances are reported.

Han et al. [170] investigated a five cylinder radial piston expander for WHR in Internal Combustion engine. The expander has been tested with R245fa. Despite the dimensions of the experimental apparatus, the device has been able to produce only 280 W with an isentropic efficiency near 20%. Overall WHR unit efficiency has been 2%. A similar device with three pistons has been tested in [171] and [172] with R134a producing up to 1.3kW. The obtained dataset has been employed to calibrate a polynomial fitting model and a semi-empirical one. This second approach showed similar performances in the calibration range. However extrapolation capabilities are much better.

Finally few studies reported comparisons between piston expanders and other types. In [173], a piston expander is compared to a single and a double stage screw expander. The analysis is conducted through performance maps. The application is the waste heat recovery from the exhaust of a diesel engine. The thermodynamic analysis shows better performances of the screw expander with a greater power output. However the economic investigation showed that piston expanders have higher potential which could justify their use considering that these devices are in an early development stage for ORC

applications. Dumont et al [174] experimentally tested a scroll, root, screw and swash plate piston expander in a 5 kW scale ORC-based WHR unit. Best performances in terms of efficiency are achieved by the scroll expander, followed by the piston and screw types.

Chapter 3

Experimental layout: top and bottom unit

3.1 Engine characteristics

The experimental test bench top unit is constituted by an Iveco F1C, a turbocharged diesel engine used for light-duty and heavy-duty applications. Maximum power output and torque are 130 kW at 3250 rpm and 400 Nm at 2000 rpm. Other characteristics are listed in table 3.1. The engine shaft in mechanically coupled to an AVL dynamometer through an universal joint which limits the maximum allowable torque at 200 Nm limiting the engine load around 50 % of the maximum power output. The cooling needs of the engine are satisfied through a cooling water closed circuit which serves also the other experimental units in the laboratory of the University of L'Aquila with different branches operating in parallel. The cooling water exits are then mixed before entering the cooling towers. The AVL dynamometer allows the control of the engine operating conditions. These latter can be defined setting up the speed and torque of the engine or, in equivalent manner, the engine speed and load. The first mainly influences the intake air which determines the mass flowrate of the exhaust gases entering the evaporator of the bottom unit, while the second (torque or load) varies the exhaust gases inlet temperature. However, being the engine turbocharged, the variation of torque can cause also the variation of the turbocharger equilibrium causing a slight different flowrate for the same engine speed.

Thermodynamic parameters of the engine are measured through pres-

Engine parameters	
Maximum power	130 kW @ 3250 rpm
Maximum torque	400 Nm @ 2000 rpm
Displacement	2988 cc
Cylinder number	4 in line
Valves number	16
Injection system	2nd generation BOSCH Common rail unijet
Stroke	104 mm
Bore	95.8 mm
Compression ratio	19:01
Injection order	1-3-4-2

Table 3.1: Parameters of the engine used in the experimental test bench.

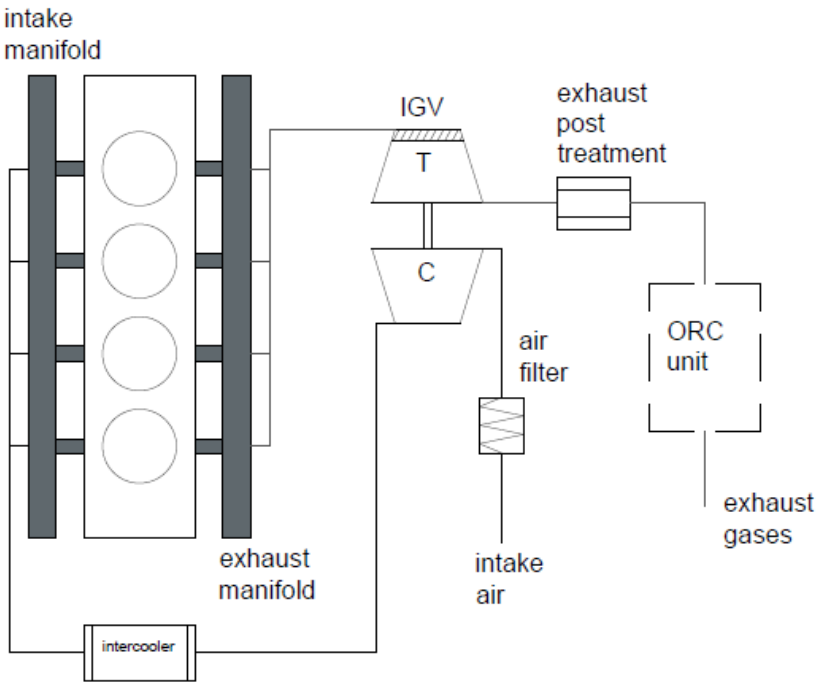

Figure 3.1: Schematic diagram of the experimental test bench layout.

sure and temperature sensors placed downstream and upstream each component. In addition to that, ECU parameters can be accessed through software ETAS-INCA V5.4. The ORC-based unit is placed downstream the post treatment unit of the exhaust gases. In this way, even if the available thermal energy to be recovered is lower, their functionality is not compromised. In figure 3.1 a schematic diagram of the engine layout with some of its components is reported. A blower at the ORC evaporator exit facilitates the exhaust gases expulsion to the atmosphere.

3.2 ORC unit

The ORC-based unit experimented in the laboratory of University of L'Aquila is thought for the recovery of the thermal energy of the exhaust gases of the aforementioned engine. Details of the experimental layout, components as well as the measurement instrumentation will be detailed in the following sections.

3.2.1 Layout and components

The layout configuration of the ORC-based unit is represented in figure 3.2. The unit is composed of a pump, an evaporator, an expander and a condenser. No recuperative heat exchanger has been used. Its use can be beneficial to increase the thermal efficiency of the plant through the partial recovery of the thermal energy content of the working fluid exiting the expander. However, in this case, given also the thermodynamic characteristic of the working fluid, little thermal energy is available in this point and even in the best case scenario little power could be exchanged. In addition to this preliminary consideration, the recuperative HX is crossed in its hot side by low pressure vapor. This means that it can produce high pressure drops, determining an higher back-pressure at the expander outlet and consequently reducing the maximum isentropic power output. For all these reasons, it has been decided not to integrate this component in the unit.

An additional component is constituted by a tank positioned upstream the pump. A plenum is a passive component, which fulfils several functions. First of all it ensures that the fluid entering the pump is in liquid state, avoiding cavitation phenomena especially at high revolution speed of the pump. An additional feature is that as long as saturated liquid conditions

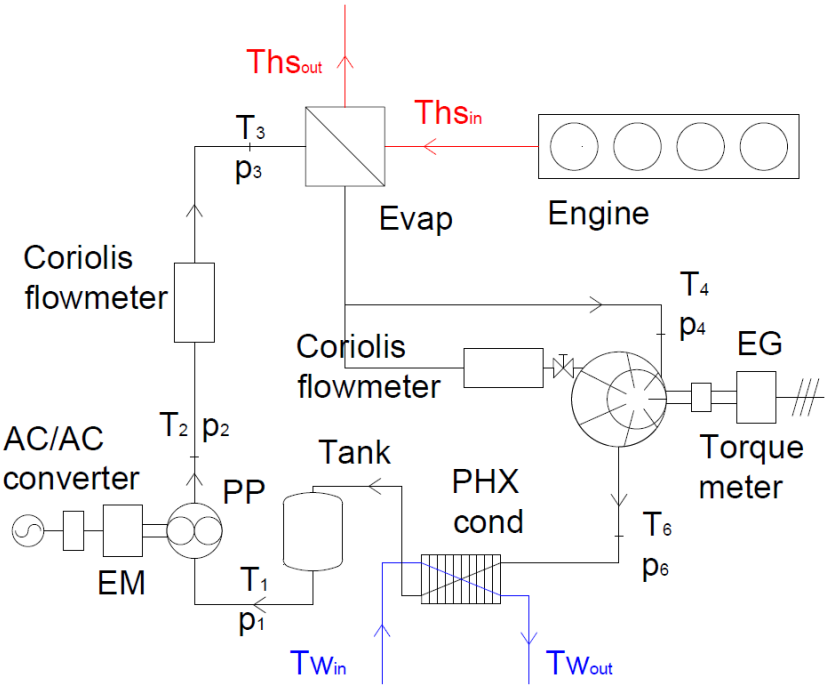

Figure 3.2: Schematic diagram of the WHR unit.

exist inside it the minimum pressure in the plant is independent from the total charge of working fluid inside it. Moreover, the volume increase of the plant reduces the condenser pressure which results in higher pressure ratios available for the expander. All these functions help to guarantee a more stable functionality of the pump.

Pump

During normal operating conditions the pump elaborates a subcooled liquid ensuring the circulation of a certain working fluid mass flowrate depending on its rotational speed. Volumetric pumps have different operating characteristics with respect to centrifugal ones. In particular, at least in an ideal case, positive displacement types allows to elaborate a certain mass-flowrate at fixed rotational speed in an independent manner with respect to the hydraulic resistance of the circuit. This means that characteristic curves in the pressure head - flowrate diagram are represented by vertical lines. In real cases, volumetric losses determine a recirculation of the flowrate inside the device producing a slight anti-clockwise rotation of the curves. At higher

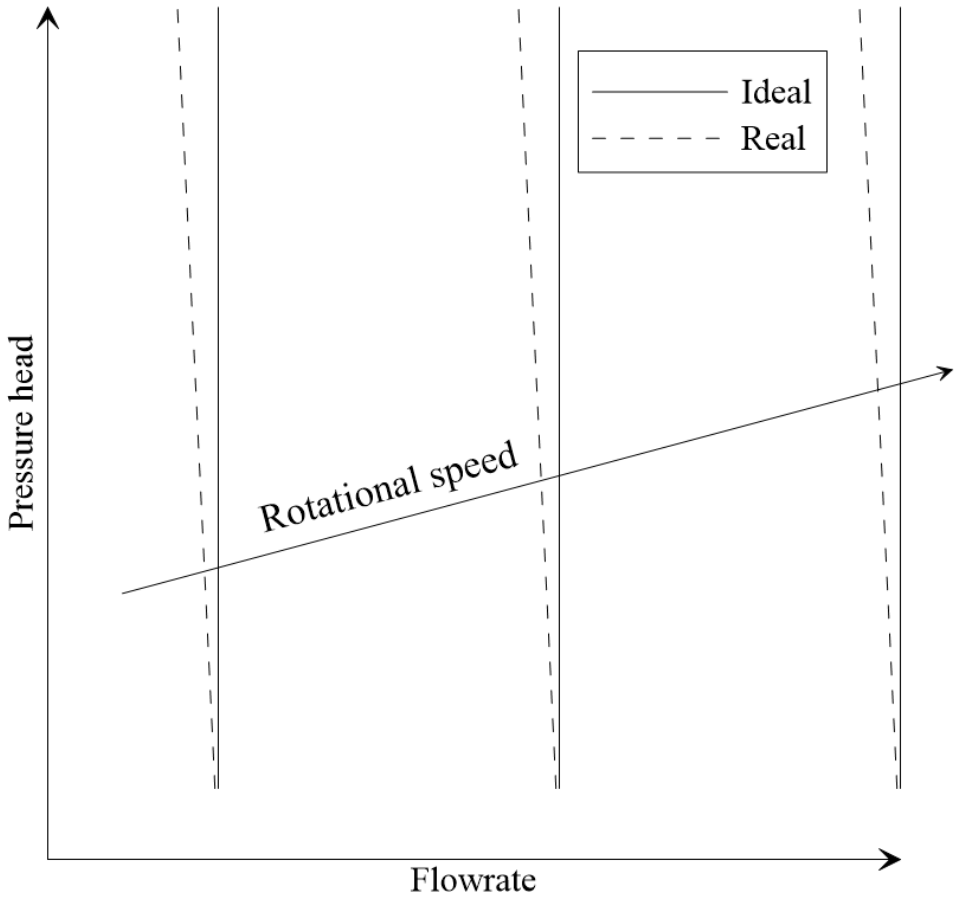

Figure 3.3: Ideal vs real characteristic curves of a positive displacement pump.

pressure head, the backflow mass flowrate increases, reducing the elaborated mass flowrate (Figure 3.3). This characteristics is quite useful in ORC systems, making it possible to control the mass flowrate in the circuit in a much easier way.

The pump utilized in the tested system is a gerotor pump, whose main advantages are represented by a low space requirement and robustness in its regulation. As in volumetric expanders, in this case the compression of the working fluid till to the exhaust pressure is obtained through an evolving chamber volume realized by means of an outer and inner rotor whose teeth engage on each other. The specific model is KP20-11.2 manufactured by Casappa ®. It is realized in cast iron to withstand high operating pressure (up to 275 bar). These kind of systems are often utilized in applications

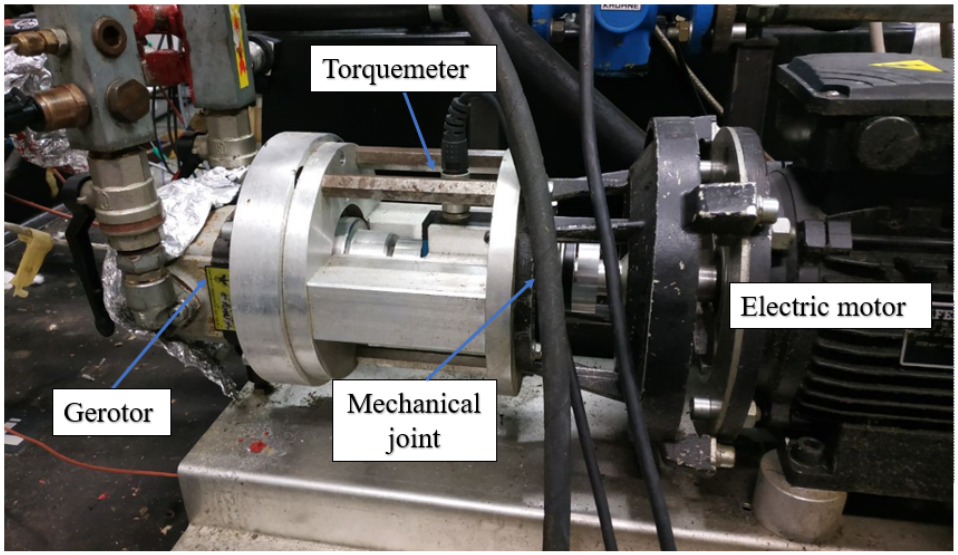

Figure 3.4: Detail on the mechanical coupling of the gerotor pump.

where contamination, encumbrances and noise represent critical aspects.

The considered pump is mechanically coupled to a 1 kW asynchronous electric motor (Figure 3.4). Between them, a torque-meter allows the evaluation of the mechanical power. The speed control is realized through a frequency converter connected on one side to the electric network and on the other to the electric generator.

Condenser

The condenser heat exchanger has the role to make possible the heat exchange between the working fluid and the cold source. The working fluid in superheated conditions enters the hot side inlet port to be desuperheated, condensed and finally subcooled down to a certain degree. In applications where cooling water is used as cold source plate heat exchangers represent the best solution in term of hydraulic and thermal performances. Moreover, they are characterized by a low volume to heat transfer area ratio, meaning that high thermal power can be exchanged also in space constrained applications. A picture of the condenser of the ORC-based unit together with its main characteristics are reported in table 3.2 and figure 3.5. It can be seen how glass wool has been used to reduce ambient losses.

Condenser parameters		
Parameter	*hot side*	*cold side*
Pressure drop [mbar]	170	30
Channel number	24	25
Ports diameter [mm]	39	39
Thermal capacity	16 kW	
Heat transfer surface	4,46 m2	
Number of plates	50	

Table 3.2: Condenser characteristics

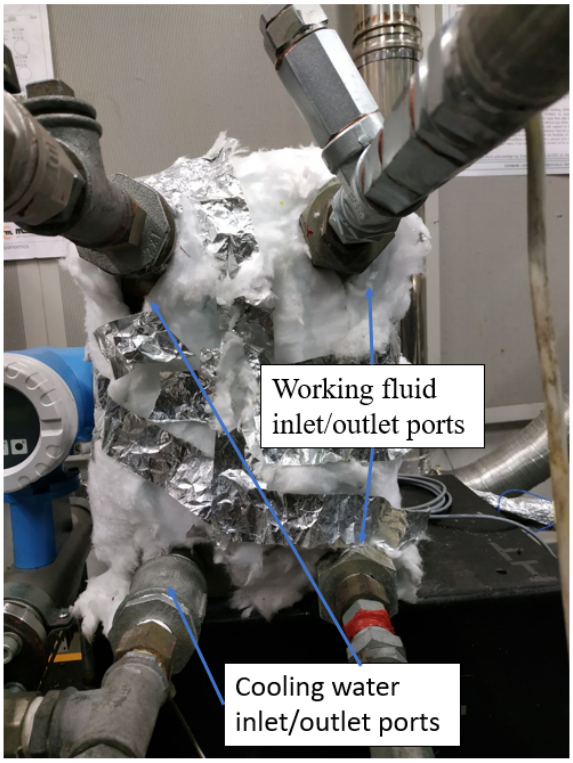

Figure 3.5: Plate heat exchanger type condenser

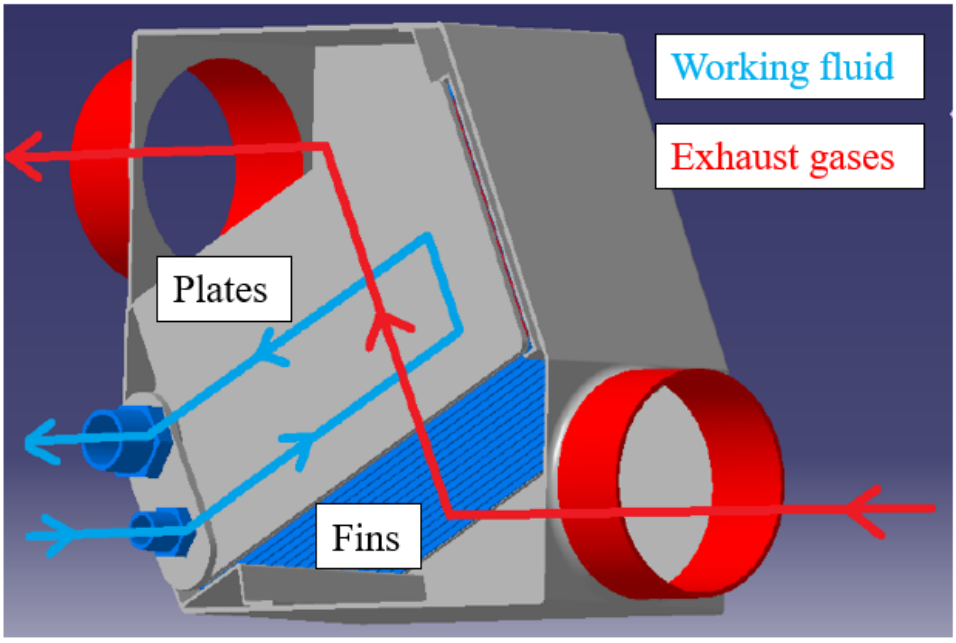

Figure 3.6: 3D cad model of the plate and fins evaporator with details on hot and cold side fluid passages.

Evaporator

The evaporator of an ORC-based unit is one of the most important components. It determines the thermal inertia of the unit in applications where the hot source shows significant variations in time and it has to ensure high thermal effectiveness together with low pressure drops both at hot and cold sides. The tested evaporator is a plate and fins heat exchanger whose characteristics are depicted in figure 3.6. Nominal thermal power exchangeable is around 30 kW. The exhaust gases flow through 5 inches ports crossing a set of 15 parallel plates with louvered fins between them. Their role is to increase the heat exchange area and the heat transfer coefficient due to a greater turbulence of the exhaust gases. The working fluid instead enters the heat exchanger through a 16 mm inlet port and gets gathered in a common manifold (figure 3.7) before being split between plates in a parallel configuration. The cold side passage represented in figure has been assumed based on common sense since its identification would have required a destructive inspection that eventually would have compromised the heat exchanger functionality.

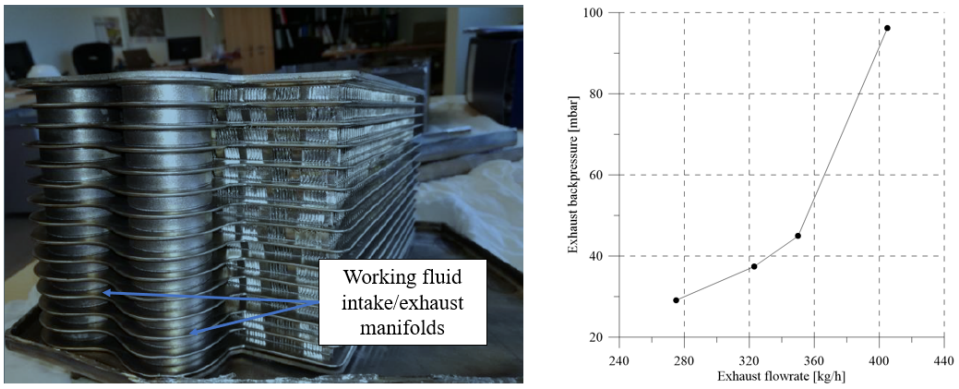

Figure 3.7: Intake and exhaust manifolds details of the evaporator and engine backpressure at different inlet air flowrates.

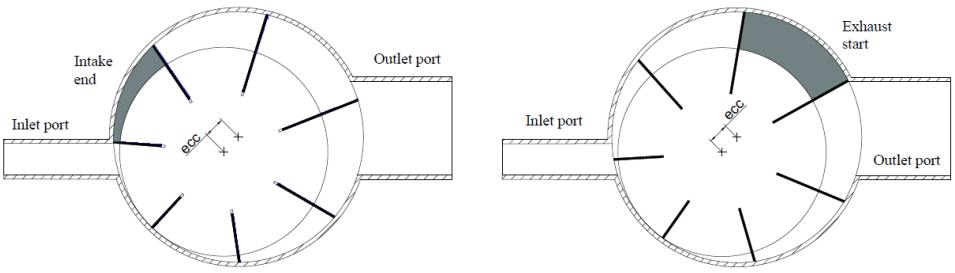

Figure 3.8: Principle of operation of a rotary vane expander, intake, exhaust volume and eccentricity.

The main advantages of this kind of device with respect to more conventional ones as plate heat exchangers and shell and tubes are represented by a lower volume to heat transfer area ratio which eventually contributes to the reduction of encumbrances at a fixed thermal power exchanged and, even more, the reduction of the exhaust pressure drop which can cause the increase of the backpressure effect on the engine. This latter aspect in fact, increases the work needed for the expulsion of the exhaust gases reducing the engine performances. A preliminary experimental analysis has been conducted in order to evaluate this aspect. The engine load has been varied from 20% to approximately 60% resulting in different flowrates. Maximum pressure drop measured in the heat exchanger has been under 100 mbar which has shown non detrimental effect on the engine efficiency.

Expander

The tested expander is a sliding vane device manufactured by Mattei SPA ®. As aforementioned in the previous chapter, this kind of machines have been used since a long time in the air compression field. The principles of operation are partially described in figure . The fluid entering through the inlet port fills a chamber volume delimited by the blades of the rotor. In ideal conditions, during the process the temperature and pressure of the working fluid remains constant. The filling process in the considered vane ends at the point depicted on the left side of the figure. At this point, the volume is closed and it is constrained inside a revolving chamber (vane) which increases its volume during the rotation, expanding the mass of fluid inside and producing work. When the chamber faces the outlet port, the expansion process is finished and the fluid is conveyed towards the condenser. Depending on the pressure at the expansion end, an isochoric transformation takes place if the pressure at the expansion end is different from the one exerted by the circuit. In particular, if this pressure is below the condenser one, an overexpansion takes place reducing the specific work. On the other hand, if this pressure is greater, an under-expansion happens. This case is not as detrimental as the previous one but reduces the amount of obtainable work and the isentropic efficiency. The ratio between the chamber volume at the expansion end and the one at the intake end defines the built-in volumetric ratio which represents the maximum volumetric expansion ratio achievable in ideal conditions.

$$\beta = \frac{V_{in}}{V_{out}} \tag{3.1}$$

In the same conditions the mass flowrate elaborated by the device can be defined as:

$$\dot{m}_{wf} = N_v \rho_{in} V_{in} n \tag{3.2}$$

where N_v, ρ_{in}, V_{in} and n represent the vane number, the working fluid intake density, the chamber volume at the intake end and the rotational speed of the expander respectively. The ratio between the theoretical mass flowrate expressed as in equation 3.2 and the measured one is defined as volumetric efficiency. In an alternative way scientific studies often consider

the inverse of this ratio calling it filling ratio.

Main characteristics of the experimented expander are reported in table 4.1. Inlet port is radial which means that the opening has been created on the stator outer diameter. On the other hand, the exhaust is placed axially on the stator surface. The expander is mechanically coupled to a 1.5 kW 2 pole pairs asynchronous generator connected to the electric network. Given the electric network frequency, the expander rotational speed is fixed at 1500 RPM. A torquemeter is used to measure rotational speed and torque which allows the evaluation of the mechanical power output.

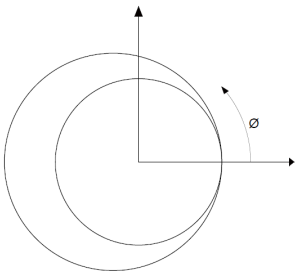

Figure 3.9: Reference for the identification of angular positions

RVE parameters	
Number of Chambers	7
Stator Inner Diameter	75.9 mm
Rotor Outer Diameter	65 mm
Eccentricity	5.45 mm
Chamber Width	60 mm
Vane Thickness	3.96 mm
Vane Length	17 mm
Vane Weight	29.5 g
Intake port opening	4.4°
Intake port closing	48°
Exhaust port opening	180°
Exhaust port closing	320°

Table 3.3: Characteristics of the sliding vane rotary expander

In the same table the port opening angles are reported considering the absolute reference represented in figure 3.9. The reference axis is placed in the line crossing the stator and rotor center and the point of tangency between them. Their angular position univocally defines the intake and exhaust chamber volume.

Auxiliary intake port definition After a first experimental campaign on the single intake expander an auxiliary port has been added. Its position has been defined according to a preliminary optimization algorithm to maximize the producible mechanical power. The effect of an additional intake port is the increase of the pressure inside the vane. In the original case, the pressure starts decreasing when the expansion process takes place. The idea behind the use of such a system is to sustain the chamber pressure even after

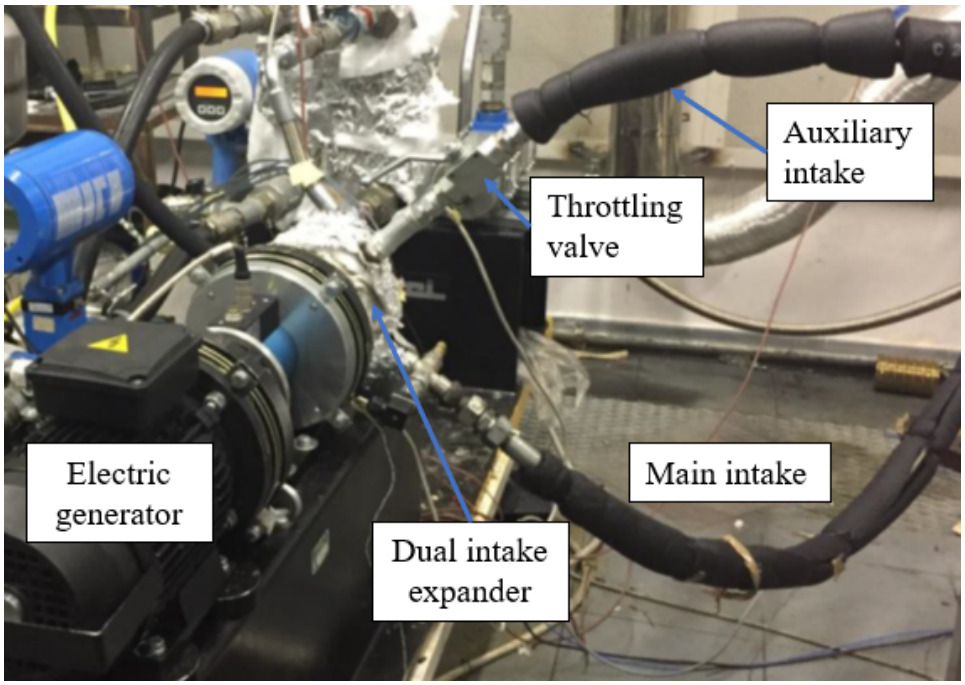

Figure 3.10: Experimental layout of the dual intake expander configuration

the main suction process is finished to have a higher indicated power. An additional flowrate has to be provided by the pump increasing its rotational speed to realize such effect.

From a technical point of view, the use of a double intake required the installation of a 1 inch diameter additional branch after the evaporator. During the operation of the system, the working fluid exiting the evaporator is facilitated to flow towards the lowest pressure branch. To prevent this phenomenon a valve has been placed right next to the auxiliary port to throttle the flow increasing the pressure at the end of the branch and limiting the flowrate in the same pipe. A picture of the investigated system in this second configuration is presented in 3.10.

Instrumentation

Most relevant quantities have been measured in specific points of the circuit. Pressure and temperature transducers have been place downstream and upstream each component. Two Coriolis flowmeters have been used to measure the total mass flowrate downstream the pump and the one flowing through the auxiliary line of the expander. An electromagnetic volumetric

sensor	type	model	range	uncertainty	Output
p1	membrane	Wika	0-16 bar	0,3 bar	4-20 mA
p2,3,4	membrane	Gems	0-25 bar	0,25% fs	4-20 mA
pz1,2,3	piezoresistive	Kistler	0-10/20 bar	0,1 % fs	4-20 mA
Temperatures	K-type	-	-	0,3 °C	-
Texp/ω_{exp}	-	Kistler 4503A	0-10/50 Nm w 0-12 kRPM	0,02 Nm 1 RPM	0-5 V frequency
Tpump	-	Kistler 4502A	0-10 Nm	0,02 N	0-5 V
$\dot{m}_{wf}$	Electro-magnetic	Krohne IFC 080	0-5,4 m^3/h	0,30%	4-20mA
$\dot{m}_{cw}$	Coriolis	Promass 80	0-2000 kg/h	±0.15%	4-20mA

Table 3.4: Measurement instruments details.

flowmeter has been used for the cooling water flowrate. Torquemeter have been placed between expander and electric generator shafts. Same coupling has been done for the pump.

In order to measure the indicated cycle of the expander three piezoresistive pressure transducers angularly spaced have been placed on the stator. A closed circuit of water-glycol equipped with a small circulation pump has been used to refrigerate the pressure sensors and not to compromise their measurement accuracy. The main advantage of this kind of sensors is the possibility to operate at higher rate with respect to conventional diaphragm type.

Main characteristics of the measurement instruments are reported in table 3.4. All signals are converted through an electronic circuit in order to have a voltage output before entering the acquisition system.

DAQ acquisition system

The DAQ acquisition system is composed of multiple components. The main one is the chassis PXIe-1073 which is responsible for the communication between the hardware devices and the computer through a RS232 port. The chassis can host six different modules. In our case, two modules have been used for the acquisition and management of temperature signals (PXIe-4353) and analog and digital input (PXI-6225). Main task of the chassis is the synchronization of signals coming from the different modules and characterized by different rates. From this point of view, the thermocouple module need a lower sampling rate. Signals are smaller and the conditioning unit requires more time in order to integrate the signals. This issue determines a trade-off between resolution and speed as it can be seen in figure 3.11.

Highest speed allowed is 90 sample per second at the lowest resolution.

Sample Rate (S/s)

Maximum Channels per ADC	1	10	20	30	40	50	60	70	80	90
1	1	1	2	2	3	3	3	4	4	4
3	1	2	3	4	4	5	5	5	5	5
5	1	3	4	5	5	5	6	6	6	6
7	1	4	5	5	6	6	6	6	7	7
9	1	4	5	5	6	6	6	7	7	7
11	1	4	5	6	6	7	7	7	7	7
13	1	4	5	6	6	7	7	7	7	7
15	1	5	6	6	7	7	7	7	7	7
17	1	5	6	6	7	7	7	7	7	7

1 = High-Resolution Mode, 7 = High-Speed Mode

Figure 3.11: Resolution vs speed relation for thermocouple signals.

On the other hand, the module which receive the voltage signals must work at much higher frequency. The evaluation of the indicated cycle need a sampling rate almost equal to 4500 Hz which results in one sample every two angle degrees of rotation at a speed equal to 1500 RPM. This resolution has been considered a good compromise between data number and accuracy of the reconstruction. The analog input modules can guarantee a maximum sampling rate equal to 6000 Hz if all the available channels are used in differential mode. It can be noted that different acquisition rates are needed assuring at the same time a correct synchronization. Each module has its own clock. The matching between them is ensured through an external reference clock at 10 MHz.

Software interface Once defined the hardware, a software interface has been built to allow the communication with the instruments. Since the chassis and the external modules are all National Instruments devices, a Labview software interface has been built. The block diagram related to the configuration is represented in figure 3.12.

Labview allows a block programming. Each object has its own inputs and outputs however, they can be separated in groups. Each of them has a role. Looking at the diagram, two tasks are created, one for each module. After the definition of the operating channels, two different tasks are created,

one for each module. The next phase was the configuration of timing and trigger control. At this point, the tasks can be started and the system begin acquiring data through the while loop. A Read subvi has been created to visualize data online and control the ORC parameters. In addition, TDMS files are created to store the acquired data. At this point acting on the stop button of the while loop, tasks are cleared and a new acquisition can be done.

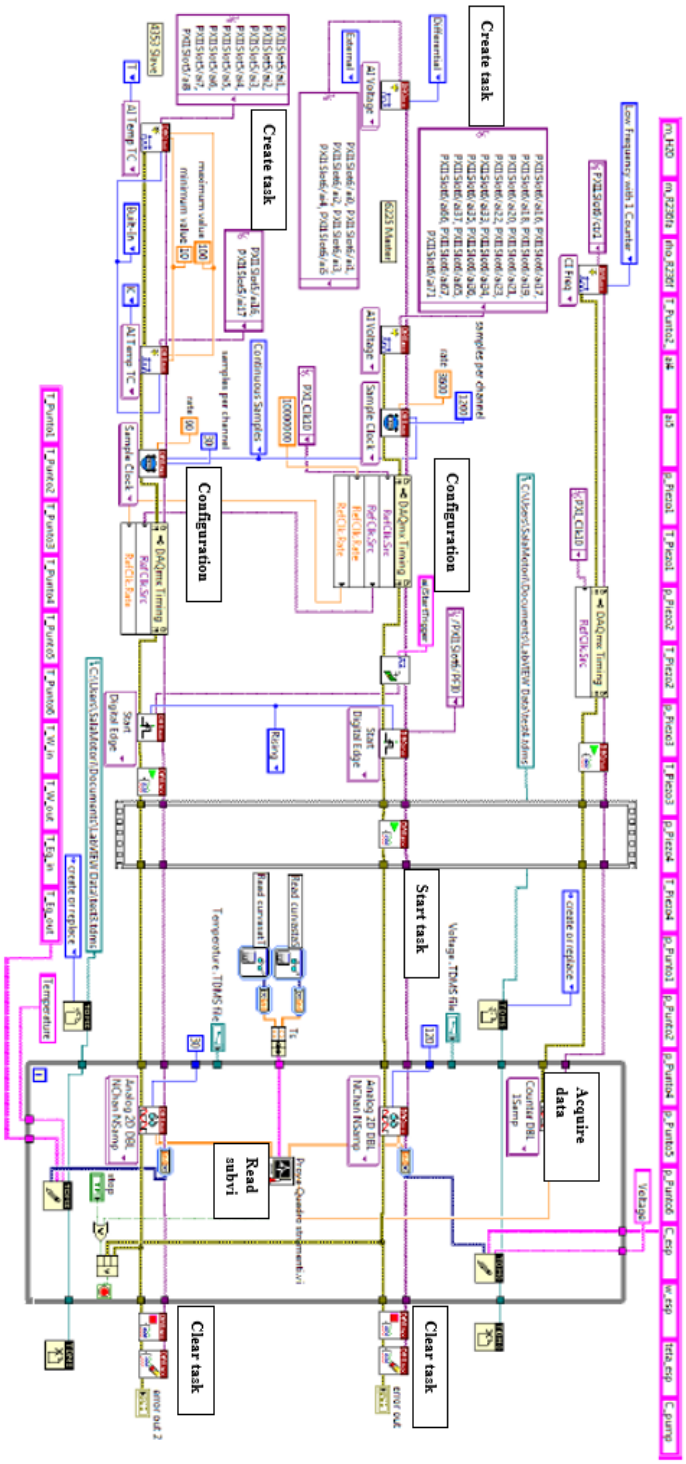

Figure 3.12: Software interface block diagram.

Chapter 4

Dual intake port experimental analysis and comparison

4.1 Introduction

In this chapter the experimental activity conducted for the characterization of the single and dual intake port vane expander will be reported. Main results will be detailed together with a full explanation of the test procedure. Particular emphasis will be given to evaluation of the indicated cycle. The determination of the indicated power allows to evaluate indicated and mechanical efficiency. The knowledge of these parameters made possible the development and calibration of a software platform which is used as a basis for further investigations that will be exposed in the next chapters.

4.2 Test procedure

An experimental test procedure has been adopted in order to ensure the repeatability of the results. Since the evaluation of the expander performances has been the primary focus of the analysis no particular attention has been given to the engine operating point. In this context it has been used only as a hot gases generator.

After the engine start up, a warm-up period of approximately ten minutes has been waited to make the engine approach a first steady state condition at low load. During this period the cooling water pumps are active for adequate cooling of the engine and to prevent the working fluid in the ORC

system to increase its temperature. During the warm-up phase, the engine oil temperature reach suitable values around 70 °C.

When this first stage is fulfilled the engine load can be increased. Torque and speed of the engine are set starting from low load region. Once the operating point was chosen and reached, exhaust gases temperature was monitored through the Labview software interface of the ORC-based unit. Approximately after five minutes the steady state regime is reached. In this case, the exhaust evaporator inlet temperature does not show significant variations. In the meantime, the pump of the ORC-base unit is activated setting the output frequency of the electric drive. A certain working fluid mass flowrate is elaborated. The expander is initially still. Due to this, expander inlet pressure does not increase and the maximum and minimum pressure of the plant are given by the pressure drops in the heat exchangers and connecting pipes between components. Being the expander still, it acts as a through-flow with no hydraulic resistance. As the working fluid heat up, when the enthalpy content of the working fluid at the expander inlet is sufficient, the expander starts rotating. At this point, an increase of the maximum pressure of the plant can be observed. The asynchronous electric generator is connected when it approaches 1500 rpm producing mechanical and electric power. After reaching the ORC-based unit steady state conditions, identified when pressure and temperature signals do not show meaningful oscillations, data are acquired. After each variation of engine load or pump speed the procedure is repeated always paying attention to the achievement of a steady state regime, both for the ORC-based unit and the engine.

Acquisition rate are 90 Hz and 4500 Hz for temperature and pressure signals respectively. As aforementioned in the previous chapter, thermocouple modules need a longer time in order to condition the signal and filter noise since the signal power is much lower. Concerning the pressure acquisition rate, a higher value is needed to elaborate the indicated cycle. Assuming an average rotational speed of the expander equal to 1500 rpm, such rate determines 1 pressure signal every two degrees of rotation of the expander which is considered a good compromise between resolution and number of data. The acquisition period has been fixed at five seconds. Considering the same parameters, over a hundred indicated cycles can be acquired and averaged.

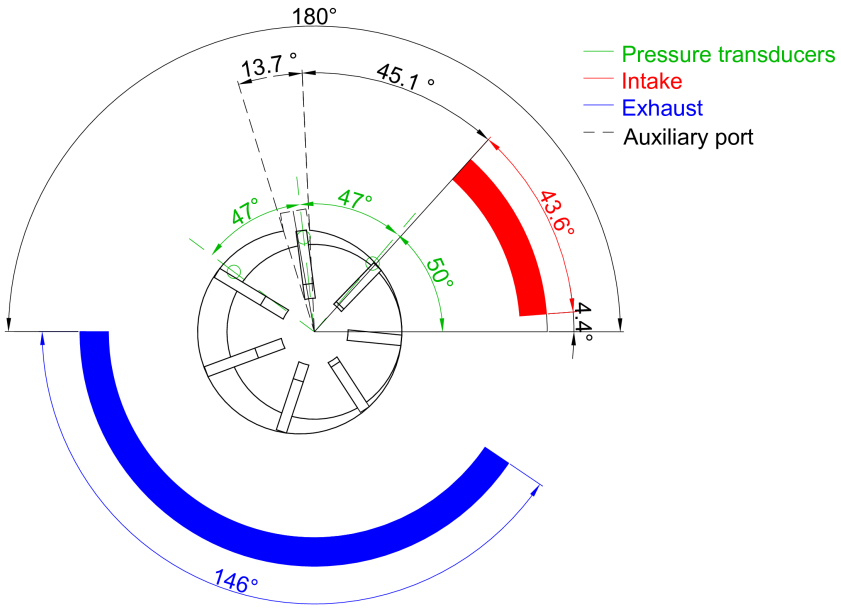

Figure 4.1: Rotary vane expander intake, exhaust and pressure sensor angular positions

4.3 Indicated cycle reconstruction

To understand the procedure for the reconstruction of the indicated cycle profile, the angular positions of pressure transducers are reported in figure 4.1. The reference axis is determined by the point of tangency between rotor and stator. The first pressure transmitter is positioned at 50 degrees. The other two are equally spaced with an angular interval equal to 47°. Since each vane has an amplitude equal to 51.4 degrees, this means that there are intervals with overlapping of pressure measurements which are needed in order to understand when to switch between a pressure signal coming from a transducer and the following one.

The positioning allows to evaluate the whole expansion process, part of the intake phase, and the beginning of the exhaust one. The remainder is evaluated considering an isentropic transformation or using the results of the CFD 1-D model which will be described in the following sections. In this latter case, dynamic phenomena are taken into account resulting in a much less regular course of the discharge phase.

Raw data are elaborated through an algorithm built in Matlab. The aim is to turn the temporal axis in an angular position first and a volume after. The algorithm must deal with the absence of an encoder which would have measured the absolute angular position. The first step is the definition of the angular speed of the expander. Measurement of the torquemeter could be slightly inaccurate and even a small difference between the real and the measured parameter determines a cumulative error which makes the task impossible. For this reason, pressure signals coming from the first sensor are fitted with a sinusoidal function. The pulsation of this function can be related to the expander rotational speed as follows to compensate the difference with the actual speed in each cycle without incurring cumulative errors.

$$n = \frac{\Delta\theta_v}{1/f_{sn}} \frac{60\ s}{1\ min} \frac{1\ round}{360\,\mathrm{deg}}\ RPM \tag{4.1}$$

where:

$$\Delta\theta_v = \frac{360}{N_v} \tag{4.2}$$

In the above equations $\Delta\theta_v$ represents the angular amplitude of each vane, N_v the number of vanes and f_{sn} the frequency of the sinusoidal function fitting the pressure signals. n is the average expander speed.

Once the mean speed was known, a time window can be defined based on the period of a cycle. Once determined, each consecutive cycle can be averaged with the first one. From the rotational speed and the acquisition rate, an angular increment can be associated to each pressure data. The knowledge of the angular positions of the pressure transducers allows to switch from one sensor to another in order to follow the evolution of the working fluid. So for example, the first part of the indicated diagram is determined based on the pressure outputs of the first sensor, while the expansion phase is based on the second one. Being the interval between them lower than the vane amplitude, the consequent overlap allows this operation. At the end of the procedure, two vectors containing pressures and corresponding angles values are built. The evaluation of the chamber volume is straightforward based on the expander geometrical characteristics:

$$V_v(\theta) = f(D_{stat}, D_{rot}, W_{exp}) \tag{4.3}$$

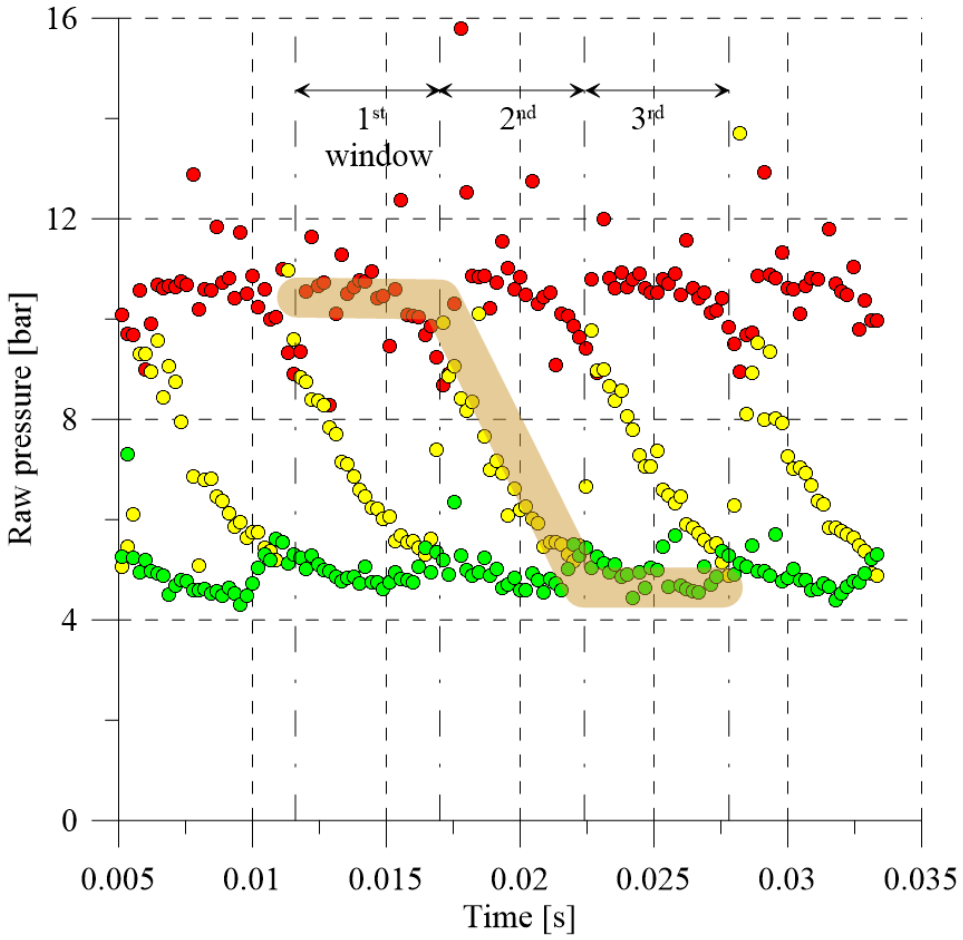

Figure 4.2: Raw pressure signals before indicated cycle reconstruction.

where D_{stat} and D_{rot} are the stator inner diameter and the rotor outer diameter respectively, while W_{exp} is the expander axial length.

The results of the procedure are represented in figure 4.4. It is worth noting how the indicated cycles average determines the elimination of outliers and a smoother profile. It has to be said that the blade tip passage on the pressure sensor determines a squeezing phenomenon which ultimately result in a measured pressure higher than the expander inlet one. This anomaly is taken into account in the algorithm. Although it is useful for the determination of the angular position reference, these outliers are not considered during the averaging process.

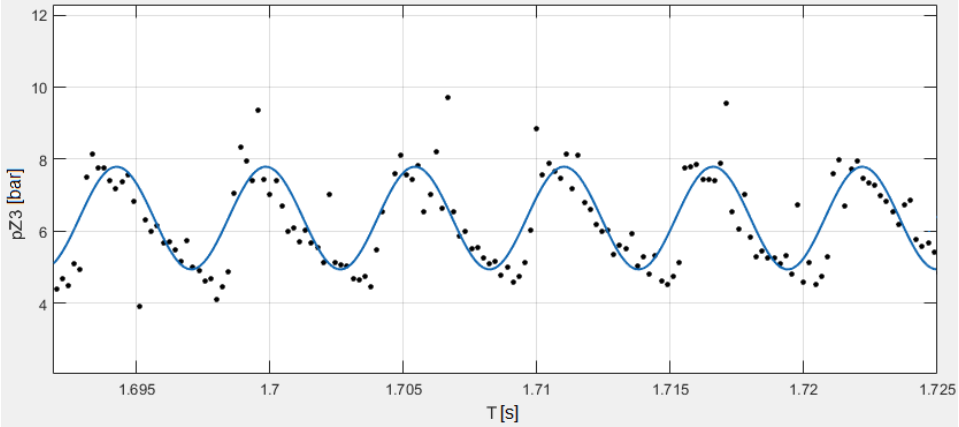

Figure 4.3: Example of pressure measurements of the first piezoresistive pressure transducer and sinusoidal fitting.

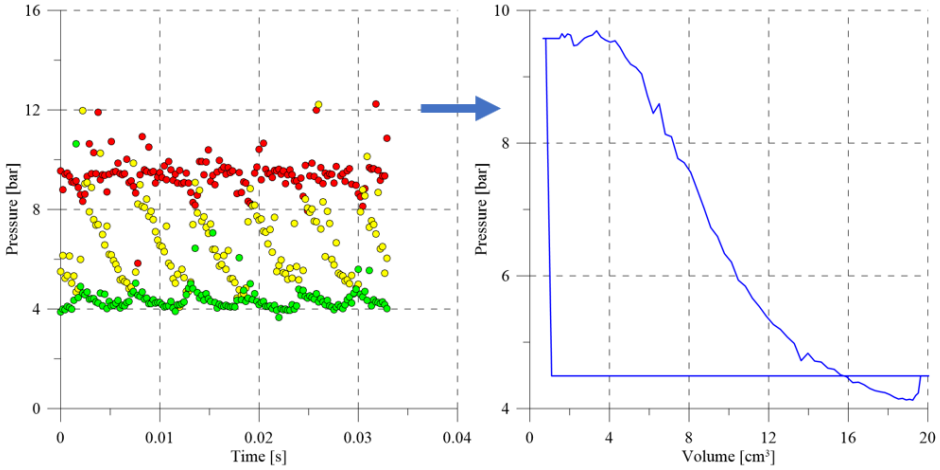

Figure 4.4: Example of the indicated cycle reconstruction procedure.

4.4 Single intake experimental assessment

A first experimental campaign on the OEM expander with a single intake has been conducted following the test procedure described above. The aim of the tests was the evaluation of the pressure - working fluid flowrate relationship together with the expander volumetric and energetic performances. Selected working fluid is R236fa. This choice allows to operate at the maximum allowable pressure of the expander at a suitable temperature without the need for high thermal energy to be recovered. In this way, it is possible to operate with superheated vapour at the expander inlet with relative ease. Moreover R236fa is characterized by a pressure greater than the atmospheric one in ambient conditions (figure 4.5c) preventing air infiltration phenomena at the condenser and allowing much easier operations during the charging and discharging phases of the plant. Temperature-entropy diagram and pressure enthalpy diagrams are represented in figure 4.5a and 4.5b.

4.4.1 Volumetric performances

In ideal conditions the mass flowrate elaborated by the expander can be written as:

$$\dot{m}_{wf} = V_{int,end}\, \rho_{int,end}\, N_v\, n \tag{4.4}$$

where $V_{int,end}$ and $\rho_{int,end}$ are the inlet chamber volume and the working fluid density at the intake phase end respectively, N_v the number of vanes and n the rotational speed of the expander. The above equation represents a mass conservation in ideal conditions when all the flowrate provided by the pump is elaborated entirely inside the vanes of the expander. However this is not the case in real conditions. The expander is characterized by geometrical gaps which are needed to reduce friction phenomena between blade sides and stator covers. In addition to that, the blade tips are not in permanent contact with the stator inner surface. In the best case scenario, the oil film ensured by the presence of lubricating oil limits the working fluid passage between a vane and the following one at lower pressure. Even so, vibration phenomena can occur causing blade chattering and the sealing is not permanently guaranteed. The volumetric efficiency is introduced to take into account such effects. It is defined as the ratio between the mass flowrate

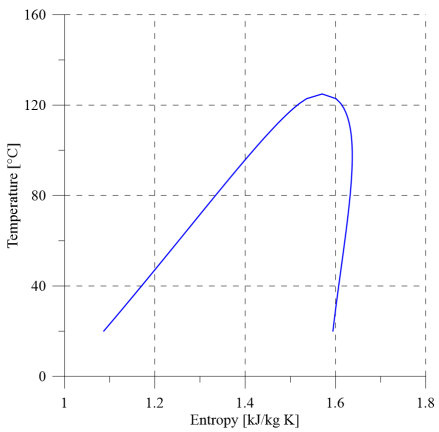

(a) T-s diagram

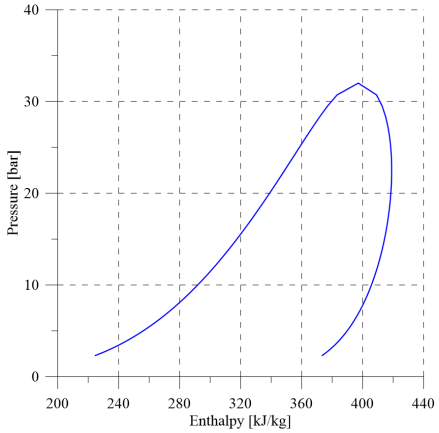

(b) p-h diagram

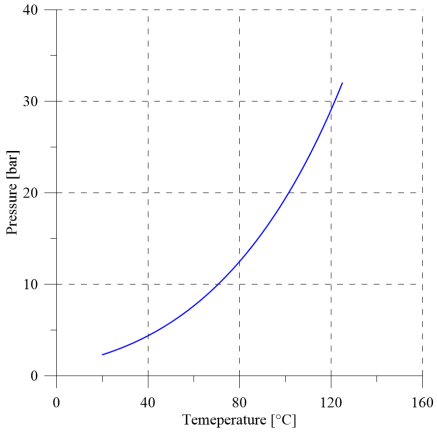

(c) p-T diagram

Figure 4.5: Thermodynamic characteristics of R236fa.

calculated with eq. 4.4 and the measured one. Introducing this parameter, eq. 4.4 can be corrected as follows:

$$\dot{m}_{wf} = \frac{V_{int,end}\,\rho_{in}\,N_v\,n}{\eta_{vol}} \tag{4.5}$$

where η_{vol} represents the volumetric efficiency and ρ_{in} the working fluid density evaluated in this case at the expander inlet. An additional information can be deduced from eq. 4.5. $V_{int,end}$ and N_v are fixed by the geometry of the expander. The rotational speed can be considered constant as well given the characteristics of the experimental layout. In order for the right term to match the left one, the inlet density and the volumetric efficiency

must vary. Volumetric efficiency is primarily a function of gaps between the elements constituting the expander so it can be considered constant as a first approximation. Working fluid density depends on pressure and temperature. In particular, density increases with pressure and decrease at higher temperature. Figure 4.6 show this trend from a thermodynamic point of view. Thermodynamic parameters are evaluated using Refprop. It can be noted how the working fluid density increases linearly with pressure with the superheating degree contributing for less than 10 % with a stronger influence at higher evaporation pressure. This aspect leads to the assumption that the expander inlet pressure, which is strictly connected to the maximum pressure of the plant, is a function of mass flowrate alone as can be noted in figure 4.7.

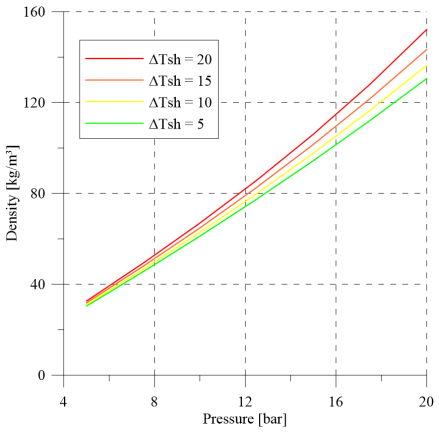

Figure 4.6: Working fluid density vs evaporation pressure at different superheating degrees.

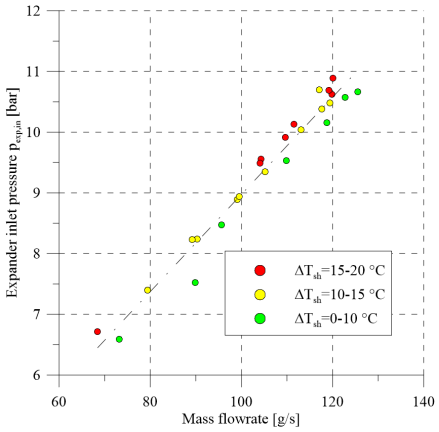

Figure 4.7: Expander inlet pressure vs mass flowrate at different values of superheating degrees.

The representation shows the pressure mass flowrate relationship found experimentally in over 30 points at different values of recovered thermal power. Elaborated mass flowrate varies from 70 g/s to 130 g/s. Corresponding pressure varies linearly from 7 bar to 11.5 bar. The effect of superheating is evidenced using different colours. It can be noted how slight variations from the linear trend are visible, especially in the low mass flowrate range. At higher values, pressures at different superheating degrees tend to diverge slightly. The linear fitting describes sufficiently well the phenomenon with a R square value of 0.96. At approximately 90 g/s, an experimental data in the 0 to 10 °C superheating range shows quite a deviation from the linear fit-

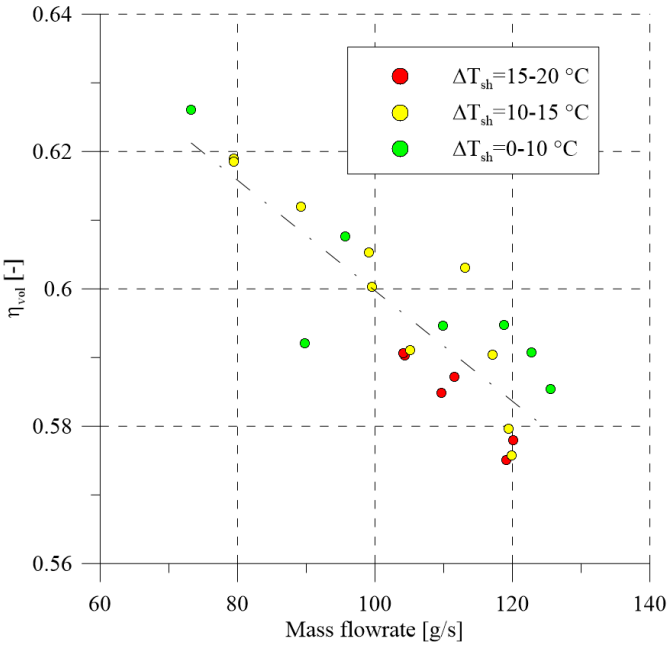

Figure 4.8: Volumetric efficiency vs mass flowrate at different superheating degrees.

ting. It has to be said that this point is characterized by a superheating value lower than 1 °C. Since the accuracy of thermocouples is of the same order of magnitude, and considering that slight variations can be found between real evaporation pressure and the one evaluated using software platforms, the state of the working fluid at the expander inlet in that operating point could have been inside the saturation curves with a quality close to one (fully vaporized fluid). The presence of liquid droplets causes the increase of the working fluid density and consequently the decrease of the expander inlet pressure.

In the considered range, volumetric efficiency varies from 57.5% and 62.5%, with a decreasing trend with the mass flowrate. At higher $\dot{m}_{wf}$, inlet pressure increases while the exhaust pressure is mainly fixed by the condenser performances and the tank upstream the pump. This results in an increased pressure difference which contributes to the increase on the leakages flowrate across the constructive gaps of the expander reducing the volumetric efficiency. A more in depth analysis on this issue will be thoroughly treated in the following chapter. The superheating degree does not influence this parameter. The largest deviation from the linear fitting is ev-

idenced in the same conditions reported above. The liquid content in this case increases the leakage flowrate because of two main reasons:

- The increased density which determine the possibility of a greater mass flowrate to go through the geometrical gaps;
- An increased value of the thermodynamic velocity which does not allow the choking of the mass flowrate;

As a further validation of these considerations the quality of the linear fitting increases from 0.6 to 0.8 if the examined operating point is not considered.

4.5 Indicated and mechanical performances

4.5.1 Indicated cycle analysis

Once the indicated cycle in reconstructed, the indicated power can be evaluated as follows:

$$P_{ind} = n\, N_v \oint_V p\, dV \tag{4.6}$$

where n is the expander speed and N_v the number of the vanes. The implicit assumption is that every vane equally contributes to the total indicated work which is valid in steady state conditions.

Figure 4.9 shows an example of an indicated cycle reconstructed in one of the operating point in the considered dataset. It evidences the main source of losses with respect to an adiabatic isentropic transformation. First source of loss is the pressure drop ΔP_{int} related to the fluid admission through the inlet port. The intake phase should be isobaric, however near the end, in proximity of the intake end volume, there is a pressure decrease which is mainly due to the throttling losses. At the end of the intake, the blade reduces the opening of the vane causing a pressure drop of the fluid entering the chamber. An additional source of loss is the overexpansion of the working fluid. In this case it can be noted that in the end of the expansion process, the pressure inside the chamber gets lower than the one externally exerted by the plant. This causes a negative work which is detracted from the theoretical obtainable one.

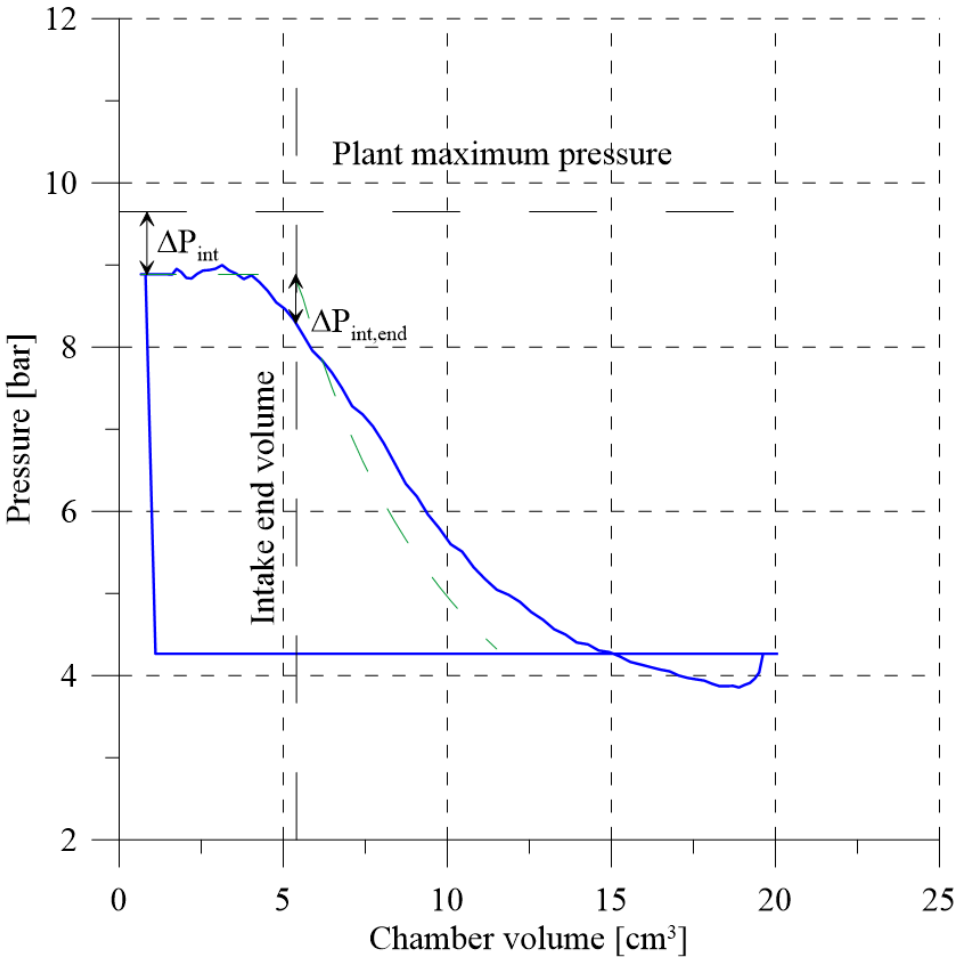

Figure 4.9: Example of indicated cycle with pressure losses details.

In figure it is possible to observe also the variations with respect to an adiabatic isentropic transformation. In the specific case, the pressure-volume profile is evaluated considering the ideal mass inside the chamber calculated as:

$$m_{id} = \rho(T_{exp,in}, p_{int,in})\, V_{int,end} \tag{4.7}$$

where $T_{exp,in}$ is the expander inlet temperature, $p_{int,in}$ the pressure at the intake start considering an isobaric process until the intake end and $V_{int,end}$ the expander intake volume. It is worth noting that the isentropic expansion phase is much shorter compared to the real case. This happens because the ideal mass is much lower that the real mass flowrate entering through the

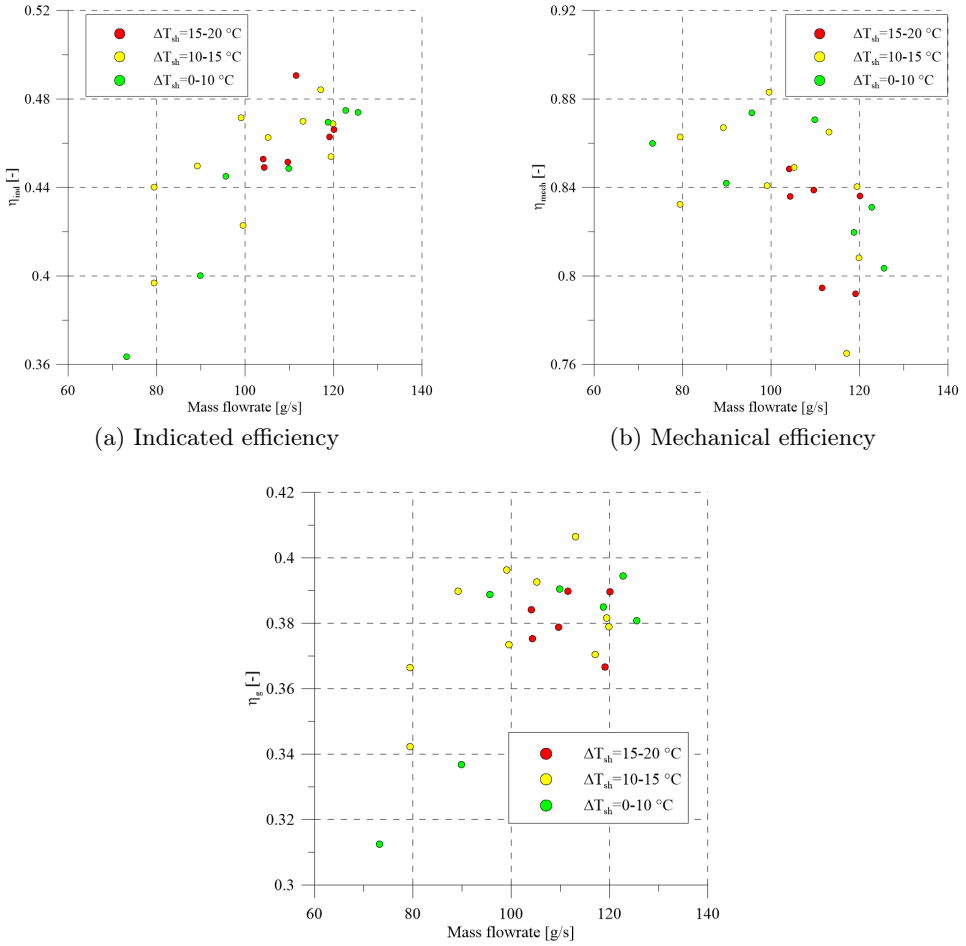

(a) Indicated efficiency

(b) Mechanical efficiency

(c) Overall efficiency

Figure 4.10: mechanical and global efficiency of the single intake expander: experimental results

inlet port. The difference in fact is not elaborated by the expander and leaks through the geometrical gaps between rotor side and stator cover. If all the mass flowrate provided by the pump was elaborated inside the chamber volumes, a much higher inlet pressure would be observed. This clarifies also why the area is comparable in the two cases. However in the real one a much greater mass flowrate is needed.

4.5.2 Indicated and mechanical power

Once evaluated the indicated power, indicated and mechanical efficiency can be calculated as follows:

$$\eta_{ind} = \frac{P_{ind}}{P_{ad,is}} \tag{4.8}$$

$$\eta_{mech} = \frac{P_{mech}}{P_{ind}} \tag{4.9}$$

where the mechanical power P_{mech} is evaluated through torque and rotational speed measurements and the adiabatic isentropic efficiency can be evaluated considering the expander inlet and outlet pressure and the expander inlet temperature in the following way:

$$P_{ad,is} = \dot{m}_{wf} \left(h(p_{exp,in}, T_{exp,in}) - h(p_{exp,out}, s_{exp,in}) \right) \tag{4.10}$$

h represents the specific enthalpy of the working fluid, while $s_{exp,in}$ is the specific entropy evaluated at the expander inlet. The overall efficiency can be calculated considering the mechanical to isentropic power ratio or, in equivalent manner, through the product of the two aforementioned efficiencies.

The results in terms of efficiencies are reported in figure 4.10. Mass flowrate has been varied between 70 g/s and 130 g/s. With respect to previous data a greater dispersion can be seen. This is due to some intrinsic uncertainties in the evaluation of the indicated cycle. The discharge phase is represented with an isobaric transformation. In a real case, dynamic phenomena can appear and pressure oscillations can be seen during the emptying of the vane. This aspect will be further discussed after the CFD 1D model will be presented in the next chapter.

Despite the dispersion, some conclusions can be deduced from the reported trends. Superheating degree does not show primary relevance in terms of mechanical and indicated efficiency. Both of them show a relative maximum in correspondence of a certain mass flowrate. In the first case, a maximum 49 % efficiency is achieved at 110 g/s. The performances show a constant increase up to this point, slightly decreasing in the upper range. The causes of this behaviour have to be found in a better filling of the vane approaching the design mass flowrate of the expander. When this latter in-

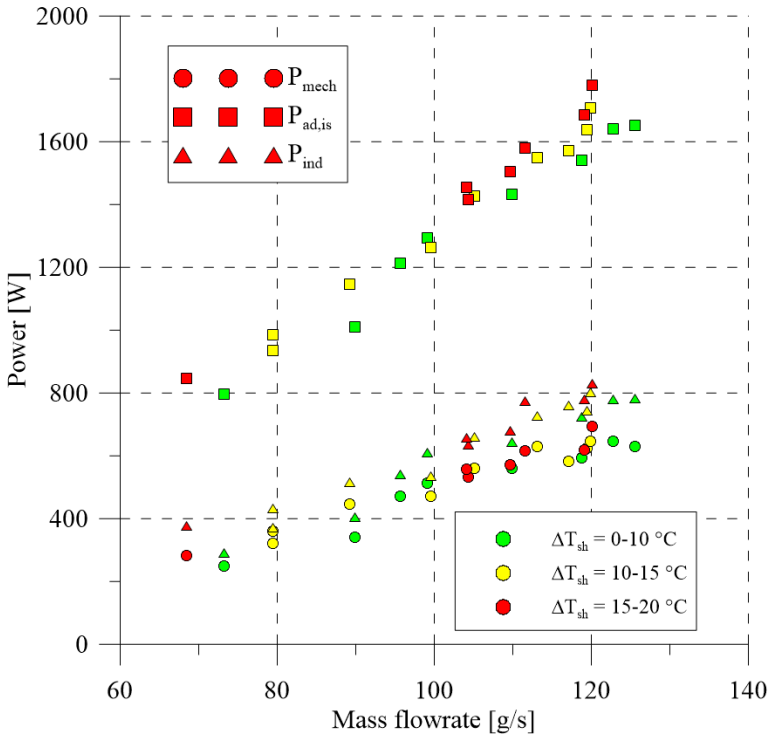

Figure 4.11: Indicated, mechanical and isentropic power of the single intake expander.

crease above its limit, leakages play their role and contributes to the decrease of the performances.

Regarding the mechanical efficiency values between 76% and 88% can be seen in figure 4.10b. In this case, quite constant mechanical performances are obtained up to 115 g/s. After reaching the optimum value, mechanical losses starts increasing because of the increased pressure inside the vane. The higher the pressure inside the chamber, the higher the force acting on the bottom on the blade due to the presence of fluid in the cavities in the rotor for the housing of the blades. This phenomenon increase the normal force acting between the vane tip and the stator inner surface increasing the friction force and consequently the mechanical losses.

The resulting overall efficiency (figure 4.10c) follows the same behaviour, being the result of their product. Maximum efficiency reaches 41% at 117 g/s. Observing the values of superheating degree, higher superheating does not determine higher efficiency. The trends observed from 10 °C to 15 °C show the highest overall performances.

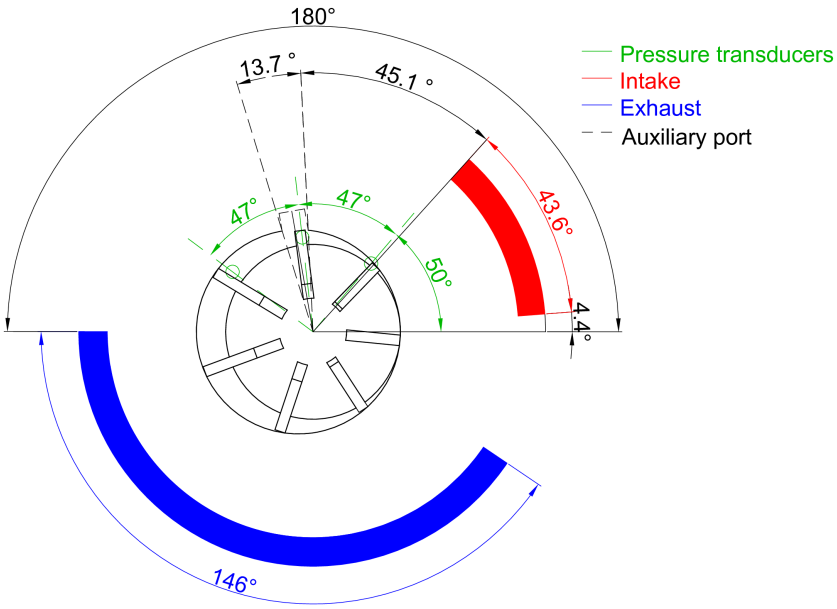

Figure 4.12: Dual intake configuration.

Power outputs are represented in figure 4.11. Isentropic power linearly increases with flowrate. Main sources of losses are in the conversion to indicated power with over 50% decrease due to volumetric losses. Friction determines a 20 % power reduction on average in the experimented range. Highest mechanical power output is 693 W which is achieved at 120 g/s for a superheating degree of 20 °C and an overall efficiency of 39%. On the other hand, the highest efficiency (40 %))is obtained for a slightly lower flowrate (113 g/s) with 643 W power output.

4.6 Dual Intake results

4.6.1 Premise

After the experimental campaign conducted with the OEM machine, an auxiliary port has been introduced on the stator. The additional inlet port geometric characteristics can be seen in figure 4.12.

In relation to the reference angle used, the port is located at 45.1 ° from the intake end. It has an angular extension of 13.7 °. In this way, the

secondary fluid admission starts right after the end of the main one. Its position and geometrical features have been designed following the results of the study reported in [162]. An optimization algorithm has been used in order to find the best position for the maximization of the power output.

After the first experimental campaign, whose data have been reported in the previous section, a decrease of the expander performances has been experienced. Since the adoption of the dual port is subsequent with respect to this deterioration, the expander performances with the dual port will be compared to the results of a second experimental campaign conducted on the single intake expander just before its modification. These lower performances, which have affected the mechanical and volumetric efficiencies, have been attributed to the wear of the blades in direct contact with the stator inner surface. This assumption has been further confirmed after the inspection done on the machine before its modification.

4.6.2 Volumetric performances

The most important impact of the dual intake port is the modification of the mass flowrate - expander inlet pressure relationship. It is possible to define a parameter called permeability as:

$$\alpha = \frac{\dot{m}_{wf}}{p_{exp,in}} \tag{4.11}$$

In this sense, a much higher permeability is obtained with this technology. In other words this means when the mass flowrate increases, a much lower inlet pressure is obtained which can be a beneficial aspect in specific applications where upper limits cannot be exceeded.

Figure 4.13 shows the modification of the pressure mass flowrate diagram in this case. The reported trend can be compared to the one observed in the two experimental campaigns conducted on the single intake expander (SIP). Moving from the first to the second series, it can be noted a decrease of the slope of the linear fittings. This trend is justified by the lower volumetric efficiency achieved which was lower in the second campaign due to the aforementioned wear phenomena. In fact, considering that:

$$\dot{m}_{wf} = \frac{\rho_{int,end}\, n\, N_v\, V_{int,end}}{\eta_{vol}} \tag{4.12}$$

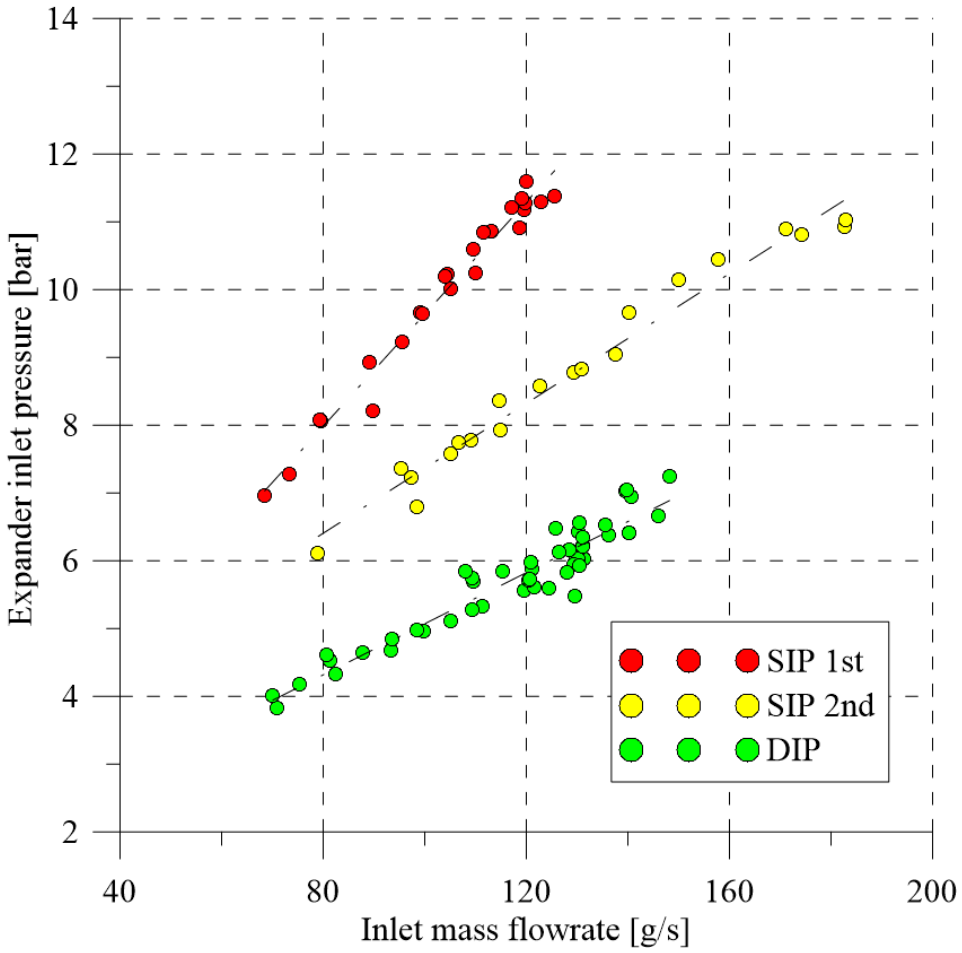

Figure 4.13: Pressure mass flowrate relationship comparison in the tested cases.

Being the rotational speed, the number of the vanes and the intake volume the same in both cases, for a fixed mass flowrate provided by the pump a lower working fluid density is needed if the volumetric efficiency is lower. Being the density proportional to the pressure of the fluid, this issue leads to a decrease of the expander inlet pressure which justifies the behaviour represented in 4.13. In this sense the drop of the slope is detrimental and it is only due to the poorer volumetric performances of the device.

On the other hand, the reported trend of the dual intake port (DIP) expander has a different meaning. Making reference to the same equation, the dual intake option determines a higher intake volume which contributes to the decrease of the inlet density and consequently of the maximum pressure.

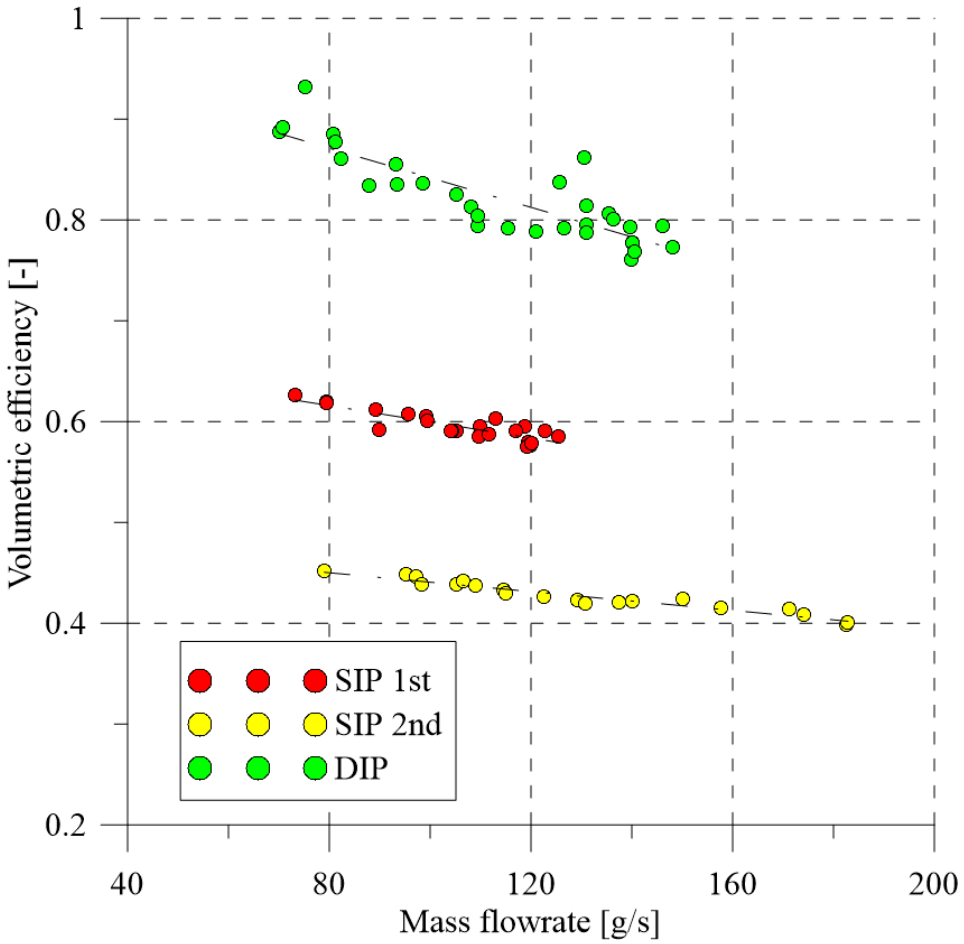

Figure 4.14: Volumetric efficiency results of the single intake expander and dual intake expander.

Moving from the first to the second campaign, no qualitative differences exist in the indicated cycle profile. On the contrary, the dual intake determines strong modifications on the cycle which will be discussed in the following section.

As a further evidence of the considerations done above, the volumetric efficiency in the three different cases have been reported in figure 4.14. It can ben noted the efficiency drop from 60 % to 48%. On the other hand, the DIP efficiency is much higher showing values between 80% and 90% with the same decrease at higher flowrates. In this last case being the intake volume different, the volumetric efficiency value has been evaluated as follows:

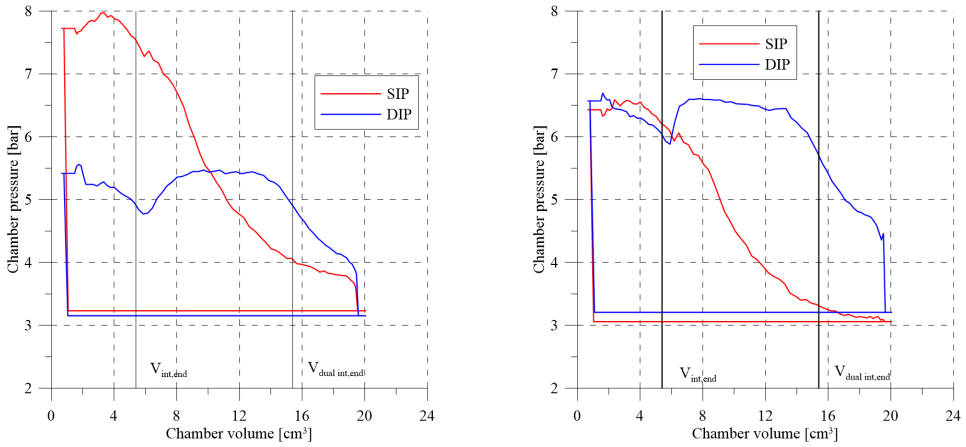

Figure 4.15: Indicated cycle comparison between SIP and DIP expander at fixed mass flowrate a) and fixed inlet pressure b)

$$\eta_{vol} = \frac{\left(\rho_1 \, V_{int,end} + \rho_2 \left(V_{dualint,end} - V_{int,end}\right)\right) N_v \, n}{\dot{m}_{wf}} \tag{4.13}$$

where $V_{int,end}$ is the volume at the main intake end and $V_{dualint,end}$ represents the volume at the end of the auxiliary intake. ρ_1 and ρ_2 are defined as:

$$\begin{aligned} \rho_1 &= \rho(p_{exp_{in_1}}, T_{exp,in}) \\ \rho_2 &= \rho(p_{exp_{in_2}}, T_{exp,in}) \end{aligned} \tag{4.14}$$

while n and N_v are the expander speed and the number of vanes. $p_{exp_{in_1}}$ and $p_{exp_{in_2}}$ are the pressures measured at the two intake adduction pipes. The same temperature has been considered in the two cases being the intake process almost isothermal. This representation of the volumetric efficiency is justified by the fact that the auxiliary intake starts right after the main one. As soon as the vane does not face the main port, the communication with the auxiliary one is opened and the working fluid can fill the same vane through the auxiliary pipe.

4.6.3 Indicated cycle comparison

To understand the deep modifications on the indicated cycle realized through the auxiliary intake port, two different comparisons are reported in figure 4.15 (a) and (b).

In the first case, the same mass flowrate is provided by the pump. The admission pressure at the expander inlet is much lower in the DIP case because of the higher permeability of the machine. This determine a lower filling of the vane and consequently poorer performances. The greater pressure observed during the expansion phase cannot balance the lower admission pressure. The result is that the indicated power is lower in the DIP case with 750 W against the 804 W achieved with the SIP device which is a 7.3 % reduction. In has to be noted that exhaust pressure is slightly lower in the reported DIP case. This difference contributes to lower the gap between indicated power which would be higher with the same exhaust pressure.

Figure 4.15b demonstrates the potential advantage of such a system. The figure shows a comparison of the indicated cycle at fixed intake pressure. In order for the DIP device to reach the same pressure, the provided mass flowrate must be significantly higher. In the reported case mass flowrate is increased from 97 g/s to 148 g/s which represents a 52 % growth. It is worth considering that if this increase was due to poorer volumetric performances most part of the working fluid would have bypassed the vane flowing through the leakage gaps and no actual modifications of the indicated diagram would have appeared. The increase of internal leakages between vanes would have sustained the pressure during the expansion, achieving higher values with respect to an adiabatic isentropic transformation resulting in a partial power recovery. Aside from this phenomenon, no differences would have occurred. Obviously, that is not the case when using a dual intake port. The increased mass flowrate is the main responsible for the constant pressure profile after the main intake port closing. Pressure rises right after the end on the main suction process until reaching a chamber volume equal to 15.4 cm^3. The same trend observed for the SIP case, related to the throttling of the fluid entering inside the vane when the port is closing, can be seen also in this case. The indicated power grows from 544 W to 934 W, realizing a 72 % increase with a 52% more mass flowrate without the need for higher pressure.

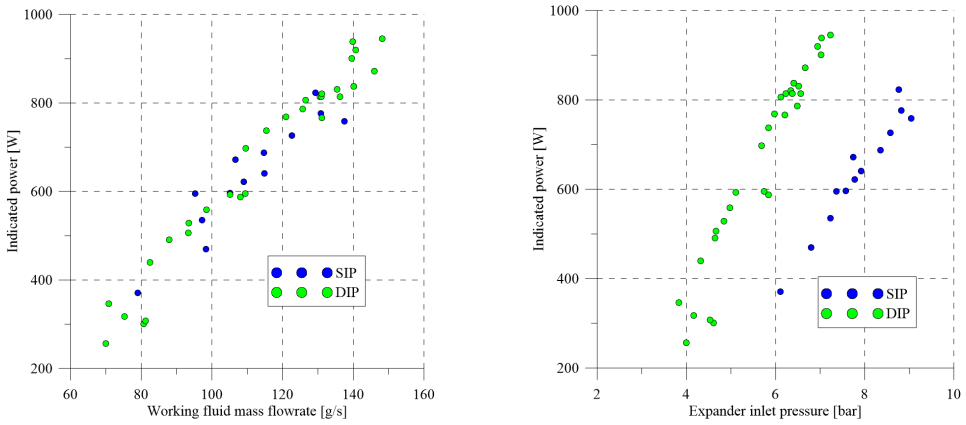

Figure 4.16: SIP and DIP comparison: indicated power vs flowrate(a) and expander inlet pressure (b).

4.6.4 Indicated and mechanical power results

Experiment results are reported in this section. Indicated and mechanical performances will be regarded with special attention given the importance of them for the mechanical power recovery.

Figure 4.16 shows a comparison between the indicated power produced by the OEM device and the dual intake expander. Figure 4.16a compares the indicated power at different mass flowrates provided by the pump. Experimental tests have been conducted in similar conditions so as to guarantee an equal exhaust pressure at the expander exit. Results demonstrate that a comparable indicated power can be achieved for a fixed mass flowrate. The proportionality is linear with the indicated power varying from 250 W to 980 W moving from 70 g/s to 150 g/s.

Figure 4.16b further highlights the benefits of such a system. The indicated power is represented against the expander inlet pressure. Through this representation the advantage are clearer. The indicated power produced in the DIP case is always above the SIP one. This means that for a fixed pressure the power output of the DIP expander is greater than the OEM option. For an expander inlet pressure equal to 6 bar, 370 W are achieved with the SIP. On the other hand, at the same inlet pressure, 770 W are reached by the expander with the dual intake port system which represents a 125 % increase. Using the linear fitting of the two described trends, in the over-

lapping region of inlet pressure, the expander power output increase varies between 350 W and 420 W due to the higher slop of the DIP case. This offset increases up to 520 W extrapolating data at 8.8 bar, the maximum pressure achieved with the OEM expander.

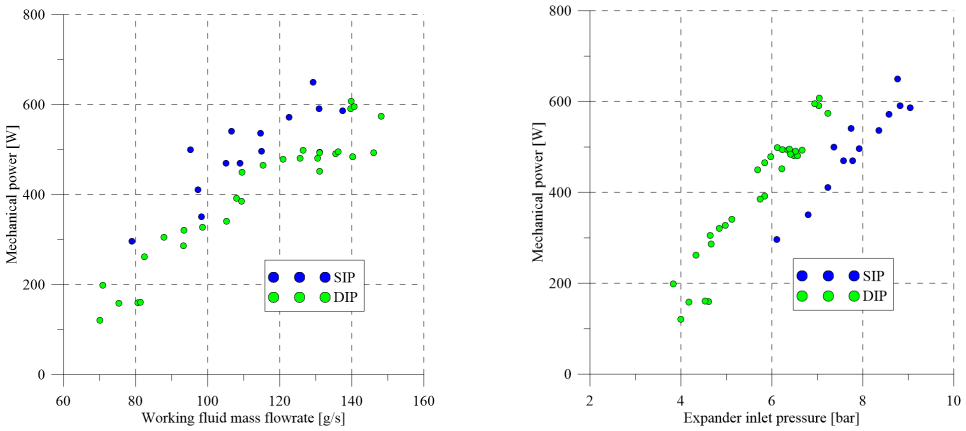

Figure 4.17: SIP and DIP comparison: mechanical power vs flowrate(a) and expander inlet pressure (b).

Similar considerations can be applied analysing the mechanical performance. In this case the offset previously found is reduced because of the lower mechanical efficiency showed by the DIP option (Figure 4.18) As observed above, since there is not physical relation between the reduction of mechanical performances and the adoption of an auxiliary port, this behaviour has been attributed to wear phenomena occurred between the different experimental campaigns due to the operating hours of the device. The only pure thermodynamic parameter which can influence the friction losses is the chamber pressure. At higher pressure the buoyancy determines an higher force acting on the bottom of the blade which increase the friction between the blade tip and the stator. This is not the case of the DIP since its main advantage is the reduction of the chamber pressure.

The lower mechanical performances also influence the expander overall efficiency evaluated with respect to the an adiabatic isentropic transformation. Experimental data are represented in figure 4.18a and b. The higher indicated efficiency shown for the DIP case is due to the increased volumetric performances which determines lower leakages through the expander and

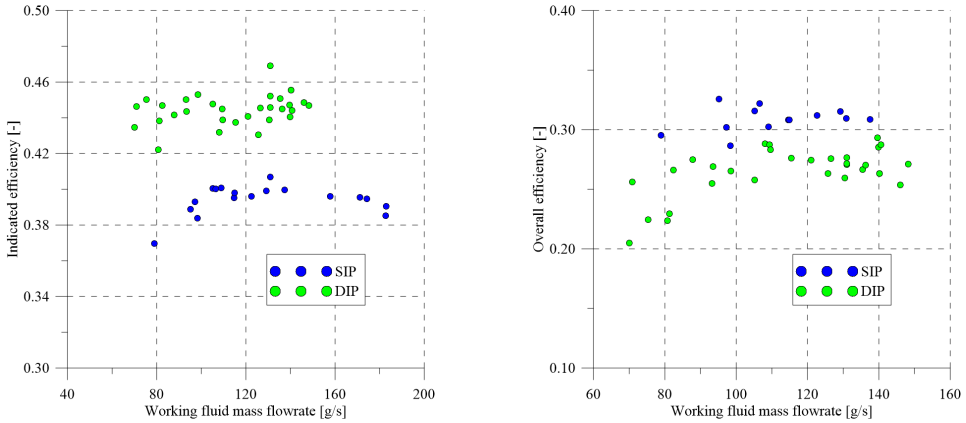

(a) (b)

Figure 4.18: SIP and DIP comparison: indicated (a) and mechanical (b) effiency vs flowrate.

between a vane and the following one. Main reason is that the lower pressure reduces the driving force that determines the leakage flow.

Indicated efficiency ranges between 42 % and 46 % for the DIP case, showing a constant trend with flowrate. On the other hand, maximum efficiency achieved in the SIP case is 41.5% at 125 g/s. At higher mass flowrates, the increased pressure reduces the internal efficiency because of higher flow losses. When the mass flowrate is lower, overexpansion losses can occur. In the DIP case an isochoric expansion phase happens in all the experimented operating points which avoid this kind of phenomena. The resulting overall efficiency is strongly affected by the reduction of mechanical performances. Maximum values reach 31 % for the SIP case at 125 g/s and 30 % in the DIP one.

4.7 Final considerations

The reported experimental data showed the performances of rotary vane expander integrated in an ORC-based unit thought for a WHR-ICE application. A comparison between two technologies involving different intake systems has been conducted. Experimental results showed advantages and downsides of both options. In particular, the dual intake port allows the reduction of the hydraulic resistance of the expander, making possible the decrease of the inlet pressure at higher flowrates. The analysis on the indi-

cated cycle showed that a slightly lower power can be produced with respect to the single intake device at fixed flowrate. On the other hand, for a fixed pressure the DIP expander is able to produce a greater power at the expense of an increase flowrate. This allows to increase the overall flexibility of the ORC plant, especially in applications where the thermal hot source varies strongly compared to the design operating point. In fact, this would cause an increase in the working fluid flow rate to allow a greater recovery.

Overall efficiencies are in the order of 30% for both options which are in line with other technologies experimented in literature. The main cause of these values is related to the volumetric performances of the machine which greatly affects the overall efficiencies. For these reasons in the chapter which follows, a model based analysis on flow losses and the fluid dynamic phenomena behind them will be exposed with the aim to understand the design choices to make to increase the rotary vane expander overall performances.

Chapter 5

Numerical analysis on the effects of leakages in Sliding Vane Rotary Expanders

5.1 Introduction

The experimental results reported in the previous chapter have been used to calibrate a numerical model built in GT-suite®. GT-Suite is a software platform which uses a 1D finite volume discretization method (Figure 5.1) to solve a system of differential equations representing the continuity equation, the energy conservation equation and the Navier Stokes equations. This means that the fluid dynamic quantities are considered constant along the cross-sectional area of the elemental duct. Vector quantities like velocity are evaluated at the interface between each control volume. On the other hand, scalar quantities are considered uniform inside the same volume. Mass and momentum conservation are written as follows:

$$\frac{dm}{dt} = \sum \dot{m} \tag{5.1}$$

$$\frac{d\dot{m}}{dt} = \frac{dpA + \sum_{boundaries}(\dot{m}u) - 4C_f \frac{\rho u|u| A dx}{2D} - K_p \frac{\rho u|u|}{2} A}{dx} \tag{5.2}$$

while the model use a different form for the energy conservation equation

Symbol	meaning
A	cross-sectional flow area
As	heat transfer surface area
C_f	Fanning friction factor
D	equivalent diameter
dp	pressure differential acting across dx
dx	length of mass element in the flow direction (discretization length)
e	total specific internal energy (internal energy plus kinetic energy per unit mass)
H	total specific enthalpy H = e + p/ρ
h	heat transfer coefficient
K_p	pressure loss coefficient (commonly due to bend, taper or restriction)
$\dot{m}$	boundary mass flux into volume,
m	mass of the volume
p	pressure
ρ	density
T_{fluid}	fluid temperature
T_{wall}	wall temperature
u	velocity at the boundary
V	volume

Table 5.1: Nomenclature used in the governing equations of the numerical model.

depending if an explicit or an implicit solver is used. In the first case the internal energy is considered as follows:

$$\frac{d(e)}{dt} = -p\frac{dV}{dt} + \sum_{boundaries} (\dot{m}H) - hA_s(T_{fluid} - T_{wall}) \tag{5.3}$$

while for the explicit case the following equation is considered:

$$\frac{d(\rho HV)}{dt} = V\frac{dp}{dT} + \sum_{boundaries} (\dot{m}H) - hA_s(T_{fluid} - T_{wall}) \tag{5.4}$$

with the meaning of each parameter reported in table 5.1.

The explicit or implicit solver influences the method in which parameters are integrated over time. In the explicit solver, primary solution variables are represented by mass flowrate, density and internal energy. Values on the right end side of the equations are evaluated based on the previous known time step in the considered sub-volume and its surroundings. This approach is well suited for highly unsteady flow where the knowledge and the accuracy in the representation of pressure pulsations is of primary importance. The time step is automatically evaluated by the model in order to satisfy the Courant condition :

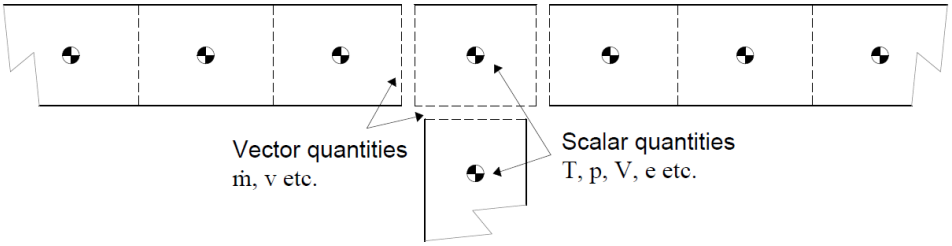

Figure 5.1: GT-suite finite volume discretization scheme.

$$\frac{\Delta t}{\Delta x}(|u| + c) \leq 0.8 * m \tag{5.5}$$

where ΔT and Δx represents the space and time intervals while u and c the fluid and thermodynamic speed respectively. The parameter m is a multiplier which must be less or equal to 1.

In the implicit solver instead, primary solution variables are mass flowrate, pressure and total enthalpy. The main difference is that the method finds the solution in all the subvolumes of the systems in the new time step solving a system of algebraic equations. Main advantage of this method is that it reduces the computational effort lowering the time needed for the simulation to find the solution. However, this method is not suitable when pressure waves are significant. Moreover, the convergence of the solution has to be verified at each time-step.

5.2 Numerical model

An overview of the numerical model is presented in figure 5.2. Each object represents a physical subcomponent of the expander or fulfils a certain function. Most important elements are numbered from 1 to 11 in order to facilitate the description of the model.

Elements 1 and 2 represents the boundary conditions of the expander. In 1 the working fluid is specified and inlet pressure and temperature are set. Element 2 is the outlet boundary condition which sets the outlet pressure acting like a plenum with infinite capacity. After the first boundary condition, several elements representing physical ducts exist with a junction for the auxiliary intake. This ramification is obviously absent in the case of the

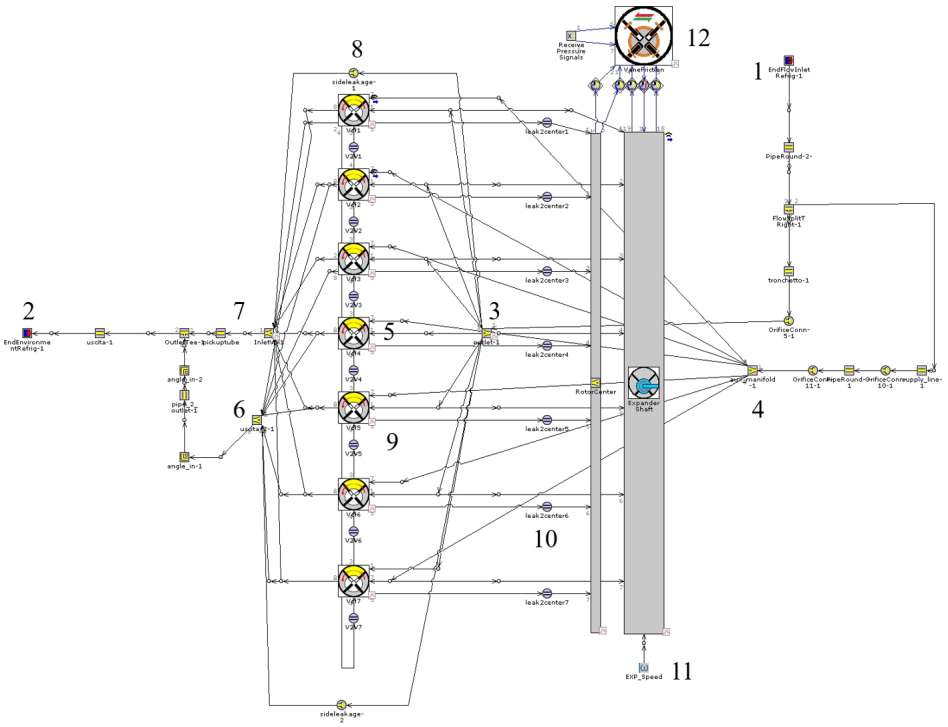

Figure 5.2: GT-Suite numerical model of the dual intake port expander.

single intake expander. Flow lines goes towards elements 3 and 4 which are the intake manifolds of the first and second intake. From there, the fluid is split between the different vanes (element 5). According to the angular position of the rotor, only some of the vanes are active with the working fluid filling them. The outlet of each vane is collected in two outlet manifolds whose pressure is linked to the one fixed at boundary condition 2.

Leakages are modelled by mean of elements 8, 9 and 10 which represent the side leakage, the vane to vane leakage and vane to rotor center leakage through the blades bottom. 12 is a component which has the function to evaluate viscous and dry friction losses, known the pressure inside the vane and the geometrical features of the expander. "11" defines the expander angular speed.

5.2.1 Indicated power calibration

The indicated power strongly varies depending on the chamber pressure trend during the revolution of the expander. Pressure inside the vane is

a function of the mass trapped inside it which depends on the elaborated flowrate and the leakages flow through the paths described in elements 8, 9 and 10. In this sense, the indicated power calibration strongly depends on the accuracy of the modelling of leakage flows. As seen, three main types of leakages exist. Leakages at the blade tip which determines a flowrate between adjacent vanes, leakage through rotor slots and side leakages between the rotor and the end wall plates. In this latter case, the mass flow is not elaborated in the vanes and goes directly from the intake to the exhaust.

First two kind of leakages are modelled in the same way with the Poiseuille-Couette flow correlation:

$$Q = A_{blade}\left(\frac{\delta^2 \Delta P}{12\mu L} - \frac{1}{2}U_{wall}\right) \tag{5.6}$$

where Q is the volumetric leakage flowrate, δ is the clearance gap between blade tip and stator inner surface, μ the dynamic viscosity and U_{wall} the peripheral speed evaluated at tip blade. A_{blade} is the passage area which is a function of the clearance gap δ and the axial length of the blades. The calibration procedure involves the definition of the clearance gap δ as will be further discussed in the following sections.

Side leakages are modelled instead through the discharge coefficient evaluated below as:

$$C_d = \frac{\dot{m}}{\rho A\sqrt{\frac{2(p_{in,tot} - p_{out,stat})}{\rho}}} \tag{5.7}$$

where A is the passage area, ρ the working fluid density, $p_{in,tot}$ the total pressure at the inlet and $p_{out,stat}$ the static pressure at the expander outlet. Iterations are needed in order to find the leakage flowrate $\dot{m}$ which solves the system of equations.

5.2.2 Mechanical power calibration

Making reference to figure 5.2 the mechanical power calibration is managed through element "12". In this section all the viscous and dry friction losses are evaluated. The most important one is the dry friction between blade tip and stator surface. The normal force acting on the bottom of the blade has two contributions, the centrifugal force and the hydrostatic force

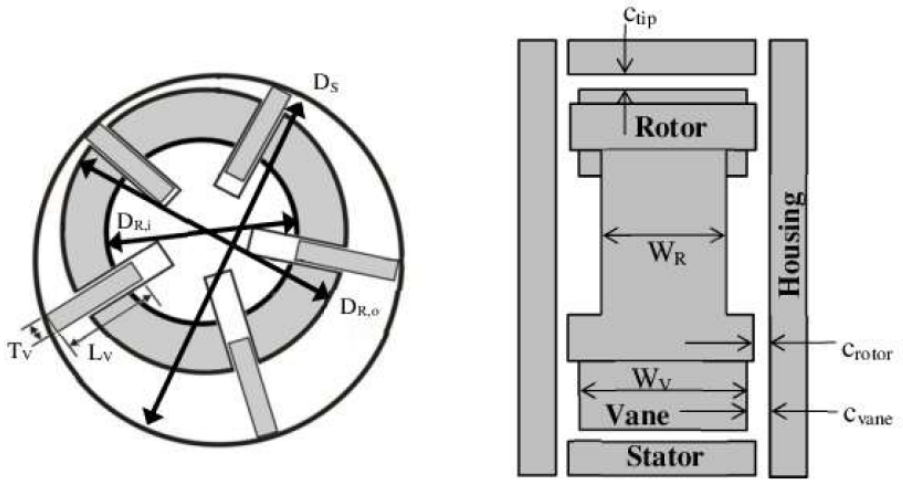

Figure 5.3: Sliding vane expander scheme and geometrical parameters.

due to the presence of fluid in the interstice under the blade. Centrifugal and hydrostatic forces can be expressed as:

$$F_c = M_b \omega^2 (R_b(\theta) - L_b/2) \tag{5.8}$$

$$F_p = p_{rot} W_b T_b \tag{5.9}$$

where M_b is the blade mass, ω the expander rotational speed and R_b the position of the tip blade with respect to the rotor center. L_b, W_b and T_b are the geometrical features of the blade with reference to figure 5.3. The resulting friction power associated with both of these forces is expressed as:

$$P_{a_1} = N_v C_{f,tip} (F_p + F_c) R_b \omega \tag{5.10}$$

The second contribution is given by the viscous friction between the blade tip and the stator inner surface due to the lubricating oil adhering on it. The viscous force can be written as:

$$F_{f,v} = \mu A \frac{du}{dy} \tag{5.11}$$

where μ is the dynamic viscosity of the working fluid, A the contact

surface and du/dy the velocity gradient. The friction power associated is given by the product of the force and the peripheral speed.

$$P_{a_2} = F_{f,v}\omega R_b = \frac{N_v \mu W_b T_b R_b^2 \omega^2}{c_{tip}} \tag{5.12}$$

where c_{tip} is the gap between the blade end and the stator.

Viscous friction phenomena occur also between the rotor and the end wall plates of the expander housing. These are modelled considering a rotor mean diameter R_{rot}, the contact area A_{rot} and the geometrical gaps between the two surfaces as follows:

$$P_{a_3} = F_{f,v}\omega R_{rot} = 2\mu A_{rot}\frac{\omega^2 R_{rot}^2}{c_{rot}} \tag{5.13}$$

Finally the same friction phenomena happens also between blade sides and the housing. In this case the contact surface can be evaluated considering the thickness and length of the blade.

$$P_{a_4} = F_{f,v}(R_b - L_b/2)\omega = 2N_v \mu L_b T_b \frac{\omega^2 (R_v - L_v/2)^2}{c_{vane}} \tag{5.14}$$

Friction power can be evaluated as the sum of all the aforementioned components. Other kinds of friction, viscous and dry, occur between the vane and the rotor slots. However, the extent of these latter is negligible with respect to the previous one. Moreover, the friction force is directed radially and does not contribute to the friction torque. Its knowledge could help in the dynamic simulation of the blade linear motion inside its slot. However, since this is not the aim of the analysis, these components will not be considered.

5.2.3 Numerical validation

The considered dataset for the numerical validation of the expander model is reported in table 5.2. Data have been selected among the different tests reported in the previous chapter to guarantee a wide range of operating conditions. Mechanical power varies between 470 W and 935 W for values of recovered thermal power ranging from 16.4 kW to 37.4 kW. Different values correspond to different flowrates. The higher the flowrate, the higher the thermal power exchanged at the evaporator. The dataset also allows to analyse volumetric losses at different values of efficiency. Global

case	$p_{exp,in}$ ±0,03 [bar]	$p_{exp,out}$ ±0,03 [bar]	n ±1 [RPM]	T_{in} ±0,3 [°C]	T_{out} ±0,3 [°C]	P_{mech} ±0,8% [W]	P_{ind} ±2% [W]	P_{rec} ±0,5% [kW]	$\dot{m}_{WF}$ ±0,15% [kg/s]	η_{vol} ±2,3% [-]	η_{exp} ±1% [-]
1	11,8	4,4	1550	82,1	62,5	935	1105	37,4	200	0,33	0,31
2	11,1	4,3	1547	78,1	60,7	859	1069	34,1	184	0,33	0,32
3	10,5	3,7	1547	76,2	57,8	864	1022	30,5	166	0,33	0,32
4	9,5	3,2	1541	83,4	62,9	795	866	27,1	138	0,33	0,32
5	11,6	4,8	1537	96,5	78,6	693	834	22	120	0,43	0,39
6	10,8	4,6	1533	90,8	72,1	616	744	20,2	112	0,45	0,39
7	10,2	4,5	1529	78,7	61,9	559	689	18,7	110	0,45	0,40
8	9,2	4,1	1525	74,6	54,1	471	571	16,4	96	0,50	0,39

Table 5.2: Experimental dataset for the single intake expander numerical validation.

efficiencies range between 30 % and 40%. Highest overall performances are reached when the volumetric efficiency is higher. The maximum value of η_{exp} is 40% when η_{vol} is 50% at a mass flowrate equal to 96 g/s. The data reported in table once again confirm the detrimental effect of volumetric losses which represent the primary limiting factor of sliding vane rotary expander.

The significance of volumetric losses can be outlined comparing case 5 and case 1. The two operating points are characterized approximately by the same expander inlet pressure (11.8 bar vs 11.6 bar). However, due to different filling factors, mass flowrate is greater in case 1. This issue determines not only a lower expander efficiency (31 % against 39 %) but also a higher need for thermal power to be exchanged at the evaporator to ensure a superheated vapour condition at the evaporator outlet which could not be guaranteed by the heat exchanger itself. Indeed, to reach the same expander inlet pressure, the mass flowrates must increase when the volumetric losses are higher.

As noted before, the validation parameters are the mass flowrate, the indicated power and the mechanical one. A calibration procedure is needed in order to achieve suitable accuracy in the numerical results with moderate errors compared to experimental data. In this case, as previously observed, clearances play a major role in volumetric losses. The existence of geometrical gaps between components of the expander determine a leakage flowrate which reduce the working fluid mass elaborated inside the chamber volume reducing the volumetric performances. At the same time, the extent of this gaps are hardly measurable. For this reason they have been used as calibration parameters.

A representation of the different leakages in a sliding vane rotary expander is reported in figure 5.4. Three main leakage paths can be found.

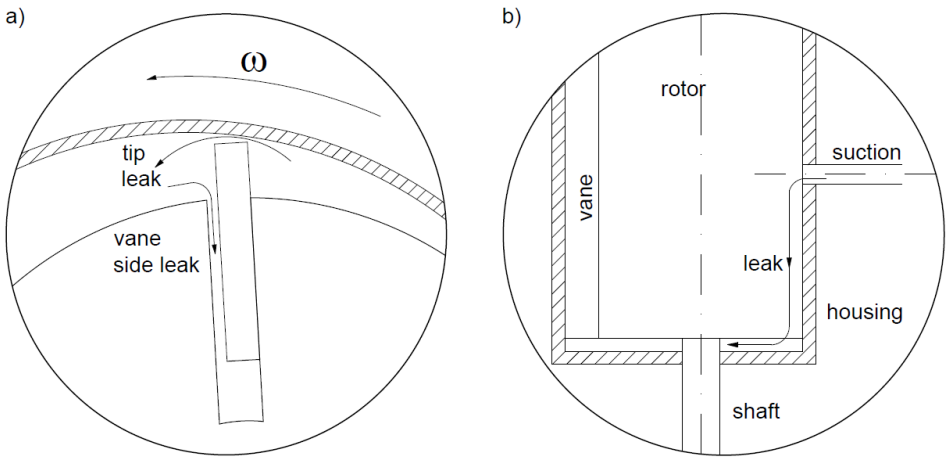

Figure 5.4: Leakage paths in sliding vane rotary expander: tip and vane side (a) rotor slots (b)

The one at the tip blade which determines the passage of a certain flowrate between vanes, the one at the vane side which has a similar consequence and the leakage in the gap between rotor and stator covers (figure 5.4b). In this latter case the working fluid mass is not elaborated by the vanes at all and passes from the intake to the exhaust directly. A further aspect to be outlined is the substantial difference between leakages at tip blades and the other ones. In the first case, no actual clearance exists in nominal conditions. The contact between the blade and the stator surface is guaranteed by the centrifugal force acting on the bottom. Moreover, lubricating oil should deposit on the surface fulfilling two main tasks: the reduction of friction losses and the sealing of the chamber. However, during real operations, vibrations can occur in the blades determining chattering phenomena which detach the tip blade from the stator thus allowing the passage of the fluid. In this sense, the assumption of a gap represents a mathematical construction to consider such flow losses. In the other cases instead, a geometrical clearance is needed in order to ensure the correct functionality of the expander.

Clearances have been varied during calibration to minimize the difference between experimental and numerical results of mass flowrate and indicated power. Mechanical power has been considered as well since the variations of gaps influence also the friction losses. The results of the numerical procedure and the values assigned to clearances are reported in table 5.3 and table 5.4. Two set of values are reported for two different volumetric efficiencies.

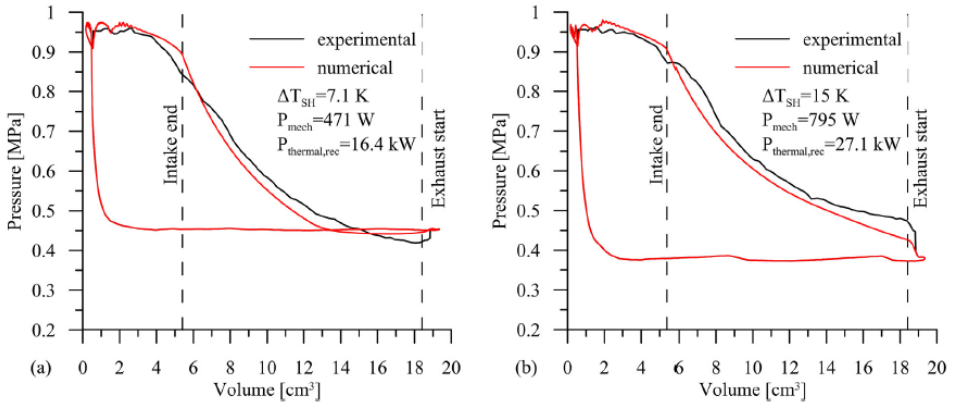

Figure 5.5: Comparison between numerical and experimental indicated cycle, case 7 (a) and case 4 (b)

The dataset in fact includes data acquired in two different experimental campaigns characterized by a different conditions of the expander. Two main groups can be distinguished. The one with a 0.33 η_{vol} and the other at 0.5 η_{vol}. Clearances corresponding to these 2 sets are different. In particular it can be noted that the gap between blade tip and the stator is double at low η_{vol} (170 μm vs 85 μm). Other clearances are fixed at the same value, further highlighting the importance of the blade tip leakages with respect to other types in relation to the indicated cycle profile and the elaborated mass flowrate.

Results show the validity of the numerical software platform. Mass flowrate can be estimated with an accuracy ranging from 0.2% to 3.8%. Indicated power has lower accuracy. Maximum deviations reach 17% for case 2. Over the whole range, the average deviation is 7.8%. The higher obtained error is somewhat expected since the indicated power calculation does not come from direct measurements but it is the result of a complex procedure which has its own uncertainties.

Observing figure 5.5, a high level of physical representation can be observed in spite of the complexity of the represented processes. The intake phase is reproduced with high accuracy representing also a pressure decrease in the last phase of it: this processes is very important because it defines the quantity of the fluid inside the vane when a closed transformation is started. After the expansion, which considers also the leakages with adjacent vanes at different pressures, the pressure at the exhaust port opening is close to

Case	1	2	3	4	5	6	7	8
$\dot{m}_{WF}$	2,6%	0,2%	3,6%	9,2%	2,9%	2,9%	1,2%	3,8%
P_{ind}	9,9%	17,9%	7,1%	3,7%	4,3%	5,4%	9,4%	4,4%
P_{mech}	3,1%	7,7%	0,8%	0,2%	2,4%	0,9%	2,4%	0,9%

Table 5.3: Results of the numerical calibration of the experimental dataset

Volumetric Efficiency η_{vol}	0.50	0.33
Clearance between vane tip and stator δ	85 μm	170 μm
Clearance between vane side and rotor slot δ'	5 μm	5μm
Clearance between rotor and casing (equivalent diameter) D_{covers}	0.2 mm	0.2 mm

Table 5.4: Clearance values resulting from the calibration procedure.

the measured one, both considering the case of a matching with the outlet pressure (figure 5.5a) or a higher value which produces a isochoric expansion (figure 5.5b). Main cause of the difference is the retarded expansion after the intake closure which can be seen in the experimental case. The passage from the intake to the expansion is characterized by a difference in the curvature value. This passage is discontinuous in the numerical case while no discontinuity seems to appear in the experimental one. This issue results in a slightly anticipated expansion in the numerical case which determines a lower chamber pressure during the expansion. However this difference is not so high to undermine the validity of the results. This issue determines a little offset but the trend is comparable to the one obtained experimentally. For this reason, the accuracy has been considered satisfying for the purpose of this study.

5.3 Internal leakages definition and analysis

5.3.1 Preliminary considerations

As previously discussed, internal leakages play a major role on the elaborated mass flowrate and indicated power. The values of the calibration parameters further confirm this statement showing how clearances have to decrease sensibly if higher volumetric efficiencies must be reached.

The effect of these parameters is shown in figure 5.6. The indicated cycles, reconstructed from experimental data, are compared to the indicated cycle of an ideal expander modelled with minimum blade tip clearances. The resulting volumetric efficiency of this ideal case is close to unity. Cases at the

same expander inlet pressure and volumetric performances are shown. Making reference to figure 5.6, the expander inlet pressure stands at 11 bar. Case 1 and case 5 are characterized by an η_{vol} equal to 0.33 and 0.43 respectively. The reported trends show that when the volumetric efficiency is lower, the pressure during the expansion phase is higher. Even if this aspect could be considered beneficial, actually this increased pressure is done at the expense of a greater mass flowrate (200 g/s against 120 g/s for η_{vol} equal to 0.43). The increased mass flowrate determines higher vane to vane leakages which contributes to the sustainment of the chamber pressure resulting in a partial recovery of indicated power which can be converted in useful work. The other reported cases show similar trend at lower intake pressure. Similarly, it can be seen that the pressure offset at different η_{vol} is slightly reduced for lower pressure ratio. However similar conclusions can be made.

5.3.2 Impact of leakages

The analysis of leakages has been conducted comparing two expanders characterized by different values of tip blade clearances. The first one is represented by the reference case which is constituted by an ideal machine with a volumetric efficiency close to unity. In order to reach such performances the blade tip clearance has been set at 10 μm. Values below this one lead to numerical instability of the model and have not been considered. The other one is representative of a real machine with a volumetric efficiency equal to 0.5 and a vane tip-stator gap of 85 μm.

Expander inlet conditions have been fixed at 11.5 bar with a superheating of 19.2°C. In order to guarantee the same inlet pressure the elaborated mass flowrate is sensibly different. The reference case with higher efficiency elaborates 67 g/s while the real one 131 g/s.

Figure 5.7a compares the resulting pressure trends in the p-θ diagram. Intake starts at 342° while ending at 71°. Expansion takes place from the end of the suction phase till the opening of the exhaust port at 157°. The discharge occurs from the expansion end up to the closing of the exhaust port at 348° realizing a little angular period of overlapping with the intake. During this angular span the intake/exhaust short-circuit is prevented by the sealing of lubricating oil between the stator and the blade tip.

During the intake phase pressure oscillations can be noted when the volumetric efficiency is higher. This is due to dynamic phenomena happen-

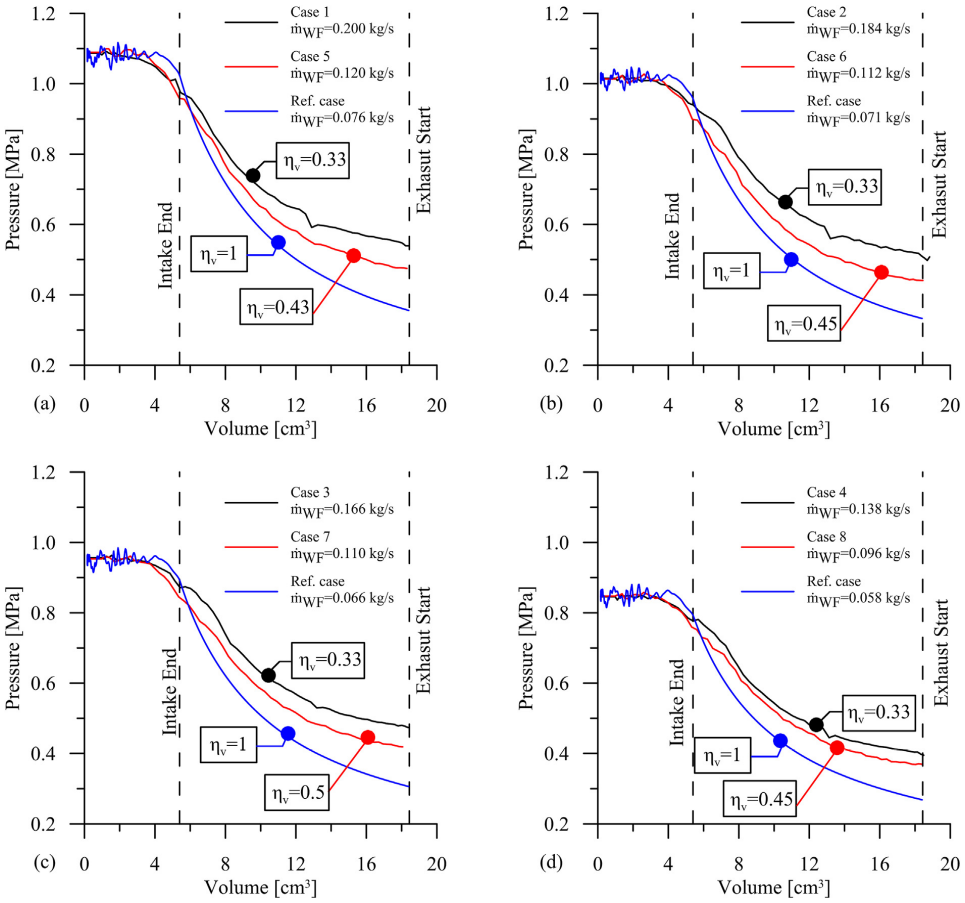

Figure 5.6: Experimental and numerical comparison between p-V diagram with different volumetric efficiencies.

ing during the filling phase of the chamber. When tip leakages are higher, the lower volumetric efficiency dampens these fluctuations resulting in a smoother filling. This issue is visible also in figure 5.7b where the instantaneous mass flowrate at the intake port is reported. Pressure oscillations are accompanied by flowrate ones which are much greater in the ideal machine representing over 50 % of the average value.

During the expansion, the increased mass flowrate of the real expander determines a higher mass inside the chamber volume which help maintaining the pressure higher than the ideal case. The phenomenon is explained in figure 5.7c where the progress of the working fluid mass inside a single vane is represented. In the ideal case, the mass increases during the intake up to the intake port closing. At this point no significant variations can be

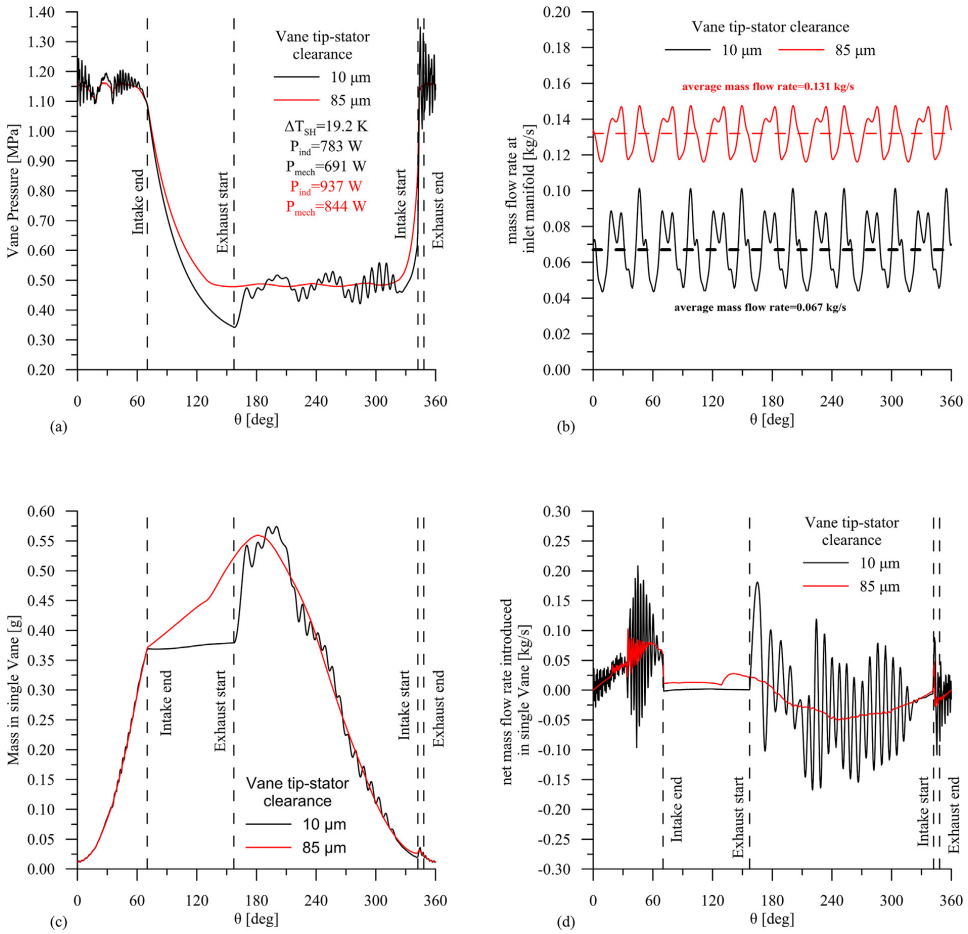

Figure 5.7: Comparison between reference and real case: p-θ diagram (a), instantaneous inlet mass flowrate (b) working fluid mass in chamber volume (c) net mass flowrate in chamber volume (d)

noted till the discharge. Tip blade clearances are not wide enough in order to allow a mass transfer between vanes. Same considerations do not apply in the real case. Clearances determine a flow among the vane and the adjacent ones. The result is that the mass inside the vane keeps on increasing during the expansion phase even if at slower rate. Figure 5.7d further confirms the behaviour showing the net $\dot{m}_{wf}$ in a single vane. For η_{vol} equal to 50% a positive $\dot{m}_{wf}$ can be seen which further increases even more near the end.

Different phenomena occur in the discharge. Thermodynamic characteristics of the working fluid trapped inside the chamber volume do not depend directly on the pressure exerted by the plant in the condenser. Due to this, pressure at the expansion end could not match with the condenser pressure.

Making reference to the ideal case, where this issue is more evident, the expansion end pressure is much lower than the external one. As a consequence, a backflow occurs when the exhaust port opens. The positive pressure difference between exhaust and chamber determines a sudden filling of the vane impeding a correct discharge and lowering the indicated power. This behaviour is less visible in the real case since the higher chamber pressure during the expansion reduces the ΔP at the exhaust start. Additional effects are represented by pressure and flowrate fluctuations (figure 5.7a and d).

In order to better understand the flow losses in sliding vane rotary expanders, the nomenclature reported in figure 5.8a will be used. Making reference to the variation of the pressure inside the vane V1, V2 represents the vane which follows while V7 the one which precedes. Intake phase starts at θ equal to 342.7° until θ equal to 71°. The expansion one starts right after the intake end up to 157°. At this point the discharge phase takes place which is the longer one in terms of angular interval. Indeed, it ends at 348.2° with little overlapping with the intake one. During this angular period (around 4°) the short circuit between the two phases is avoided by the geometrical features of the expander and the lubricating oil which guarantees the sealing between the chambers.

Indicated cycles on the p-θ diagram are reported in figure 5.8b for the real and ideal case. It can be seen the angular offset between the different pressure profiles. This corresponds to the angular width of each vane which is equal to 51.4°. It is worth noting also the pressure differences existing between vanes. Making reference to V1 in can be seen that between 18° and 133°, pressure in V1 is greater than in V2. This involves the second half of the intake phase and part of the expansion one. At the same time, during all the expansion phase, pressure in V2 is greater than the one in V1 from 71° to 187°. This pressure difference explains the phenomena reported in figure 5.9.

Figure 5.9 show the mass flowrate exchanged between V1 and the adjacent vanes (V2 and V7) as a function of the angular position θ. As a consequence of the positive pressure difference between V1 and V7, from 18° till 130°, a negative flowrate can be noted. This means that the working fluid in chamber V1 flows from V1 to V7. The exchanged mass flowrate sharply decreases at 18° due to the beginning of the expansion phase in V1, increasing as the expansion takes place due to the lower pressure difference

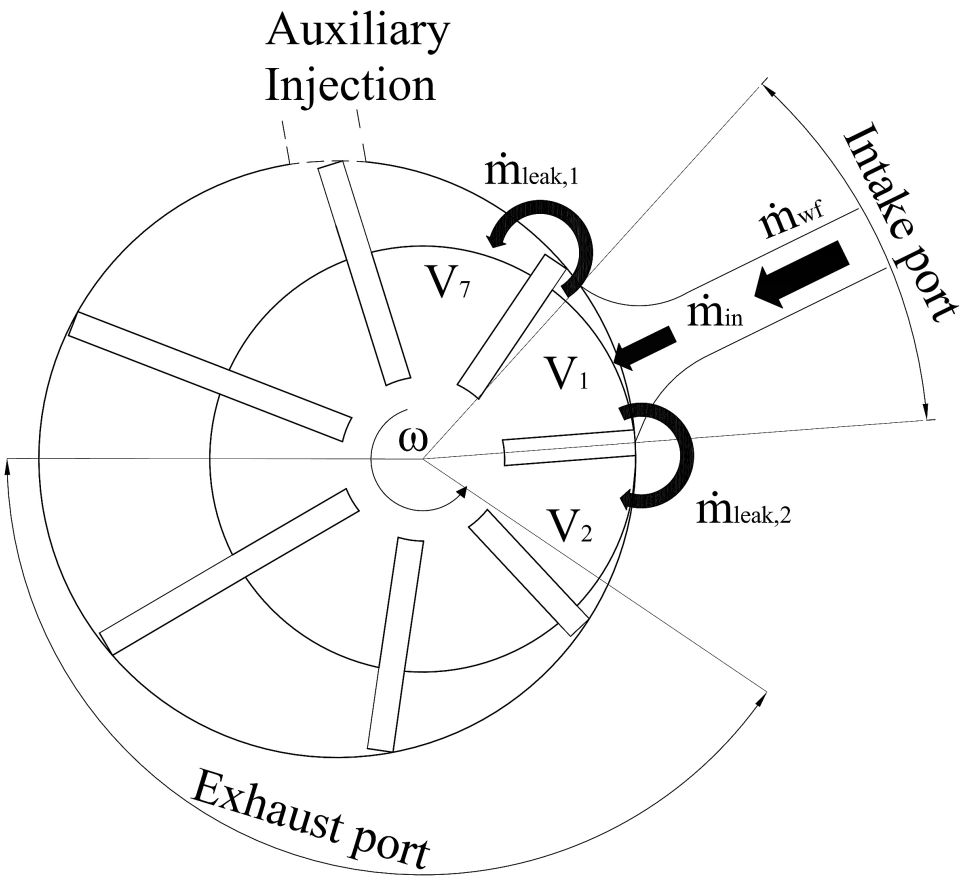

(a)

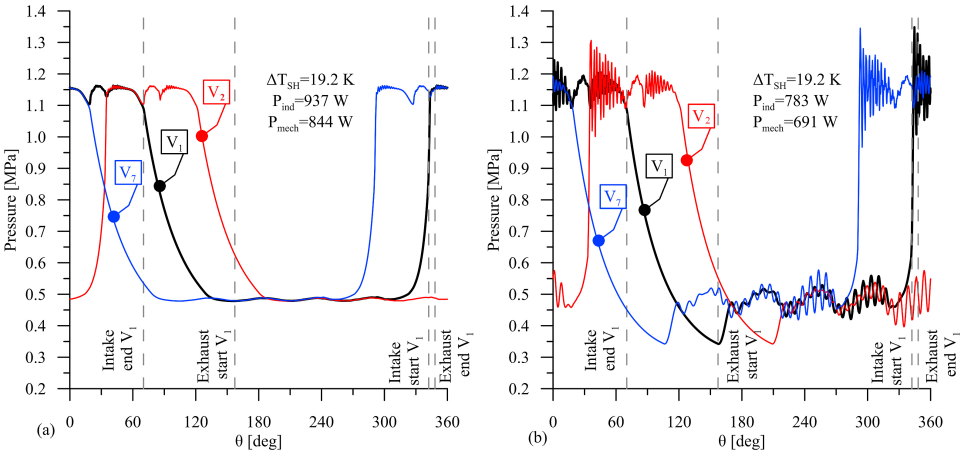

(b)

Figure 5.8: Schematic diagram of leakages path in sliding vane rotary machines (a) and pressure trend phasing in the p-θ diagram for between different vanes.

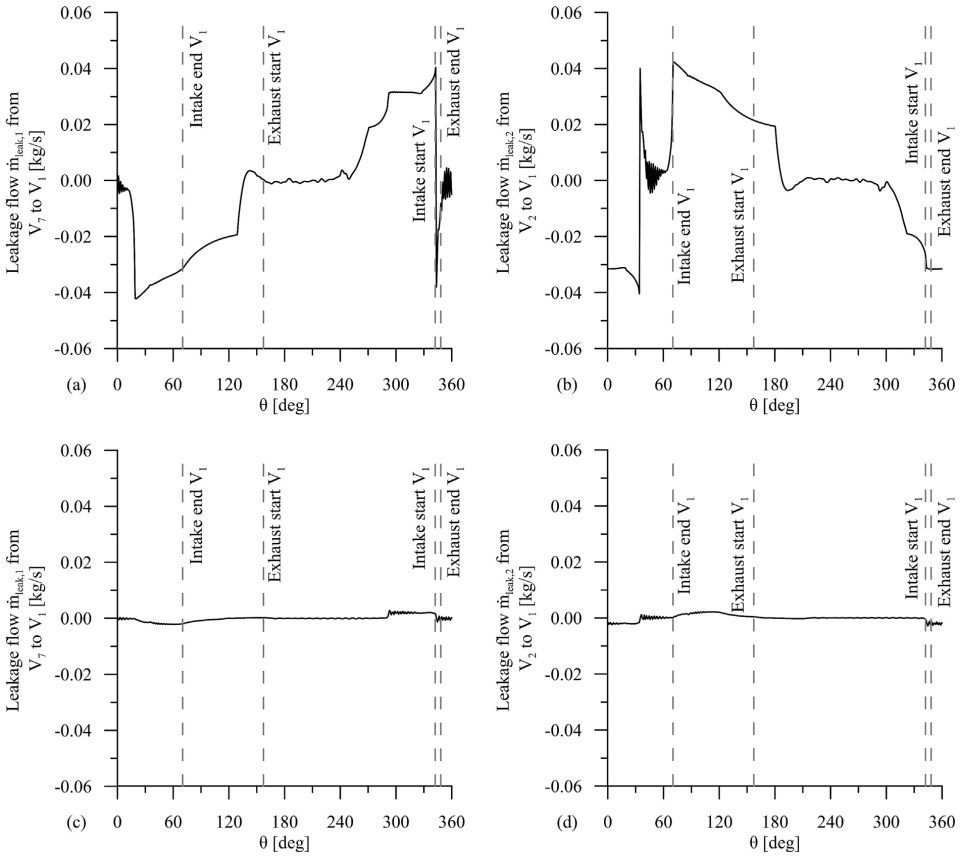

Figure 5.9: Leakage flows in real case (a) and (b) and in the ideal case (c) and (d).

which approach 0 right before the discharge start. The leakage flow remains almost constant during the first part of the exhaust increasing suddenly at 250°. At this point, V7 restarts the intake phase, increasing the chamber pressure and causing a positive flowrate towards V1.

Leakage flows between V1 and V2 are reported in figure 5.9b. From 0° to 35° V1 is in the filling phase while V2 is discharging. $p(V_1)$ is higher than $p(V_2)$ determining a working fluid flow towards V2. This $\dot{m}_{leak}$ stops approximately at the intake end. After that the expansion of V1 takes place, chamber pressure decreases while V2 is still aspirating. Working fluid mass moves from V2 to V1 till no more pressure difference is available at 187°. Here both chambers are emptying and pressures are equal. This situation occurs till to 300° when V1 approaches a new filling phase while V2 is still emptying. As a consequence, $\dot{m}_{leak}$ moves from V1 to V2. It is important

to note that during the exhaust of V1, both V2 and V7 have a positive pressure difference in various angular period with respect to V1 worsening the emptying phase which is obstructed by the working fluid mass moving from other vanes.

With reference to the ideal case shown in figure 5.9c and figure 5.9d no sensible leaks can be noted and mass flowrates are negligible. The absence of important clearances determine this behaviour despite pressure difference being similar in the two cases. Indeed, as previously explained, leakage losses are modelled through the Poiseuille-Couette equation in the following way:

$$Q_{leak} = A_{blade,tip}\left(\frac{\delta^2 \Delta P}{12\mu L_{leak}} + \frac{1}{2}u_{blade,tip}\right) \tag{5.15}$$

where δ is the clearance gap, L_{leak} the length of the clearance and $u_{blade,tip}$ the peripheral speed of the blade evaluated at the tip. The leakage volumetric flowrate depends on the clearance gap squared which nullifies the effect of the pressure difference ΔP. The working fluid choice influences leaks in a direct way through the viscosity μ. The higher the viscosity the lower the leaks. In addition to that, the fluid density plays an important role. When this is higher, the fluid depositing on the stator surface is greater and the sealing between chambers improves. Moreover, it is usually mixed with lubricating oil which reduce even more the probability of the working fluid to flow from a vane to the other. This latter aspect does not appear directly in the above equation. However, since the clearance gap is a calibration parameter, if a higher density working fluid is used, it would lead to a reduction of the gap in the validation of the model.

In figure 5.10 3 cases are shown:

- Case 1: real case with η_{vol} equal to 50% (figure 5.10a)
- Case 2: Ideal case (figure 5.10a)
- Case 3: Larger ideal machine whose elaborated mass flowrate equals the one of case 1 (figure 5.10b

The ideal expander of case 3 is obtained with a larger intake volume which is able to elaborate a higher flowrate. This can be easily achieved through an increase of the stator diameter or raising the axial length. The aim of the comparison is to identify the effect of leakages in the indicated cycle and to

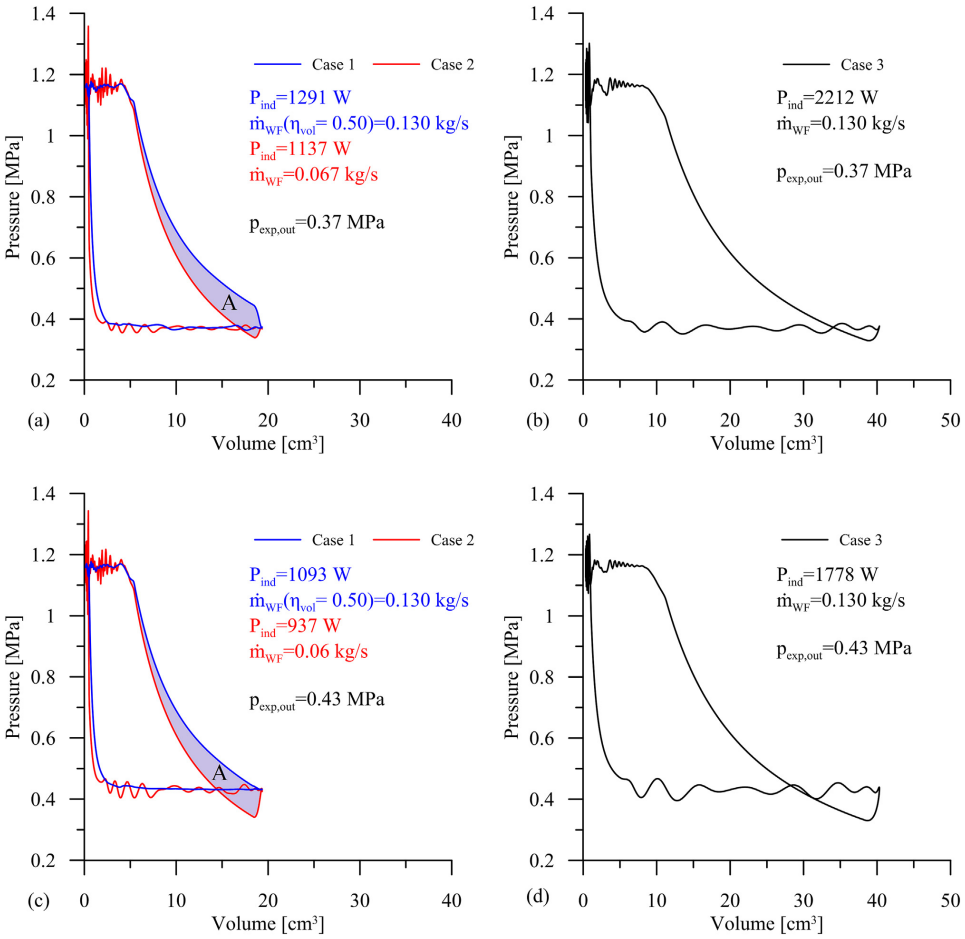

Figure 5.10: Indicated cycle comparison for different boundary conditions.

understand the extent of the partial energy recovery. With reference to the comparison between case 1 and case 2, leakages determines a higher closed area in the p-V diagram. The difference is represented by the area "A" which account for 13.5% of the total area in case 2. The real case is characterized by a greater output even if at lower overall efficiency. The mass flowrate is much greater in the real case, producing vane to vane leakages which determine the pressure sustainment during the expansion phase. Comparing the ideal case with the one of case 3 it is worth noting how the ratio between the two indicated power equals the one between mass flowrates. This is a direct consequence of the ideal volumetric behaviour of the expanders with the whole flowrate being elaborated inside the vanes. Obviously, the presence of non negligible clearances in a real case scenario breaks this proportionality,

especially considering that with higher dimensions also the gaps increase.

Figure 5.10c and d reports the same kind of comparison in a situation where the ideal case is characterized by a higher overexpansion. It can be noted that the chamber pressure at the expansion end is lower than the exhaust one, producing a back-flow and a negative work. In this case the partial recovery represented with the area "A" has a greater contribution, representing 16.6 % of the indicated power of the ideal case.

The obtained results allowed to understand the leakage effects of the performances of a sliding vane expander. Even if their detrimental effect is confirmed, they can be seen in a different light due to the partial energy recovery which is possible to obtain. Indeed, the design of an ideal machine with minimum clearances and a unitary volumetric efficiency is a quite impossible task in the field of positive displacement expanders. The analysis will help improve the design of such devices, in particular when considering the trade-off between mechanical and volumetric losses.

5.4 Effect of dual intake

As already seen in the experimental analysis shown in the previous chapter, the dual intake system allows a massive increase of the indicated power without the need for higher chamber pressure, avoiding problems related to the reliability and safety of the unit.

An analysis on the effect of the dual intake on the volumetric performances of the expander has been carried out. To understand the following considerations, the nomenclature reported in figure 5.11 must be explained. Moreover, for a better explanation, the single intake expander and the dual intake expander will be referenced as SIP and DIP respectively. The intake and exhaust port angular extensions and positions are the same for the OEM expander and the DIP one. $\Delta\Phi_{dual,int}$ is the angular width of the auxiliary port between $\theta_{dualint,start}$ and $\theta_{dualint,end}$ and is maintained fixed in the analysis. Its value is 12° which represents 15% of the main one. On the other hand, $\Phi_{dual,int}$ represents the angle between the main intake end $\theta_{int,start}$ and the auxiliary start $\theta_{dualint,start}$. This parameter has been varied in order to understand the best positioning in relation to leakage flows and volumetric losses.

Analysis have been conducted at the same boundary conditions reported

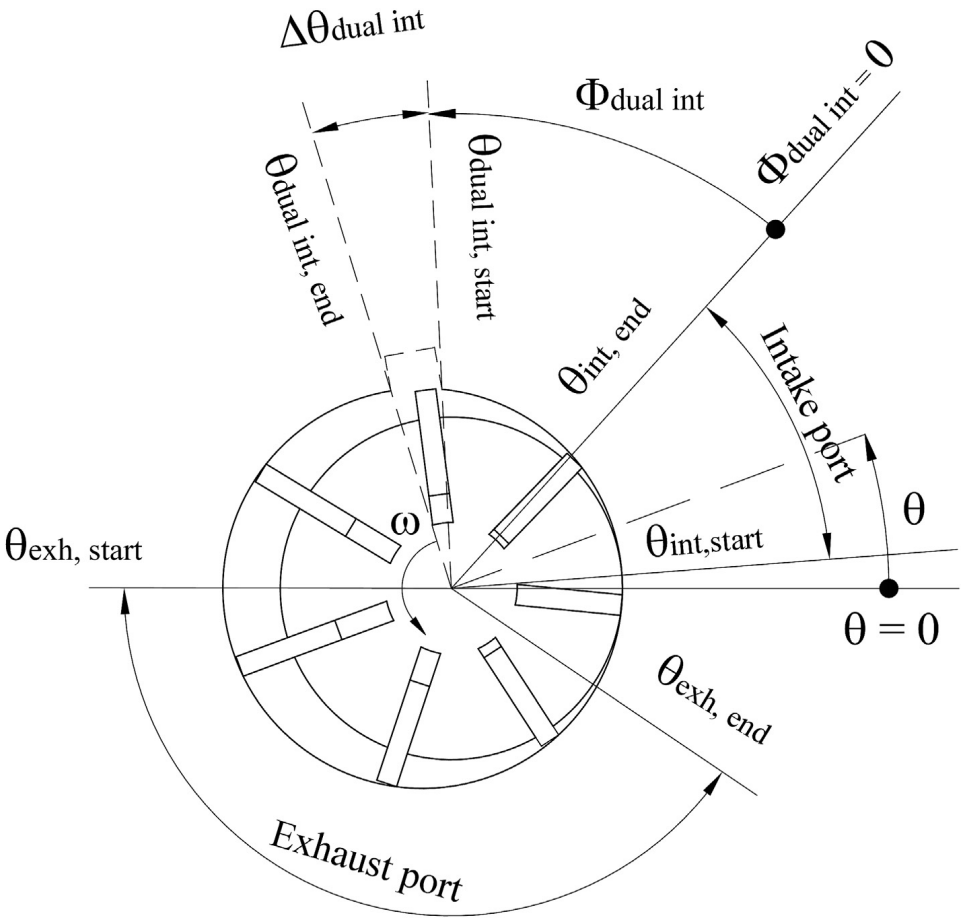

Figure 5.11: Scheme of the dual intake expander and nomenclature.

above and the same calibration parameters found in the previous section. The only input parameter which has varied is $\Phi_{dual,int}$. Results are reported in table 5.5. In order to describe the effect of leakage in a synthetic way, a new parameter namely leakage impact has been introduced. It is defined as the ratio between the vane to vane average flowrate and the total flowrate at the intake port inlet. In this way it is possible to asses the extent of leakages in the different cases since they are characterized by very different $\dot{m}_{wf}$. $\Phi_{dual,int}$ has been varied between 4° and 64.7°. Values below the angular width of the vane (51.4°) involve an overlapping between the main intake and the auxiliary one with this latter starting when the first is not finished yet. The highest investigated angle has been limited by the maximum volume reached by the chamber. Above this value the second intake is put in communication directly with the exhaust, determining poorer performances.

$\Phi_{dual,int}$ [°]	$\dot{m}_{leak}$ V2/V1 [kg/s]	$\dot{m}_{leak}$ V1/V7 [kg/s]	$\dot{m}_{WF}$ [kg/s]	Leakage impact [%]	P_{mech} [W]	$\Delta\eta_{mech}$ [%]	$\Delta\eta_{vol}$ [%]
Single-intake	0,003	0,003	0,132	2,50%	844	-	-
1,3	0,006	0,006	0,16	3,70%	1251	+3%	+28%
8,4	0,006	0,006	0,174	3,50%	1405	+3%	+28%
15,4	0,006	0,006	0,191	3,40%	1554	+4%	+28%
22,4	0,007	0,007	0,206	3,20%	1674	+4%	+28%
29,5	0,006	0,006	0,222	2,90%	1770	+4%	+23%
36,5	0,006	0,006	0,237	2,60%	1841	+4%	+21%
43,6	0,006	0,006	0,249	2,20%	1882	+6%	+19%
50,6	0,004	0,004	0,26	1,60%	1905	+6%	+14%
57,7	0,003	0,003	0,27	1,00%	1917	+6%	+9%
64,7	0,001	0,001	0,279	0,40%	1913	+6%	+7%

Table 5.5: Dual intake expander performances at different position of the dual port.

As previously noted, the mechanical and indicated power show a sharp increase till the maximum investigated value of $\Delta\Phi_{dual,int}$. The trend agrees with the studies reported in [162] and [163]. Mechanical power grows from 844 W to 1917 W at $\Delta\Phi_{dual,int} = 57.7°$. At the same time an increase of the mass flowrate can be noted even if with a slower rate. The ratio between the OEM mass flowrate and the one corresponding to the maximum power is lower than the ratio between mechanical power outputs. This leads also to a higher efficiency of the machine with the dual intake port. Volumetric performances also improve with the dual port. Compared to the single intake port expander, maximum relative increase stands at +28% when the dual port is positioned right after the main intake end. Anyway, a certain improvement is visible in all the considered values of $\Phi_{dual,int}$. In addition to that, also the mechanical efficiency reports little improvements. η_{mech} is defined as the ratio between mechanical and indicated power. The difference is due to the friction losses given by the relative motion between the revolving blades and the stator inner surface. These latter are mainly influenced by the rotational speed of the expander which determines a greater centrifugal force increasing friction forces. Since the rotational speed is fixed at 1500 RPM in all cases but the indicated power strongly increases at higher $\Phi_{dual,int}$, the mechanical efficiency also increases.

The leakage impact starts decreasing at $\Phi_{dual,int}$ greater that 36.5°. In order to understand the reasons of the better volumetric performances a comparison between the p-θ diagram of the SIP and DIP expander over a whole rotation is reported in figure 5.12. In figure 5.12a the SIP case is

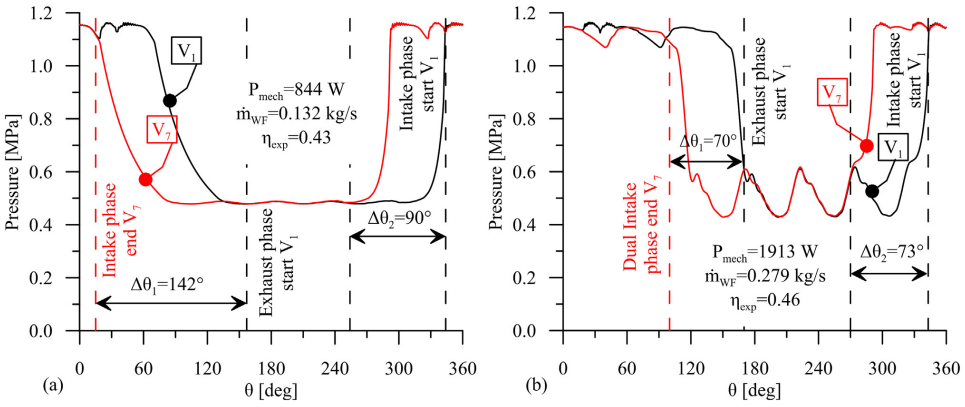

Figure 5.12: Angular phasing of chamber pressure in the p-θ diagram.

showed. Chamber pressures for two adjacent vanes is represented which are shifted by an angle equal to the angular width of the vane. Two angular intervals are reported, namely $\Delta\theta_1$ and $\Delta\theta_2$. The first one is the angle comprised between the exhaust start of V1 and the intake end of V2 and has a value of 142°. $\Delta\theta_2$ is the angle from the exhaust end of V7 and the intake start of V1 with a value of 90°. Both of them are characterized by a sensible pressure difference between adjacent chambers.

The same representation is shown in figure 5.12b for the dual intake port expander when $\Phi_{dual,int}$ is 65°. The extent of $\Delta\theta_1$ and $\Delta\theta_2$ is lower, passing from 142° to 70° and 90° to 73° respectively. The reduction of the angular extent in which the pressure difference exists results in a lower time period for the leakages to happen, consequently determining lower volumetric losses. The second injection determines quite a constant pressure trend in the cycle. The expansion phase takes place in few degrees of rotation between the end of the main one and the beginning of the auxiliary. During this period of 20°, the pressure difference is too low and leakage flows are negligible. In this way flow losses are restricted to the angles $\Delta\theta_1$ and $\Delta\theta_2$ which, as seen, are lower compared to the SIP case.

Figure 5.13 reports the cumulative mass flowing through the leakages between adjacent vanes. In the SIP case (figure 5.13a and b), it is possible to note how the inlet mass flowrate during the intake phase of V1 flows also towards V2 and V7. This is the main cause of the pressure reduction at the intake which causes a lower volumetric efficiency. During the expansion the working fluid flows from V1 to V7 and from V2 to V1. Looking at the

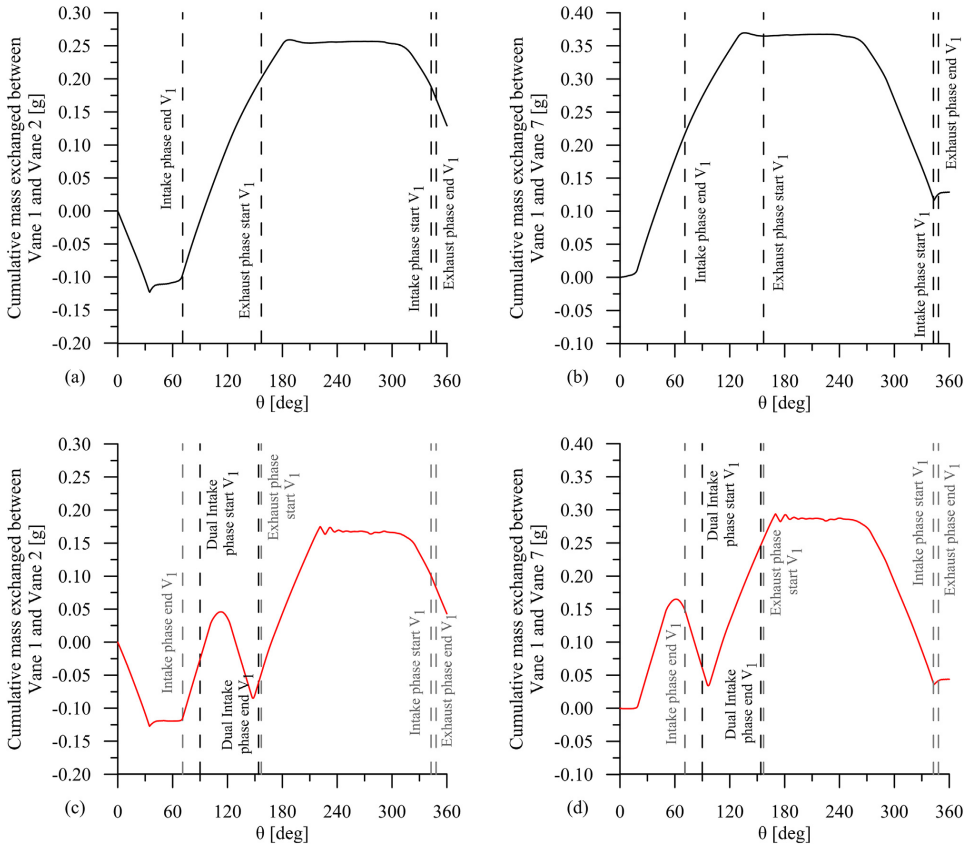

Figure 5.13: Cumulative mass in chamber volume in p-θ diagram. OEM expander (a) and DIP expander (b).

slope of the curve during the expansion of V1 from 70° to 150°, it can be noted that the mass exchanged between V2 and V1 is much higher than in the other case. This behaviour justifies the pressure sustainment during the expansion.

When the dual port is considered, a similar trend during the intake phase of V1 is visible. On the other hand, after that, the presence of the dual intake determines a lower cumulative mass exchanged through the leakages given by the reduction of $\Delta\theta_1$ and $\Delta\theta_2$.

The numerical results demonstrate that the dual intake port can be considered as a valid alternative for sliding vane expander to improve indicated and mechanical performances as well as volumetric ones. According to design options available in literature studies, leakage losses are reduced, increasing the number of the vanes or the force acting on the bottom of the blades.

Even if this could represent a solution, both of them increase friction effects, lowering the mechanical efficiency. In contrast, the tested and modelled solution can guarantee an overall improvement of the device. A potential downside is that an increase of the mass flowrate elaborated by the pump of the ORC unit is necessary in order to operate properly the expander. This involves that a greater thermal energy need to be recovered which is not always available in the hot source. In order to limit this drawback a further step forward in the design of such machines will be presented in the following chapter.

5.5 Conclusions

In this chapter a characterization of the performances of a sliding vane expander with a dual intake port has been carried out. The experimental results reported in the previous chapter have been used for the calibration of a numerical model which allowed to assess the thermo-fluid dynamic phenomena occurring inside the chamber volumes. The modelling activity permitted to understand also the effect of leakages on the volumetric performances of the machine. Main results show that the primary cause of volumetric losses is represented by the leakages occurring at tip blade. This aspect is evidenced by the values of the calibration parameters (clearance gaps) obtained in the validation phase of the model. The effects of them on the indicated diagram has been observed. The leakages during the intake phase determine a lower inlet pressure. On the other hand, leakages during the expansion phase determine a pressure sustainment which increases the chamber pressure with respect to an ideal case, recovering part of the energy lost. The dual intake can reduce such phenomena, decreasing the angle intervals in which a pressure difference is observed between adjacent vanes, reducing the flow losses. This latter aspect could represent a valid solution for the increase of volumetric efficiencies without the reduction of the mechanical performances which are greatly penalized by more conventional solutions.

Chapter 6

Dual Intake design and modelling options in sliding vane rotary expanders.

6.1 Introduction

In the previous sections of this manuscript, the performances of a sliding vane expander with a single and a double intake port have been reported together with the effects of this novel system on leakages and volumetric losses. The analyses have shown a good improvement potential which will be further outlined and reinforced in this chapter. However, also drawbacks have been found, mainly related to the increased working fluid mass flowrate needed to reach suitable expander inlet pressures even if this feature could be of interest when an additional thermal energy must be recovered. For these reasons, a new modelling approach for the design of a dual port expander will be presented.The design methodology could allow to improve also the traditional revolving vane expander.

6.2 Dual intake port results

Experimental data reported in table 6.1 have been used for the calibration of the model. With respect to the previous training dataset, they have been improved with the addition of a flow-meter on the auxiliary line. In this way the mass flowrate entering through the second port has been measured and

			1	2	3	4	5	6
ϕ			100%	100%	100%	60%	50%	45%
ω	±1	RPM	1517	1514	1512	1518	1521	1521
$\dot{m}_{wf,main}$	±0.5%	[g/s]	49	46	44	61	71	69
$\dot{m}_{wf,dualint}$	±0.5%	[g/s]	80	73	67	70	59	50
$p_{int,main}$	±0.3	[bar]	6,1	5,6	5,3	6,4	6,4	6
$p_{dualint}$	±0.3	[bar]	5,7	5,4	5,1	5,6	5,4	4,7
$p_{exp,out}$	±0.3	[bar]	3,6	3,3	3,1	3,6	3,2	3
$T_{exp,in}$	±0.03	[°C]	78,9	70,4	77,2	79,5	78,9	64,7
$T_{exp,out}$	±0.03	[°C]	72,8	63,4	71,2	71,9	70,2	54,9
P_{ind}	±0,02	[W]	535	507	469	565	639	541
P_{mech}	±0.8%	[W]	304	270	263	323	398	329
η_{vol}	±2.3%	[%]	59	60	59	57	55	57
η_{mech}	±2.8%	[%]	57	53	56	57	62	61
η_{global}	±0,01	[%]	26	25	26	25	25	25

Table 6.1: Dual intake expander experimental data at different valve opening ϕ

used as a validation parameter for the numerical model.

Experimental operating points have been taken at different working fluid flowrates elaborated by the pump. Moreover, in cases 4, 5 and 6 a different opening (ϕ) of the admission valve positioned right before the dual intake port has been set. Values at ϕ equal to 100 % correspond to a fully open valve. The aim was to study the different repartition of the flowrate between the admission pipes when the throttling valve is partially closed.

Cases 1, 2 and 3 have been taken at ϕ equal to 100 %. In these cases mass flowrates in the second admission pipe was about 60 % of the total one elaborated in the pump. Expander inlet pressure increases linearly at higher mass flowrate from 5.3 bar to 6.1 bar. Outlet pressure was kept approximately constant at 3.3 bar. Mechanical power output increases from 263 W to 304 W when $\dot{m_{wf,main}}$ increases. Global efficiency stands at 26%, even if they are severely affected by the poor mechanical performances. A separate analysis for such values (below 60 %) will be reported in the following section. Volumetric performances confirm theoretical expectations with values around 60 %. Expander outlet temperatures show little decrease compared to the inlet ones. This is due to the reduced expansion phase which happens only in few degrees of rotation between the end of the intake phase and the beginning of the auxiliary one.

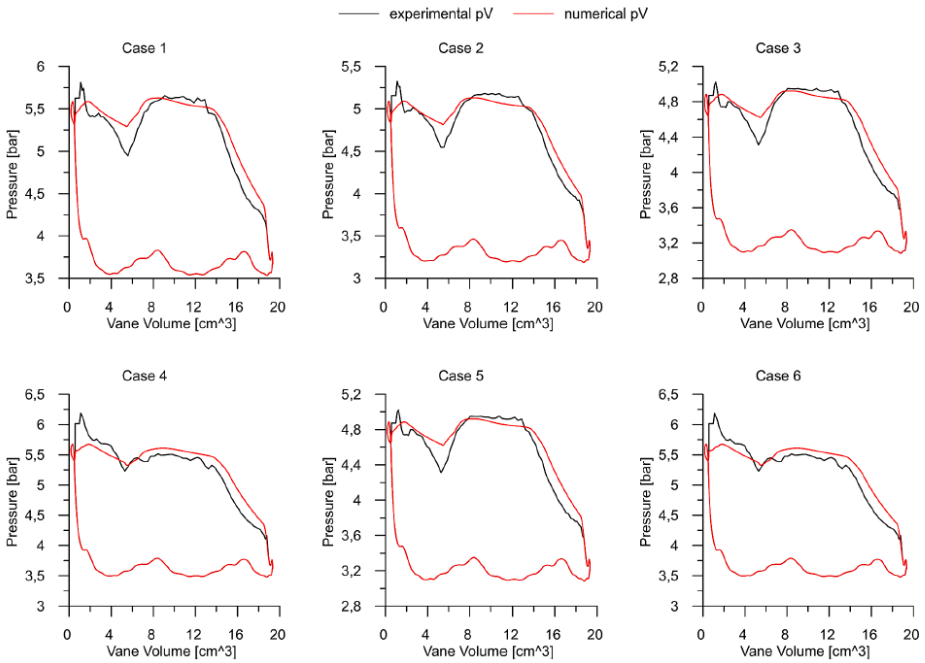

Figure 6.1: Experimental and numerical indicated cycles of the operating points reported in table 6.3

When the valve on the auxiliary admission pipe is partially closed from 100 % to 45 % several considerations can be done. First of all, the closure of the valve determines a lower mass flowing in the auxiliary line ($\dot{m}_{wf,dualint}$). Moving from $\phi = 100\%$ to $\phi = 45\%$, $\dot{m}_{wf,dualint}$ decreases from 62% to 42% compared to the total working fluid mass flowrate elaborated by the pump $\dot{m}_{wf}$. In particular, looking at cases 1, 4 and 5, which are characterized by the same $\dot{m}_{wf}$ of 130 g/s, $\dot{m}_{wf,dualint}$ decreased from 80 g/s to 59 g/s. At the same time, a slight decrease of the pressure at the dual intake can be observed together with a little increase in the expander inlet pressure because of the increased overall hydraulic resistance of the machine. As a consequence of that, a slight increase of the produced mechanical power can be observed between case 1 and 5. However, part of this can be attributed to the reduced condenser pressure which increases the indicated power related to the isochoric expansion. Further confirmation of this contribution is provided by the analysis on the overall efficiency which shows the same values in both cases. In contrast, the higher average pressure in the chamber causes a moderate decrease of η_{vol} (2-3 percentage points).

Type	value
Vane tip leakages clearance gap	75 μm
Vane side leakage clearance gap	40 μm
Covers/ Rotor faces leakage clearance gap	47 μm
Friction coefficient C_{tip}	0.05

Table 6.2: Results of the calibration parameters of the DIP expander numerical model.

Cases	$\dot{m}_{wf,main}$	$\dot{m}_{wf,dualint}$	$p_{int,main}$	$p_{dualint}$	P_{ind}	P_{mech}
1	6,8	4,1	2,6	2,9	1,1	0,4
2	5,2	2,9	2,5	0,5	5,5	2,7
3	3,3	1,9	2,6	0,8	0,6	0,8
4	4,2	3,6	3,2	2,7	0,6	2,2
5	0,9	1	1,8	3,7	6,7	1,5
6	4,5	6,4	1,4	2,7	8,8	7
RMSE	2	1,9	0,6	1,3	3,6	2,4

Table 6.3: Deviation between numerical and experimental results for cases reported in table 6.1

Experimental and numerical indicated cycles are depicted in figure 6.1. Values of the calibration parameters resulting from the validation procedure are reported in table 6.2. The numerical indicated cycle approximates quite well the experimental trend. Some greater differences in the chamber pressure are evident between the end of the main suction phase and the beginning of the auxiliary one. This is due to complex dynamic phenomena happening inside the vane which can be hard to describe through a 0D model. However, except for this issue, the numerical trend agree with the experimental one as can be noted from the results reported in table 6.1. Deviation of mass flowrate, pressure as well as indicated and mechanical power show a root mean square error on the whole dataset lower than 5%. Since the exhaust phase has not been measured, the same exhaust phase between the numerical and experimental case has been considered. Deviations in the indicated power have been evaluated only in the common part of the indicated cycle.

Clearances gap show lower values compared to the SIP expander gaps presented in chapter 4. As explained, clearance gaps do not have an immediate physical meaning but they are varied to increase or lower leakage flow losses. In this sense, their reduction with respect to the SIP device confirms that this system allows the improvement of volumetric performances.

Operating conditions	SIP	DIP
Intake pressure p_{in} ± 0,3 [bar]	7,7	5,93
Intake Temperature T_{in} ± 0,03 [°C]	75	70
Elaborated mass flow rate $\dot{m_{wf}}$ ± 0,5% [g/s]	130	130
Exhaust pressure p_{exh} ± 0,3 [bar]	3,23	3,16
Indicated Power±2% P_{ind} [W]	816	622
Mechanical power P_{mech} ± 0,8% [W]	650	367
Mechanical Efficiency±2,8% η_{mech} [%]	79,6	58,9
Volumetric Efficiency±2,3% η_{vol} [%]	42	58,3
Indicated Efficiency±2,5% η_{ind} [%]	39,6	45,7
Global efficiency±1% η_{global} [%]	31,5	27

Table 6.4: SIP and DIP expander performances comparison at the same working fluid mass flowrate.

6.3 Mechanical efficiency analysis

In figure 6.2 a comparison between the expander with a single intake port (SIP) and the the dual intake port (DIP) is reported. Two cases are represented at the same elaborated working fluid mass flowrate and exhaust pressure. The analysis of the indicated cycle in the p-V diagram shows that despite the energy recovery of the DIP during the second phase of the SIP expansion, the reduced chamber pressure during the intake does not allow to obtain the same performances. For a mass flowrate equal to 130 g/s, inlet pressure decreases from 7.7 bar to 5.9 bar. Indicated power shows a reduction of 23 %, passing from 816 W to 622 W. In contrast, the indicated efficiency, evaluated as the indicated to isentropic power ratio, increased by 15.6 % from 39.6 % to 45.7 %. This latter result clearly shows the potential advantage of the dual port technology.

The mechanical power results deserves some further considerations. It can be noted in table 6.4 a significant decrease of the mechanical efficiency of the expander between the two configurations. As already observed, the numerical model allows the evaluation of different kind of friction forces. These are constituted by the dry and viscous friction forces occurring because of the relative motion between rotor and stator components. However, the dominant phenomenon is the dry contact between the blade tip and the stator inner surface (figure 6.3). Other types determine smaller contributions, several order of magnitude lower that the above one. The associated dry friction power lost is expressed as:

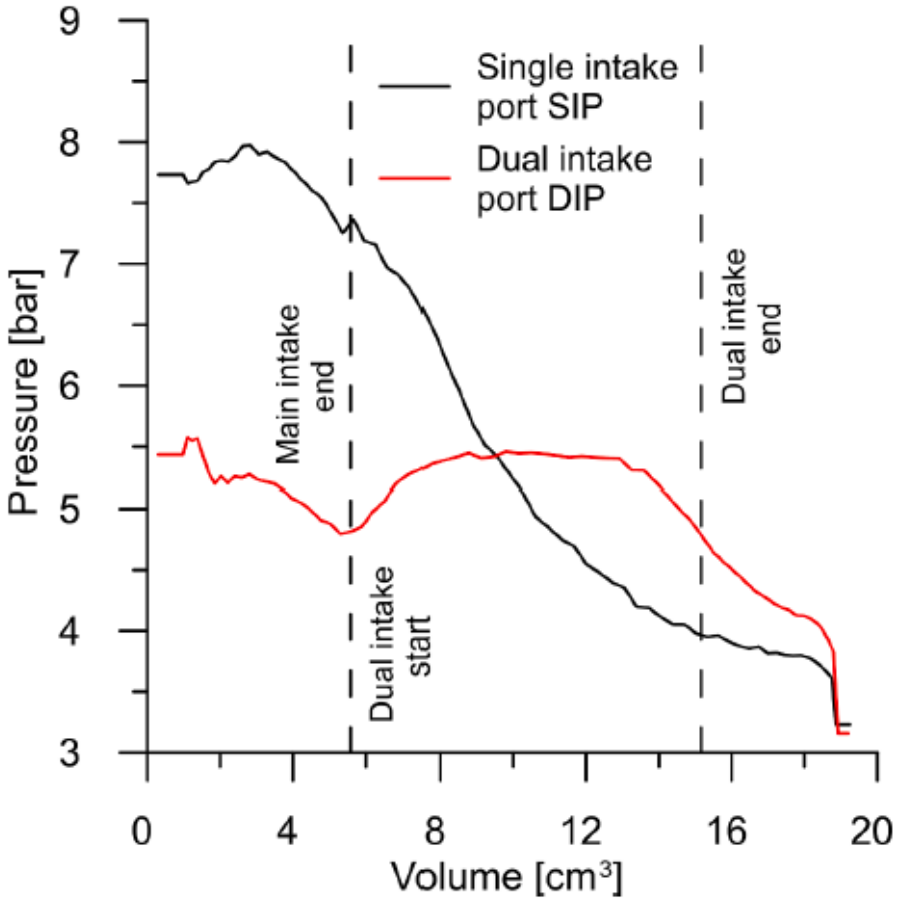

Figure 6.2: Indicated cycle comparison between SIP and DIP expander at the same working fluid mass flowrate.

$$P_f = N_v C_{f,tip} (F_p + F_c) R_b \omega \tag{6.1}$$

where N_v is the number of the vanes, $F_p + F_c$ the normal force and R_b the distance between the blade tip and the rotor center. $F_p + F_c$ represents the sum of the centrifugal force and the hydrostatic force. The first one is given by the rotational speed of the expander, while the second is proportional to the pressure inside the vane which acts on the blade bottom because of the fluid in the interstice of the rotor which further pushes the tip against the stator increasing the normal force. C_{tip} is the friction coefficient which is primarily given by the nature of the materials in contact and the lubricating conditions. This coefficient has been assumed as a calibration parameter.

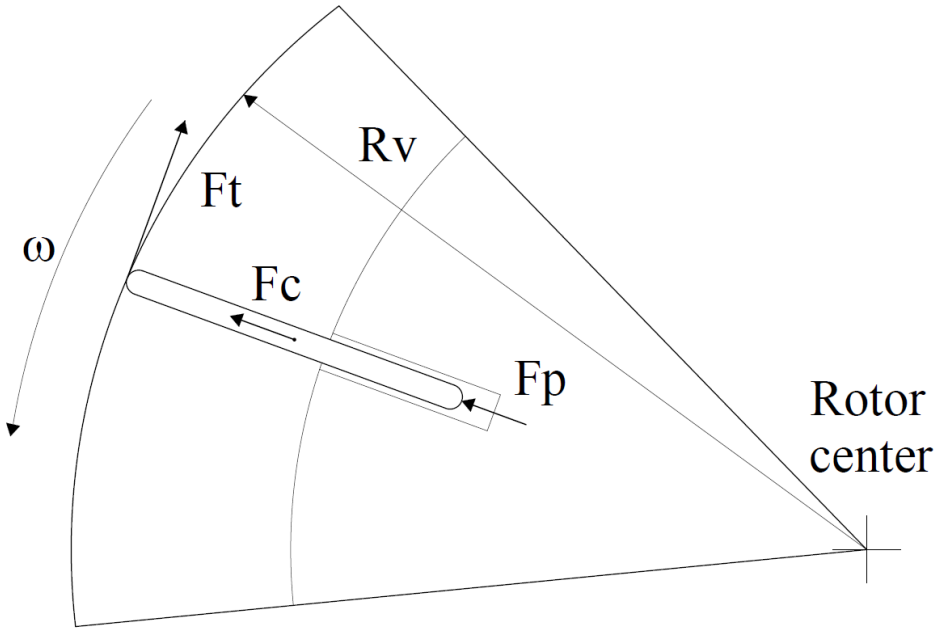

Figure 6.3: Scheme of dry friction force acting on the blade tip of the expander.

The results reported in the previous section showed that in the dual intake case its value is equal to 0.05 against the 0.01 found in the single intake expander. Since in the DIP case the lower chamber pressure should guarantee a lower normal force and the lubricating conditions have not been varied between the experimental campaigns, this difference has been attributed to the wearing of the stator surface and the blade tips which eventually determined this increase in friction losses. For these reasons, in the analyses developed in the following sections, a common friction coefficient equal to 0.01 has been assumed.

6.4 Theoretical analysis

The comparison reported above in table 6.4 shows a lower mechanical power of the dual intake port expander compared to the OEM version. The main reason is that the dual port is made on an existing machine rather than on a newly conceived one. The aim of the following analysis is to support the design of a new machine, able to close the gap with the single intake one to reach the same inlet pressure when the mass flowrate is similar, without

undermining the beneficial effects on the volumetric performances. In this way it could be possible to achieve better performances in terms of indicated efficiency.

The determination of the geometrical features of the expander to guarantee a certain inlet pressure flowrate proportionality is not straightforward. The developed numerical model can fulfil this task only through some iterations. In order to simplify this task, some preliminary theoretical considerations must be done.

When the working fluid is superheated vapour the equation of state can be written as follows:

$$\frac{p_{int,end}}{\rho_{int,end}} = ZRT_{in} \tag{6.2}$$

which represents the equation of state of an ideal gas with a compression factor Z to take into account the real behaviour of the working fluid. At the same time, the working fluid density can be expressed through the following equation considering the working fluid mass flowrate at the expander inlet:

$$\dot{m}_{wf} = \frac{N_v \rho_{int,end} V_{int,end} n}{\eta_{vol}} \rightarrow \rho_{int,end} = \frac{\eta_{vol}}{N_v V_{int,end} n} \dot{m}_{wf} \tag{6.3}$$

with the meaning of each parameter already discussed in previous sections.

Comparing equation 6.2 and 6.3, the expander inlet pressure can be written as a function of the inlet mass flowrate $\dot{m}_{wf}$ and the volumetric efficiency η_{vol} as follows:

$$p_{in} = \frac{ZRT_{in}\eta_{vol}}{N_v V_{in} n} \dot{m}_{wf} \tag{6.4}$$

An additional term related to pressure losses due to the throttling effect of the inlet port can be added as well:

$$p_{in} = \frac{ZRT_{in}\eta_{vol}}{N_v V_{in} n} \dot{m}_{wf} + \Delta p_{loss} \tag{6.5}$$

which can be transformed in linear form interpolating experimental data as:

$$\Delta p_{loss} = \overline{k} \dot{m}_{wf} + \overline{q} \tag{6.6}$$

In a similar way, the same representation can be used also for the dual intake port. Equation 6.2 and 6.3 can be readapted in the following way:

$$\rho_{glob} = \frac{\eta_{vol_{main}} \dot{m}_{wf,main} + \eta_{vol_{dualint}} \dot{m}_{wf,dualint}}{N_v V_{dual,int} n} \tag{6.7}$$

which leads to:

$$p_{in} = \frac{ZRT_{in}}{N_v V_{dualint} n} (\eta_{vol_{main}} k_1 + \eta_{vol_{dualint}} k_2) \dot{m}_{wf} + \Delta p_{loss} \tag{6.8}$$

which is the equivalent of equation 6.5 for the DIP expander. k_1 and k_2 represent the quantity of the total mass flowrate $\dot{m}_{wf}$ flowing in the two admission pipes evaluated as follows:

$$\begin{aligned} k_1 &= \frac{\dot{m}_{wf,main}}{\dot{m}_{wf}} \\ k_2 &= \frac{\dot{m}_{wf,dualint}}{\dot{m}_{wf}} \end{aligned} \tag{6.9}$$

Comparing the two different formulations of theinlet pressure for the DIP and SIP expander, it can be found the relationship between the overall volumetric efficiency and the working fluid flowrate in the two admission pipes:

$$\eta_{vol_{glob}} = \eta_{vol_{main}} k_1 + \eta_{vol_{dualint}} k_2 \tag{6.10}$$

It can be noted in this relation that the overall volumetric efficiency can be thought as a weighted average of the volumetric performances in the two filling phases based on the working fluid flowrate entering the two ports.

Values of k_1 and k_2 have been experimentally evaluated at ϕ equals to 100 %. In this case they show a slight dependence on the total elaborated mass flowrate as observed through the linear fitting in figure 6.4. In figure 6.5, the volumetric efficiency of the two filling phases and the global one evaluated by mean of equation 6.10 are reported. Moving from 100 g/s to 130 g/s, their values are between 55% and 65 % with no direct dependence on $\dot{m}_{wf}$.

Considering an average value of $\eta_{vol_{main}}$ and $\eta_{vol_{dualint}}$ and the linear fitting between k values and $\dot{m}_{wf}$, it is possible to evaluate the expander

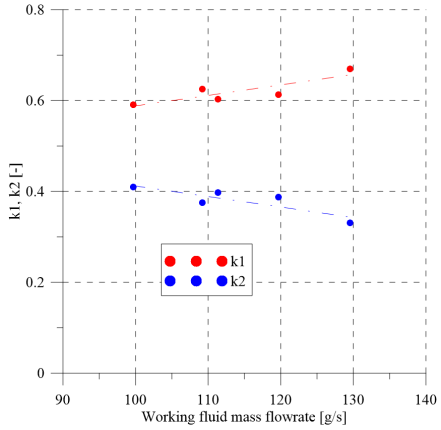

Figure 6.4: Experimental values of k_1 and k_1.

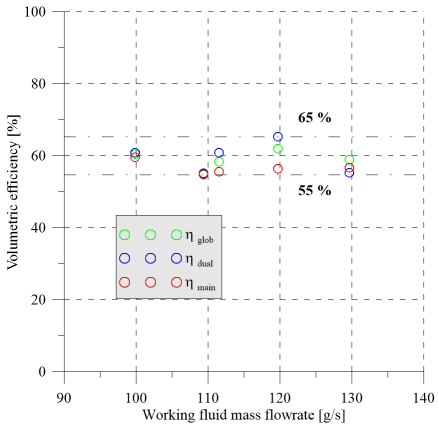

Figure 6.5: Volumetric efficiency of the two filling phases in the DIP expander.

inlet pressure at different flowrates with satisfying accuracy. The results of this procedure is reported in figure 6.6.

The simplified model determines a linear relationship between the expander inlet pressure and the working fluid mass flowrate slightly underestimated at low $\dot{m}_{wf}$. However deviations with experimental data are below 8%. In the same figures, also the trend described by the same same model with further assumptions has been reported. Indeed, the red line in figure 6.6(a) describes the trend obtained considering average values of k_1 and k_2 neglecting the influence of mass flowrate reported in figure 6.4. In this latter case, deviations are greater reaching values up to 10%. This result confirms the importance of the correct representation of the mass flowing through the admission pipes to correctly predict the inlet pressure at the expander inlet. Even a slight variation can produce greater modifications in the permeability of the device.

6.5 Preliminary design of a downsized expander

A preliminary evaluation of the dual intake volume necessary to guarantee the same intake pressure between a dual port and a single port expander can be done comparing equation 6.5 and 6.8. When all the other quantities are the same, parameters can be simplified leading to the following equation:

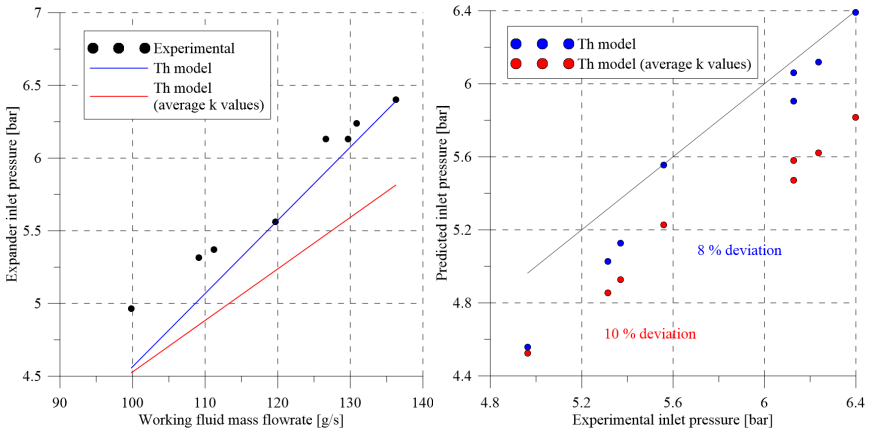

(a) (b)

Figure 6.6: Results of the theoretical analysis (a) inlet pressure vs flowrate (b) predicted vs experimental pressure data.

$$\frac{V_{dualint,end}}{V_{mainint,end}} = \frac{\eta vol_{main} k_1 + \eta vol_{dualint} k_2}{\eta vol} = \frac{\eta vol_{glob}}{\eta vol} \tag{6.11}$$

which states that in order to have the same inlet pressure, the ratio between the dual intake volume and the main one of the single port device has to equal the ratio between their related volumetric efficiency.

In the real machine, the volume ratio is 2.8. Indeed, the dual intake volume is 15.2 cm^2 against the 5.4 cm^2 of the main intake end. On the other hand, the ratio between the experimental volumetric efficiency stands at 1.39 (42 % vs 58%). For this reason, the indicated cycles shown in previous sections (fig. 6.2) evaluated at the same $\dot{m}_{wf}$ exhibits different inlet pressures. In order to ensure the same operating point, the volume at the dual intake end has to be 7.5 cm^2 which is approximately half of the value in the experimented expander. In this way a 50% reduction of the expander size, weight and volume can be achieved with obvious advantages in many applications. Making reference to the transport sector, on board applications are severely limited by space availability. Moreover, reduced weight determines lower fuel consumption, which ultimately reduces the impact on engine performances.

The intake volume reduction can be fulfilled acting on the axial length of the expander or reducing the eccentricity between rotor and stator. In order to understand the best design solution a dedicated analysis has been conducted. The aim has been the minimization of friction losses which represent

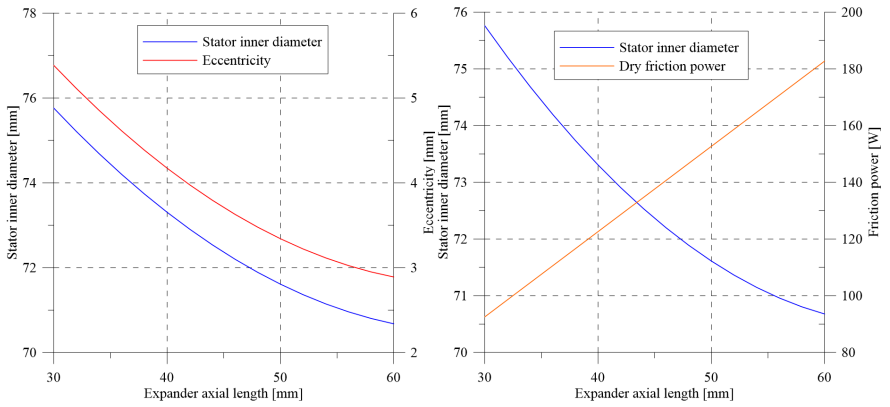

(a) (b)

Figure 6.7: Geometric constrains of the expander (a) and dry friction vs expander axial length relation (b).

a crucial parameter affecting the overall performances of the expander. As seen, the most important contribution to friction losses is related to the dry friction between the blade tip and the stator inner surfaces. Other sources of mechanical losses are negligible and contribute for less than 1%.

From this consideration a simplified model has been used to evaluate such losses at different expander geometries. The rotor diameter has been fixed at the original value of 65 mm. To guarantee a fixed dual intake volume, when the axial length decreases the stator diameter must increase. Being the eccentricity defined as the difference between stator and rotor radius, it must increase as well for a fixed rotor diameter (figure 6.7a).

The geometry of the expander has been reconstructed by means of few equations. First, θ_1 and θ_2, representing the angles between the reference axis and each of the blade constituting the vane, are defined:

$$\begin{aligned} \theta_1 &= \theta - \frac{1}{2}\left(\frac{2\pi}{N_v}\right) \\ \theta_2 &= \theta + \frac{1}{2}\left(\frac{2\pi}{N_v}\right) \end{aligned} \tag{6.12}$$

where θ is the angle between the bisector of the vane and the reference axis and N_v the number of the vanes. Then, the distance between the rotor center and the two points of contact of the blade tips with the stator are

defined as:

$$\begin{aligned} r_1(\theta) &= -ecc\ \cos\theta_1 + \sqrt{r_{stator}^2 + ecc^2(\cos^2\theta_1 - 1)} \\ r_2(\theta) &= -ecc\ \cos\theta_2 + \sqrt{r_{stator}^2 + ecc^2(\cos^2\theta_2 - 1)} \end{aligned} \tag{6.13}$$

where ecc represents the eccentricity between stator and rotor. Once known r1 and r2, the evolution of the chamber volume can be evaluated for each angle θ as :

$$V(\theta) = \Big((r_1 r_2 \frac{\sin(2\pi/N_v)}{2}) - \frac{\pi r_{rotor}^2}{N_v} + r_{stator}^2(\theta_c - \cos\theta_c \sin\theta_c) - \frac{Tk_b}{2}(r_1 + r_2 - 2r_{rotor})\Big)W_{exp} \tag{6.14}$$

In the equation a different angle, namely θ_c, compares. It represents the analogue of θ_1 and θ_2 but it is referred to the stator center. It can be evaluated as follows:

$$\begin{aligned} \theta_1'(\theta) &= \theta_1 - \sin^{-1}\left(\frac{ecc\ \sin\theta_1}{r_{stator}}\right) \\ \theta_2'(\theta) &= \theta_2 - \sin^{-1}\left(\frac{ecc\ \sin\theta_2}{r_{stator}}\right) \\ \theta_c &= \frac{\theta_2' - \theta_1'}{2} \end{aligned} \tag{6.15}$$

Figure 6.7b reports the trend described by the dry friction power when the expander axial length varies. Friction losses are proportional to the normal force acting on the bottom of the vane which depends on centrifugal and pressure forces. Both are affected by a different size of the expander. When the axial length decreases, also the blade reduces its longitudinal dimension and mass, decreasing the centrifugal force. Moreover, if the blade is shorter, the surface in which the rotor pressure is exerted is lower, lowering the hydrostatic force. As a consequence, the reduction of the axial length decreases the friction losses almost linearly.

The pressure under the blade depends primary on the vane pressure. In addition, its value is influenced by the gaps between the blades and the rotor slot and the dynamic phenomena occurring during the rotation of the expander. For these reasons it is hardly predictable through a simplified analysis and it has been assumed as half of the intake pressure in figure 6.7b.

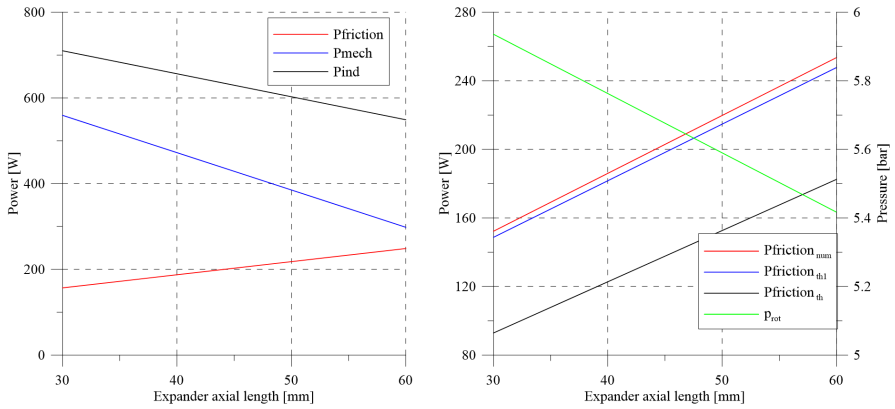

Figure 6.8: Influence of expander axial length on performances (a) and friction power (b).

A more in depth analysis on the same parameter conducted by means of the GT-Suite model revealed that this assumption greatly underestimates power losses despite capturing the general trend with the expander axial length (figure 6.8b). In the same figure, the average rotor pressure is represented. It is worth noting how, despite the reduction of p_{rot}, the friction losses are higher when the axial length is higher, meaning that the increased surface of the blades bottom has a much larger influence on the normal force acting on the stator. As a result mechanical power is highest at the lowest investigated value. The variation of p_{rot} is determined by the different geometry of the expander. When the axial length W is reduced indeed, not only the dual intake volume is affected but also the exhaust one. In addition, the varied eccentricity produces slight modifications in the built in ratio of the expander and on leakage flows which play an important role in the definition of the chamber pressure as seen in the previous chapter.

6.6 Numerical comparison

The previous analysis showed that the axial length of the expander has to be reduced to maximize the benefits of the dual intake system on mechanical performances. In this way it is possible to lower centrifugal and hydrostatic forces which ultimately contribute to the increase of dry friction phenomena. The analysis has been carried out varying the axial length W of the expander

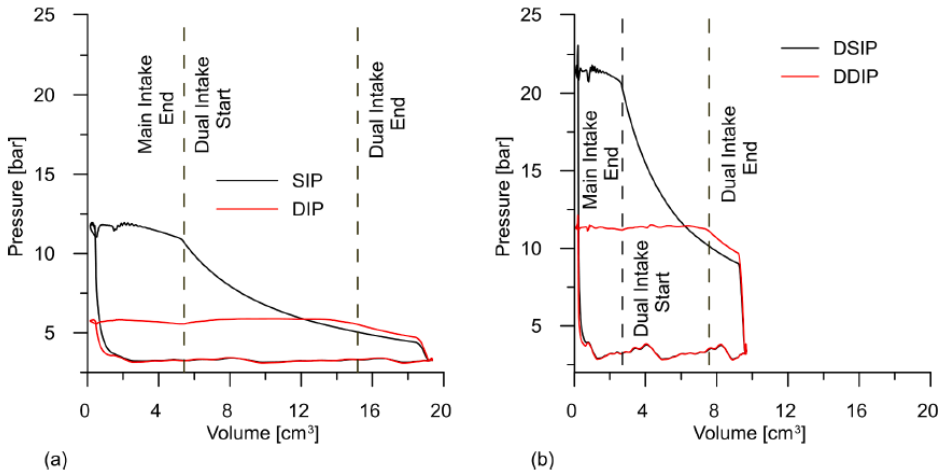

Figure 6.9: Numerical indicated cycle comparison between SIP and DIP expander (a) and DSIP and DDIP expander (b)

from the original value of 60 mm down to 30 mm. At this latter value it corresponds a stator diameter equal to the one of the single intake machine. Further reduction of W involves an increase of the stator size higher than that of the SIP device. For this reason the axial length has been fixed at 30 mm resulting in a stator diameter of 75.9 mm, equal to the OEM expander.

The analysis on the downsized dual intake port expander (DDIP) has been further carried on comparing its performance to the one obtained by the single and dual intake. Moreover, a downsized version of the single intake expander (DSIP) has been added to the analysis.This last version represents a single intake expander with the same geometrical features of the DDIP with the exception of the dual port. All the evaluations have been conducted by mean of the numerical model built in GT-Suite. Clearances and dry friction coefficient have been fixed at the same values in all the cases as reported in table 6.5.

Figure 6.9 reports the indicated cycles obtained with the different expanders for the same boundary conditions. The working fluid mass flowrate has been fixed at 130 g/s with a superheating degree of 10 °C. The inlet pressure represents a result of the numerical model based on dynamic evaluations on the permeability of the machines. Outlet pressure is fixed at 3.2 bar.

In figure 6.9a DIP and SIP devices are compared. The closed area described by the DIP expander is much lower than the SIP. Intake pressure is

greatly reduced due to the higher intake volume which does not allow the pressure to increase. The downsized versions are represented in figure 6.9b. The exhaust volume, identified by the sudden isochoric expansion, is half the one observed in the previous case because of the reduced axial length of the expander. Similar considerations can be done with the SIP version achieving higher intake pressure and a higher closed area representing the indicated work of the expander.

The performances of the expanders at the operating conditions of figure 6.9 are reported in detail in table 6.5. The SIP is able to guarantee an intake pressure almost double than the DIP with 10.7 bar against 5.5 bar. This aspect is reflected also in the indicated and mechanical power which are much greater in the SIP case. P_{ind} of the single intake expander is 1432 W while being 50% lower in the DIP case. This trend influences also the mechanical efficiency. Despite friction losses are lower in DIP, the mechanical efficiency is higher in the SIP case because of the great disparity in the indicated power output of the expanders. Lower friction losses are caused by the decreased chamber pressure in the DIP case as thoroughly explained in previous sections.

The large power difference is reduced when the downsizing of the expander is considered. The DDIP expander indicated power stands at 1276 W which is abut 10% lower than the SIP case. The relative difference moves down to 8% when the mechanical power is considered. In the DDIP expander in fact, the reduced axial length determines a lower centrifugal force which decreases the friction losses from 90 W to 46 W. As a result, the mechanical efficiency is quite higher (96% vs 94%). Compared to the DIP case this increase is much more evident, given the higher indicated power which also contributes to the increase of η_{mech}. Indicated and overall efficiencies are comparable between the DDIP and the SIP cases despite the first having a superior η_{vol}. Main cause of this effect is related to the larger isochoric expansion which takes place (figure 6.9b).

When the downsizing is considered for the single intake option the primary effect is an increased pressure at the expander inlet which reaches 20.3 bar for the same flowrate of 130 g/s. The increase is caused by the reduction of the intake end volume according to equation 6.5. The higher pressure ratio and isentropic power determine a higher indicated and mechanical power output compared to all other cases. The power losses due to friction are higher

	SIP	**DIP**	**DSIP**	**DDIP**
Clearance between vane tip and Stator [μm]	85	85	85	85
Clearance between blade tip and Stator [μm]	10	10	10	10
Clearance between rotor face and slot [mm]	0,2	0,2	0,2	0,2
Friction Coefficient at tip blade	0,01	0,01	0,01	0,01
Intake pressure p_{in} (at intake manifold) [bar]	12,7	5,9	21,9	11,4
Intake end pressure $p_{int,end}$ [bar]	10,7	5,5	20,3	11,1
Intake temperature [°C]	88,8	60,1	111,5	86,2
Average outlet pressure [bar]	3,2	3,2	3,2	3,2
Elaborated mass flow rate $\dot{m}_{wf}$ [g/s]	130	130	130	130
Mechanical power P_{mech} [W]	1342	680	1817	1230
Power loss P_{loss} [W]	90	80	60	46
Indicated Power P_{ind} [W]	1432	760	1877	1276
Global efficiency η_{global} [%]	47	55	47	46
Mechanical Efficiency η_{mech} [%]	94	90	97	96
Volumetric Efficiency η_{vol} [%]	51	72	56	75
Indicated Efficiency η_{ind} [%]	50	61	49	48

Table 6.5: Performances comparison between SIP, DIP, DSIP and DDIP expanders.

than the DDIP case. Despite having the same dimension, which eventually leads to the same centrifugal force acting on the blade, the higher chamber pressure increases the hydrostatic force on the blade bottom. Nonetheless, the higher indicated power (1877 W) allows to ensure a higher mechanical efficiency.

The greater performances of the DSIP with respect to other options were expected. The lower intake end volume, together with the absence of a second fluid intake ensures better thermodynamic conditions at the expander inlet which consequently increase the theoretical power that can be converted into useful work. However, the dual intake system has been initially thought to reduce the maximum pressure of the plant. In the DSIP case, the expander inlet pressure increases up to 20.3 bar. In this condition, the recovered thermal power is about 24 kW considering a working fluid entering the evaporator of the ORC-based unit at 30 °C. When the thermal load is higher, an increase of the mass flowrate is needed which eventually involves a further increase of the maximum pressure of the plant. This issue is of great importance in the manufacturing of components. When the pressure increases, both the evaporator and the expander have to withstand higher

pressure forces which determine an increase of weight and size. Sealing systems can be compromised. In addition, evaporation temperature increases with p_{in}, reducing the temperature difference at the evaporator between the working fluid and the hot source making it more difficult to exchange thermal power. For all these reasons, despite showing lower energetic performances, the DDIP ensures a better reliability of the machine which results in a much easier operation of the plant.

A complete analysis on the normal force acting of the blades is shown in figure 6.10. The most important factor is represented by the pressure exerted on the blade bottom. Figure 6.10a reports the trend against the working fluid mass flowrate. In all the cases the pressure inside the slots increases with flowrate due to the higher p_in which increases the chamber pressure. This phenomenon is much more visible in the DSIP case where the rotor pressure varies from 10 bar to 18 bar for $\dot{m}_w f$ moving from 100 g/s to 200 g/s in a quadratic way. On the other hand, SIP and DSIP show lower values in the same range of investigation. Maximum pressure reached by the DSIP is around 11 bar at 200 g/s down to a pressure slightly above 8 bar for the minimum value of flowrate. The trend characterizing the SIP expander is somewhat below that of the DSIP mainly because of the slight different inlet pressures reported in figure 6.9 and table 6.5. On the other hand, the DIP device shows the lowest values of p_{rot} due to its higher permeability as shown previously.

Figure 6.10b represents the trend of the hydrostatic force resulting from the pressure values previously discussed. It is proportional to the surface in which the pressure is acting. Indeed, hydrostatic force can be evaluated as:

$$F_p = p_{rot} T k_b W_b \tag{6.16}$$

where Tk_b and W_b represent the thickness of the blade and the dimension along the axis of the expander. This latter parameter is reduced in the downsized versions of the expander, both in the SIP and in the DIP case. For this reason, the trend observed for p_{rot} is partially overturned because of the influence of the blade geometry. Indeed, the blade geometry has a much larger contribution to the pressure force with respect to the rotor pressure itself. Lowest values are achieved by the DDIP which combines moderate rotor pressure to reduced blade length. On the other hand, dual

and single port expander without downsizing exhibit the highest pressure force. For $\dot{m}_{[}wf]$ equal to 100 g/s, the pressure force (F_p) is 158 N and 169 N respectively, which is almost double than the downsized counterparts. The DSIP expander show values of F_p greater than DDIP but lower than the DIP up to 175 g/s. For greater $\dot{m}_{wf}$, pressure inside the slots of the rotor increases too much and nullifies the effects of the reduced dimensions of the blades leading to a pressure force higher than the original case reaching 200 N at 200 g/s.

The effect of the blade mass is also visible in figure 6.10c which represents the centrifugal force. This quantity can be evaluated as:

$$F_c = m_b n^2 (r_1 - \frac{L_b}{2}) \tag{6.17}$$

where m_b is the blade mass, r_1 the distance between the rotor center and the blade tip and L_b half the length of the blade to take into account the position of its center of gravity. From the equation it is straightforward to understand that the centrifugal force in the downsized version is half compared to the original expander because of the reduced blade mass. In the first case it stands at 12 N against 24 N in the SIP and DIP option. It is worth noting that the centrifugal force value is approximately one order of magnitude lower than the hydrostatic one. This aspect determines a normal force trend in all cases which reflects the same behaviour of F_p. Highest values are obtained in the SIP case over the whole range of investigation moving from 192 N to 234 N for $\dot{m}_{wf}$ ranging between 100 g/s and 200 g/s. In the same interval, the DDIP version exhibits 50% lower normal forces which vary between 96 N to 131 N.

6.7 Conclusions

In this chapter a novel design methodology for sliding vane rotary expanders has been presented. Starting from experimental data collected on a ORC-based recovery unit equipped with a siding vane expander in single and dual port configuration, a virtual software platform has been developed. Through the validation of the numerical model, a comprehensive knowledge of the dynamic phenomena occurring inside the chamber which affect the volumetric and energetic performances of the expander in both configurations has been reached.

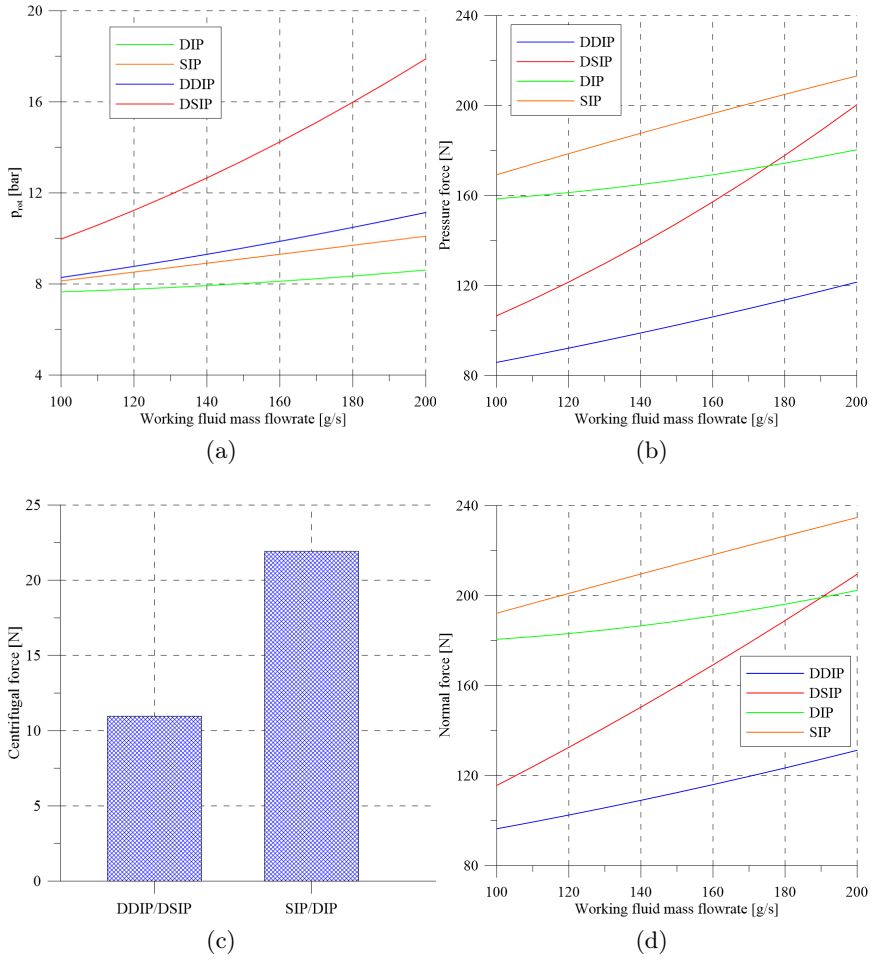

Figure 6.10: Analysis of normal forces acting on the blades: rotor pressure (a), hydrostatic force (b), centrifugal force (c) and normal force (d).

The understanding of these phenomena allowed to define a novel design methodology. Experimental and numerical results showed that the dual port option can guarantee lower chamber pressures with respect to a traditional device at the expense of a lower produced mechanical power. This aspect could be beneficial in several applications where it is not possible to exceed certain pressure limits. At the same time, an increase of the recovered thermal energy is achievable increasing the mass flowrate without determining an expander inlet pressure too high. However, the possibility to downsize the expander has been investigated to reduce the mechanical power output gap with the single intake expander.

Preliminary theoretical considerations showed that to ensure the same performances of a SIP expander, a 50% reduction of the dual intake end volume compared to the experimented machine is necessary. This volume reduction can be obtained decreasing the axial length of the expander with consequent benefits on the mechanical performances. The reduced dimensions indeed, help lowering the friction forces due to the dry contact between the blade tip and the stator surface. Numerical results indicated that the downsized version of the expander, with the auxiliary intake, can guarantee higher mechanical performances (96% vs 94%) and a higher volumetric efficiency (75% vs 51%) at the expense of a slight reduction of the power output (-8%). On the other hand, with a newly conceived dual port expander a sensible reduction of size, volume and consequently weight of the device is achieved. In addition, the analysis on the normal force acting on the blades showed that the DDIP is characterized by half the force acting on a traditional single intake expander which can potentially reduce also vibration and wear phenomena on the blade.

In conclusion, the study on the dual port design demonstrated that this system is a viable solution to improve the ease of operation of the ORC-based power unit and the reliability of the expansion device allowing to recover a comparable power compared to the single intake machine at the same operating conditions.

Chapter 7

Conclusions

In this thesis the issues related to the thermal energy recovery in Internal Combustion Engine have been treated. Initially, the challenges related to global warming have been described, analysing the primary energy demand evolution and shares and the related global CO_2 emissions. In this context, the transport sector is one of the major sources of atmospheric CO_2. It is responsible for 20 % of the world primary energy demand and approximately 12 % of worldwide greenhouse gases emissions. Lots of efforts have been made through national and international policies which set more and more stringent limits regarding specific emission on type approval cycles. These measures eventually lead to an overall increase of the efficiencies of newly registered vehicles by means of the adoption of several innovations. However, further improvements can be made. Among the available different technologies Waste Heat Recovery appears a promising solution. In particular, among the different bottoming cycles which can be used to recover part of the waste heat, Organic Rankine Cycles offer good potential in terms of thermodynamic efficiency and good flexibility having a further degree of freedom consisting in the working fluid which can be chosen in order to match the necessity of the specific applications. A thorough analysis of the available research studies on this matter has been conducted, focused on working fluid selection criteria, plant layout configurations and component level analysis. Regarding this matter, a particular focus has been given to the expander technology. The improvement of the efficiency of the expanders is of primary importance in order to increase the performances of ORC-based units, especially in the kW scale power output range. At the same time, this ma-

chine has to guarantee reliability and ease of operation, particularly in Waste Heat Recovery applications in internal combustion engines.

Sliding vane volumetric expanders represent a good compromise between efficiency and ease of operation. Main advantages are constituted by their easy manufacturing and simple geometry which ensure an easy lubrication and good performances in off-design conditions. This kind of machine has been tested in the laboratory of fluid machines of the University of L'Aquila. Main characteristics of the expander are an intake volume of 5.4 cm^3 and a built in volume ratio of 3.4. The expander has been integrated in an ORC-based power unit for the recovery of the exhaust gases of a 3 liter turbocharged Diesel Engine commonly used in light and heavy duty vehicles. Besides the sliding vane expander, the ORC-based unit was composed of a plate and fins evaporator, a plate heat exchanger as a condenser and a gerotor pump. A tank upstream the pump has been placed to stabilize the mass flowrate and guarantee a hydraulic head at the pump inlet to avoid cavitation phenomena. Temperature and pressure transducers have been placed downstream and upstream each component. Moreover, a set of three piezoresistive pressure transducers have been inserted on the stator cover to measure the pressure inside the vane and reconstruct the indicated cycle through a dedicated post-processing sub-routine. The evaluation of the indicated cycle allowed the definition of mechanical and indicated efficiencies.

Several experimental campaigns have been conducted on the experimental test bench varying the conditions of the hot source, setting the operating regime of the engine, and the elaborated mass flowrate of the ORC-based unit. In this way, it has been possible to assess the performances of the expander at different inlet pressure and superheating degree. The results of the first experiments showed that superheating degree has a negligible influence on the volumetric performances which ranged between 58 % and 62%. Lowest values have been found at higher inlet pressures. Regarding this aspect, an important correlation has been found between working fluid mass flowrate and the inlet pressure of the expander. The relation is linear, with inlet pressure increasing from 6.8 bar to 11 bar for mass flowrate ranging from 70 g/s to 130 g/s. The analysis of the indicated cycle showed a relative maximum of the indicated efficiency, which peaked at 49% for $\dot{m}_{wf}$ equal to 110 g/s. This is justified by under and over expansion losses in off-design conditions. Global efficiencies follow the same trend being obviously

decreased because of the mechanical losses. Maximum values reached 40 % at the same flowrate conditions with a mechanical efficiency of 85%.

After the conclusion of this first experimental campaign, the original device has been modified. A second port, positioned right after the closure on the main one, has been opened on the stator. The aim of this modification was to define an auxiliary injection to contrast the pressure decrease during the expansion phase of the expander. In this way strong modifications on the hydraulic resistance of the device and on the specific trend of the indicated cycles are determined. In particular, the modification allowed to elaborate a greater flowrate without increasing the inlet pressure of the expander which could reduce the reliability and safety of the device. Experimental data confirmed theoretical expectations. The maximum expander inlet pressure at the highest value of the flowrate investigation range (130 g/s) reached 7 bar, with a decrease compared to the Single Intake Port (SIP) expander of 50 %. On the other hand, volumetric efficiency increased from 60 % to an average of 85 % with the auxiliary intake because of lower fluid-dynamic losses associated to the reduced pressure inside the vanes. The comparison between the indicated cycles at the same flowrate showed that the higher pressure in the end of the expansion does not balance the lower inlet pressure of the dual intake expander, thus determining a lower indicated power (P_{ind}). On the other hand, when the same comparison is made at constant inlet pressure, the indicated cycle on the p-V diagram describes a higher closed area determining a greater power. The trend of P_{ind} at different working fluid mass flowrates are partially overlapped in the two cases, with the Dual intake option (DIP) reaching higher values at lower pressures. However, mechanical power output is slightly lower in the DIP case because of the lower mechanical efficiency experimentally found . This issue was found also between two consecutive experimental campaigns on the single intake machine. A thorough inspection of the device allowed to attribute this difference on wear phenomena on the blade tip due to the dry friction with the stator inner surface. This eventually contributed to the reduction of mechanical and volumetric performances. Overall efficiencies have been influenced by this phenomenon with maximum values of 32 % and 30 % for the SIP and DIP case respectively, despite the higher indicated efficiency of the dual intake expander (46% vs 41 %).

The collected experimental data have been used to build and calibrate

a numerical model on GT-Suite software platform. The software platform allows the representation of fluid-dynamic phenomena in a 1D way. Filling and emptying processes are evaluated solving the Navier Stokes equations together with energy and mass conservation equations. On the other hand, the processes happening inside the chamber volume during the expansion phase are evaluated through a 0D modelling approach, using several libraries of equations which are capable to describe the dynamic phenomena occurring in the revolving vane. The model has been built to account also for the calculation of leakage losses. Three different leakage paths have been identified. The one occurring at the blade tip between adjacent vanes, the one occurring through the rotor slots, which also produces a flowrate from a vane to the previous one (according to the direction of rotation), and the one in the stator cover, whose main effect is to put in communication the intake with the exhaust. Clearance gaps for the three kinds of paths have been chosen as calibration parameters. Validation quantities are mass flowrate and indicated power. After that, the calibration of the friction coefficient between blade tip and stator is necessary for the evaluation of the mechanical power and friction losses. Results of the calibration procedure done on the single intake machine showed maximum deviations of 9.2 %, 9.9 % and 7.7% for mass flowrate, indicated and mechanical power respectively. One first conclusion could be made from this analysis. The calibration procedure led to different results depending on the state of the expander. In other words, the results obtained for the machine after it encountered lower mechanical and volumetric efficiencies showed a sensible increase of the clearance gap between vane tip and stator. This result confirmed that clearance gaps have a great influence on the expander performances. Moreover, it is shown that the most significant losses are the one related to the clearance gaps between blade tip and stator. An in depth analysis on the indicated cycles showed that, despite having a detrimental effect on the expander inlet pressure, the presence of such flow losses allows a partial recovery during the expansion phase. p-V diagrams associated with a lower volumetric efficiency are characterized by a higher pressure during the expansion phase with respect to an adiabatic isentropic transformation. This is obtained through a higher mass flowrate needed for the achievement of a certain pressure, at the expense of the machine efficiency. The causes of this behaviour are the pressure differences which exist between adjacent vanes during a certain angular period.

The evolution of the mass inside the vane during the cycle demonstrates that when high clearances exist, mass flowrate keep entering the vane also after the end of the intake phase consequently determining the aforementioned pressure increase. The adoption of an auxiliary port strongly affects also this phenomenon, lowering the pressure difference and the angular period in which it is exerted between the vanes. A sensitivity analysis has been conducted varying the angle of the dual intake port in order to define the best angular position. The results showed that the best position strongly varies depending on the objective function. If the power output has to be maximized the best position is near the exhaust, at 57.7 ° after the end of the main one. In this case the volumetric and mechanical efficiency increases are 6% and 9% respectively. The mechanical power output increases from the reference value of 844 W to 1917 W is the working fluid mass flowrate goes from 132 g/s to 279 g/s. On the other hand, if the aim is to reach maximum efficiency, the second port positioning translates near the end of the main one causing an overlapping between the two filling phases. Indeed, when the angular distance between the end of the main and the start of the auxiliary intake is equal to 22.4 ° a 28 % increase of the volumetric efficiency is achievable. At the same time, mechanical power output increases to 1674W with a mass flowrate increase of 50% compared to the reference value.

The conducted analyses showed that the dual intake expander is able to guarantee higher performances compared to the original device (OEM), in particular when the intake pressure is fixed at the same value. However, in order to close the gap also at the same mass flowrate, the numerical software platform has been used as a design tool. Preliminary theoretical considerations, based on the analysis of the volumetric efficiency, showed that in order to guarantee the same inlet conditions when the mass flowrate is the same a downsize on the volume is necessary. Based on the experimental data it has been found that the dual intake end volume has to decrease to 50% of the original value. This downsize can be achieved reducing the axial length of the expander or the stator inner diameter. Through the evaluation of the mechanical efficiency it has been found that the reduction of the axial length could allow he decrease of friction phenomena occurring between the blade tip and the stator inner surface. For this reason, the considered downsized version of the expander with a dual intake port had the same stator diameter of the original device. The geometry has been imported into the

software platform and the machine has been compared to the OEM device at the same clearance gaps and the same elaborated flowrate. Indicated power output differs by 11% with the SIP device achieving 1432 W against 1276 W of the downsized version (DDIP). This difference is reduced to 9% when the mechanical power is considered because of the lower friction losses associated with the DDIP machine. In order to make a fair comparison, a downsized version of the single intake expander has been also considered. In this case, a greater mechanical and indicated power can be achieved at the expense of an inlet pressure which is far higher than the previous cases. In fact, the inlet pressure increases up to 21 bar against 11 bar reached in the SIP and downsized DIP expander. The increase of the inlet pressure can be dangerous for the reliability of the plant. Moreover, the higher average temperature in the upper part of the Rankine cycle could potentially decrease the efficiency of the evaporator because of the reduced temperature difference. The downsized version, on the other hand, is able to produce a comparable mechanical power with respect to the original device with the additional benefit of having reduced size, volume and weight which are characteristics greatly important in non stationary applications as the one related to the recovery of waste heat in internal combustion engines.

In conclusion, this thesis allowed to assess the performances of sliding vane expanders in a wide range of operating conditions. The performances and the advantages of a novel technology consisting in an additional intake port have been studied and reported with numerical analyses and experimental data. The numerical and theoretical analyses allowed also the evaluation of the main sources of loss which eventually made possible the definition of new design criteria. In particular, the dual port option made possible a sensible downsize of the device with comparable performances in terms of mechanical and indicated power output. In the future, further experimental tests will be conducted to assess the performances of the machine also at different rotational speed with the aim to define a suitable control strategy when the conditions of the hot source strongly varies as it happens in internal combustion engine applications.

Appendices

Appendix A

Nomenclature

Symbols

A	cross sectional area
β	Built in volume ratio
Cd	Discharge coefficient
Cf	Fanning coefficient
D	Diameter
δ	clearance gap
$\Delta\theta$	Angular Amplitude
e	eccentricity
e	specific internal energy
ecc	eccentricity
η	efficiency
fs	full scale
fs	force
h	heat transfer coefficient
Kp	pressure loss coefficient
m	mass flowrate
M	Mass
μ	dynamic viscosity
Nv	Vane number
p	pressure
P	power
Φ	angle
R	Specific Gas Constant
R	Radius
ρ	density
S	entropy
T	temperature
Texp	Expander Torque
Tk	Thickness
u	velocity vector
V	Volume
W	Width
Z	Compressibility factor

Subscripts

ad	adiabatic
b	blade
c	centrifugal
cw	cold water
el	electric
f,v	viscous friction
id	ideal
in	inlet
ind	indicated
int	intake
is	isentropic
mech	mechanical
out	outlet
p	pressure
rot	rotor
stat	stator
v	vane
vol	volumetric
wf	working fluid

Acronyms

BAU	Business As Usual
BECCS	Bio-Energy with Carbon Capure and Storage
CHP	Combined Heat and Power
DDIP	Downsized Dual Intake Port
DIP	Dual Intake Port
DSIP	Downsized Single Intake Port
ECU	Electronic Control Unit
EFT	Enhanced Transparency Network
EG	Exhuast Gases
EGR	Exhaust Gases Recirculation
GDP	Gross Domestic Product
GHG	Greenhouse Gases
GWP	Global Warming Potential
HDDE	Heavy Duty Diesel Engine
HDV	Heavy Duty Vehicle
HT	High Temperature
HX	Heat Exchanger
ICE	Internal Combustion Engine
IPCC	Intergovernmental Panel on Climate Change
LDV	Light Duty Vehicle
LT	Low Temperature
LT-EDS	Long term emission development strategies
NDC	Nationally Determined Contribution
NEDC	New European Driving Cycle
ODP	Ozone Depletion Potential
ORC	Organic Rankine Cycle
P&F	Plate and Fins
PHX	Plate Heat Exchanger
RMSE	Root Mean Square Error
RVE	Revolving Vane Expander
S&T	Shell and Tubes
SIP	Single Intake Port
SSE	Single Screw Expander
SVRE	Sliding Vane Rotary Expander
TFC	Trilateral Flash Cycle
UNFCC	United Nations Framework on Climate Change
WHR	Waste Heat Recovery
WLTP	Worldwide harmonized Light vehicles Test Procedure

Bibliography

[1] Dieter Lüthi et al. "High-resolution carbon dioxide concentration record 650,000–800,000years before present". In: *Nature* 453.7193 (2008), pp. 379–382. ISSN: 1476-4687. DOI: 10.1038/nature06949. URL: https://doi.org/10.1038/nature06949.

[2] Karin Van Der Wiel et al. "Rapid attribution of the August 2016 flood-inducing extreme precipitation in south Louisiana to climate change". In: *Hydrology and Earth System Sciences* 21.2 (2017), pp. 897–921. ISSN: 16077938. DOI: 10.5194/hess-21-897-2017.

[3] Tom K. R. Matthews, Robert L. Wilby, and Conor Murphy. "Communicating the deadly consequences of global warming for human heat stress". In: *Proceedings of the National Academy of Sciences* 114.15 (2017), pp. 3861–3866. ISSN: 0027-8424. DOI: 10.1073/pnas.1617526114. eprint: https://www.pnas.org/content/114/15/3861.full.pdf. URL: https://www.pnas.org/content/114/15/3861.

[4] I. Masood et al. "The deadly heat wave of Pakistan, June 2015". In: *International Journal of Occupational and Environmental Medicine* 6.4 (2015), pp. 247–248. ISSN: 20086814. DOI: 10.15171/ijoem.2015.672.

[5] Asaf Bernstein, Matthew T. Gustafson, and Ryan Lewis. "Disaster on the horizon: The price effect of sea level rise". In: *Journal of Financial Economics* 134.2 (2019), pp. 253–272. ISSN: 0304405X. DOI: 10.1016/j.jfineco.2019.03.013. URL: https://doi.org/10.1016/j.jfineco.2019.03.013.

[6] Felix Creutzig et al. "Beyond Technology: Demand-Side Solutions for Climate Change Mitigation". In: *Annual Review of Environment*

and Resources 41.1 (2016), pp. 173–198. DOI: 10.1146/annurev-environ-110615-085428. eprint: https://doi.org/10.1146/annurev-environ-110615-085428. URL: https://doi.org/10.1146/annurev-environ-110615-085428.

[7] Smil Vaclav. *Energy Transitions: Global and National Perspectives*. Praeger, 2016.

[8] M. Gloor, J. L. Sarmiento, and N. Gruber. "What can be learned about carbon cycle climate feedbacks from the CO 2 airborne fraction?" In: *Atmospheric Chemistry and Physics* 10.16 (2010), pp. 7739–7751. ISSN: 16807316. DOI: 10.5194/acp-10-7739-2010.

[9] European Commission. "Regulation (EU) N. 443/2009 OF THE EUROPEAN PARLIAMENT AND OF THE COUNCIL". In: *Official Journal of the European Union* (2009). URL: https://eur-lex.europa.eu/legal-content/EN/TXT/HTML/?uri=CELEX:32009R0443&from=EN.

[10] European Commission. "Regulation (EU) N. 510/2011 OF THE EUROPEAN PARLIAMENT AND OF THE COUNCIL". In: *Official Journal of the European Union* (2011). URL: https://eur-lex.europa.eu/legal-content/EN/TXT/?uri=celex%3A32011R0510.

[11] European Commission. "Regulation (EU) 2019/631 OF THE EUROPEAN PARLIAMENT AND OF THE COUNCIL". In: *Official Journal of the European Union* (2019). URL: https://eur-lex.europa.eu/legal-content/EN/TXT/PDF/?uri=CELEX:32019R0631&from=EN.

[12] Fact Sheet Europe. "Market Monitor European Passenger Car Registrations : January – March 2020". In: March (2020), pp. 2–5.

[13] *Monitoring of CO2 emissions from new passenger cars – Regulation (EU) No 2019/631*. 2019. URL: https://www.eea.europa.eu/data-and-maps/indicators/proportion-of-vehicle-fleet-meeting-5/assessment#:~:text=In%20addition%20to%20the%20550,of%20new%20registrations%20in%202019..

[14] José Ramón Serrano, Ricardo Novella, and Pedro Piqueras. "Why the development of internal combustion engines is still necessary to fight against global climate change from the perspective of transportation".

In: *Applied Sciences (Switzerland)* 9.21 (2019). ISSN: 20763417. DOI: 10.3390/app9214597.

[15] European Automobile Manufacturers Association. *The automobile industry pocket guide 20-21*. 2021.

[16] Qinyu Qiao et al. "Comparative Study on Life Cycle CO2 Emissions from the Production of Electric and Conventional Vehicles in China". In: *Energy Procedia* 105 (2017). 8th International Conference on Applied Energy, ICAE2016, 8-11 October 2016, Beijing, China, pp. 3584–3595. ISSN: 1876-6102. DOI: https://doi.org/10.1016/j.egypro.2017.03.827. URL: https://www.sciencedirect.com/science/article/pii/S1876610217309049.

[17] Douglas Broom. *The Dirty secrets of electric vehicles*. Ed. by World Economic Forum. 2019. URL: https://www.weforum.org/agenda/2019/03/the-dirty-secret-of-electric-vehicles.

[18] Amnesty International. "This is what we die for: Human rights abuses in the democratic republic of the congo power the global trade in cobalt". In: (2016), p. 88. URL: https://www.amnesty.org/en/documents/afr62/3183/2016/en.

[19] Nic Lutsey et al. *Efficiency Technology and Cost Assessment for U.S. 2025-2030 Light-Duty Vehicles*. Tech. rep. March. 2017, p. 11.

[20] R. D. Reitz et al. "IJER editorial: The future of the internal combustion engine". In: *International Journal of Engine Research* 21.1 (2020), pp. 3–10. ISSN: 20413149. DOI: 10.1177/1468087419877990.

[21] Gautam Kalghatgi. "Is it really the end of internal combustion engines and petroleum in transport?" In: *Applied Energy* 225.April (2018), pp. 965–974. ISSN: 03062619. DOI: 10.1016/j.apenergy.2018.05.076. URL: https://doi.org/10.1016/j.apenergy.2018.05.076.

[22] Environmental Protection Agency. *The 2019 EPA automotive trends report*. Tech. rep. March. 2020, p. 54. URL: https://nepis.epa.gov/Exe/ZyPDF.cgi?Dockey=P100YVFS.pdf.

[23] Lars Eriksson et al. "Scalable Component-Based Modeling for Optimizing Engines with Supercharging, E-Boost and Turbocompound Concepts". In: *SAE International Journal of Engines* 5.2 (2012), pp. 579–595. ISSN: 19463944. DOI: 10.4271/2012-01-0713.

[24] Youssef Ismail et al. "Study of parallel turbocompounding for small displacement engines". In: *SAE Technical Papers* 2 (2013). ISSN: 26883627. DOI: 10.4271/2013-01-1637.

[25] Habib Aghaali and Hans Erik Ångström. "A review of turbocompounding as a waste heat recovery system for internal combustion engines". In: *Renewable and Sustainable Energy Reviews* 49 (2015), pp. 813–824. ISSN: 18790690. DOI: 10.1016/j.rser.2015.04.144. URL: http://dx.doi.org/10.1016/j.rser.2015.04.144.

[26] L. S. Hewawasam et al. "Waste heat recovery from thermo-electric generators (TEGs)". In: *Energy Reports* 6 (2020), pp. 474–479. ISSN: 23524847. DOI: 10.1016/j.egyr.2019.11.105. URL: https://doi.org/10.1016/j.egyr.2019.11.105.

[27] Nesrine Jaziri et al. "A comprehensive review of Thermoelectric Generators: Technologies and common applications". In: *Energy Reports* 6 (2020), pp. 264–287. ISSN: 23524847. DOI: 10.1016/j.egyr.2019.12.011. URL: https://doi.org/10.1016/j.egyr.2019.12.011.

[28] Ali Elghool et al. "A review on heat sink for thermo-electric power generation: Classifications and parameters affecting performance". In: *Energy Conversion and Management* 134 (2017), pp. 260–277. ISSN: 01968904. DOI: 10.1016/j.enconman.2016.12.046. URL: http://dx.doi.org/10.1016/j.enconman.2016.12.046.

[29] Muhammad Imran et al. "Recent research trends in organic Rankine cycle technology: A bibliometric approach". In: *Renewable and Sustainable Energy Reviews* 81.July 2017 (2018), pp. 552–562. ISSN: 18790690. DOI: 10.1016/j.rser.2017.08.028. URL: http://dx.doi.org/10.1016/j.rser.2017.08.028.

[30] M. Bianchi and A. De Pascale. "Bottoming cycles for electric energy generation: Parametric investigation of available and innovative solutions for the exploitation of low and medium temperature heat sources". In: *Applied Energy* 88.5 (2011), pp. 1500–1509. ISSN: 03062619. DOI: 10.1016/j.apenergy.2010.11.013. URL: http://dx.doi.org/10.1016/j.apenergy.2010.11.013.

[31] Anh Tuan Hoang. "Waste heat recovery from diesel engines based on Organic Rankine Cycle". In: *Applied Energy* 231.June (2018), pp. 138–

166. ISSN: 03062619. DOI: 10.1016/j.apenergy.2018.09.022. URL: https://doi.org/10.1016/j.apenergy.2018.09.022.

[32] Huijuan Chen, D. Yogi Goswami, and Elias K. Stefanakos. "A review of thermodynamic cycles and working fluids for the conversion of low-grade heat". In: *Renewable and Sustainable Energy Reviews* 14.9 (2010), pp. 3059–3067. DOI: 10.1016/j.rser.2010.07.006.

[33] Bo-Tau Liu, Kuo-Hsiang Chien, and Chi-Chuan Wang. "Effect of working fluids on organic Rankine cycle for waste heat recovery". In: *Energy* 29.8 (2004), pp. 1207–1217. ISSN: 0360-5442. DOI: https://doi.org/10.1016/j.energy.2004.01.004. URL: http://www.sciencedirect.com/science/article/pii/S0360544204000179.

[34] Yuanyang Zhao et al. "Expansion devices for organic Rankine cycle (ORC) using in low temperature heat recovery: A review". In: *Energy Conversion and Management* 199.August (2019), p. 111944. ISSN: 01968904. DOI: 10.1016/j.enconman.2019.111944. URL: https://doi.org/10.1016/j.enconman.2019.111944.

[35] Bin Xu et al. "A comprehensive review of organic rankine cycle waste heat recovery systems in heavy-duty diesel engine applications". In: *Renewable and Sustainable Energy Reviews* 107.September 2018 (2019), pp. 145–170. ISSN: 18790690. DOI: 10.1016/j.rser.2019.03.012.

[36] Simone Amicabile, Jeong Ik Lee, and Dongsuk Kum. "A comprehensive design methodology of organic Rankine cycles for the waste heat recovery of automotive heavy-duty diesel engines". In: *Applied Thermal Engineering* 87 (2015), pp. 574–585. ISSN: 13594311. DOI: 10.1016/j.applthermaleng.2015.04.034. URL: http://dx.doi.org/10.1016/j.applthermaleng.2015.04.034.

[37] Cheng Zhang et al. "Thermo-economic comparison of subcritical organic Rankine cycle based on different heat exchanger configurations". In: *Energy* 123 (2017), pp. 728–741. ISSN: 03605442. DOI: 10.1016/j.energy.2017.01.132. URL: http://dx.doi.org/10.1016/j.energy.2017.01.132.

[38] J. Larjola. "Electricity from industrial waste heat using high-speed organic Rankine cycle (ORC)". In: *International Journal of Production Economics* 41.1 (1995). Proceedings of the 12th International Con-

ference on Production Research, pp. 227–235. ISSN: 0925-5273. DOI: https://doi.org/10.1016/0925-5273(94)00098-0. URL: http://www.sciencedirect.com/science/article/pii/0925527394000980.

[39] Vignesh Pethurajan, Suresh Sivan, and Grashin C. Joy. "Issues, comparisons, turbine selections and applications – An overview in organic Rankine cycle". In: *Energy Conversion and Management* 166.March (2018), pp. 474–488. DOI: 10.1016/j.enconman.2018.04.058.

[40] E. H. Wang et al. "Study of working fluid selection of organic Rankine cycle (ORC) for engine waste heat recovery". In: *Energy* 36.5 (2011), pp. 3406–3418. ISSN: 03605442. DOI: 10.1016/j.energy.2011.03.041.

[41] Junjiang Bao and Li Zhao. "A review of working fluid and expander selections for organic Rankine cycle". In: *Renewable and Sustainable Energy Reviews* 24.October 2017 (2013), pp. 325–342. ISSN: 13640321. DOI: 10.1016/j.rser.2013.03.040. URL: http://dx.doi.org/10.1016/j.rser.2013.03.040.

[42] "Montreal Protocol on Substances that Deplete the Ozone Layer Final Act 1987". In: *Journal of Environmental Law* 1.1 (Mar. 1989), pp. 128–136. ISSN: 0952-8873. DOI: 10.1093/jel/1.1.128. eprint: https://academic.oup.com/jel/article-pdf/1/1/128/7286520/1-1-128.pdf. URL: https://doi.org/10.1093/jel/1.1.128.

[43] Maria E. Mondejar and Fredrik Haglind. "The potential of halogenated olefins as working fluids for organic Rankine cycle technology". In: *Journal of Molecular Liquids* 310 (2020). ISSN: 01677322. DOI: 10.1016/j.molliq.2020.112971.

[44] Antti Uusitalo et al. "Thermodynamic evaluation on the effect of working fluid type and fluids critical properties on design and performance of Organic Rankine Cycles". In: *Journal of Cleaner Production* 188 (2018), pp. 253–263. ISSN: 09596526. DOI: 10.1016/j.jclepro.2018.03.228.

[45] Ngoc Anh Lai, Martin Wendland, and Johann Fischer. "Working fluids for high-temperature organic Rankine cycles". In: *Energy* 36.1 (2011), pp. 199–211. ISSN: 0360-5442. DOI: https://doi.org/10.

1016/j.energy.2010.10.051. URL: http://www.sciencedirect.com/science/article/pii/S0360544210006146.

[46] Jinliang Xu and Chao Yu. "Critical temperature criterion for selection of working fluids for subcritical pressure Organic Rankine cycles". In: *Energy* 74 (2014), pp. 719–733. ISSN: 0360-5442. DOI: https://doi.org/10.1016/j.energy.2014.07.038. URL: https://www.sciencedirect.com/science/article/pii/S0360544214008603.

[47] J. Hærvig, K. Sørensen, and T. J. Condra. "Guidelines for optimal selection of working fluid for an organic Rankine cycle in relation to waste heat recovery". In: *Energy* 96 (2016), pp. 592–602. ISSN: 03605442. DOI: 10.1016/j.energy.2015.12.098. URL: http://dx.doi.org/10.1016/j.energy.2015.12.098.

[48] Guibing Chen et al. "Performance prediction and working fluids selection for organic Rankine cycle under reduced temperature". In: *Applied Thermal Engineering* 153.April 2018 (2019), pp. 95–103. ISSN: 13594311. DOI: 10.1016/j.applthermaleng.2019.02.011. URL: https://doi.org/10.1016/j.applthermaleng.2019.02.011.

[49] Zheng Miao et al. "Thermodynamic selection criteria of zeotropic mixtures for subcritical organic Rankine cycle". In: *Energy* 167 (2019), pp. 484–497. ISSN: 03605442. DOI: 10.1016/j.energy.2018.11.002. URL: https://doi.org/10.1016/j.energy.2018.11.002.

[50] Zheng Miao et al. "Selection criteria of zeotropic mixtures for subcritical organic Rankine cycle based on thermodynamic and thermoeconomic analysis". In: *Applied Thermal Engineering* 180 (2020), p. 115837. ISSN: 13594311. DOI: 10.1016/j.applthermaleng.2020.115837. URL: https://doi.org/10.1016/j.applthermaleng.2020.115837.

[51] M. Chys et al. "Potential of zeotropic mixtures as working fluids in organic Rankine cycles". In: *Energy* 44.1 (2012), pp. 623–632. ISSN: 03605442. DOI: 10.1016/j.energy.2012.05.030. URL: http://dx.doi.org/10.1016/j.energy.2012.05.030.

[52] S. Lecompte et al. "Exergy analysis of zeotropic mixtures as working fluids in Organic Rankine Cycles". In: *Energy Conversion and Management* 85 (2014), pp. 727–739. ISSN: 01968904. DOI: 10.1016/j.

enconman.2014.02.028. URL: http://dx.doi.org/10.1016/j.enconman.2014.02.028.

[53] Carlos J. Noriega Sanchez, Louis Gosselin, and Alexandre K. da Silva. "Designed binary mixtures for subcritical organic Rankine cycles based on multiobjective optimization". In: *Energy Conversion and Management* 156.November 2017 (2018), pp. 585–596. ISSN: 01968904. DOI: 10.1016/j.enconman.2017.11.050. URL: https://doi.org/10.1016/j.enconman.2017.11.050.

[54] Hua Tian et al. "Thermo-economic analysis of zeotropic mixtures based on siloxanes for engine waste heat recovery using a dual-loop organic Rankine cycle (DORC)". In: *Energy Conversion and Management* 136 (2017), pp. 11–26. ISSN: 01968904. DOI: 10.1016/j.enconman.2016.12.066. URL: http://dx.doi.org/10.1016/j.enconman.2016.12.066.

[55] D. Di Battista et al. "The Potential of Mixtures of Pure Fluids in ORC-based Power Units fed by Exhaust Gases in Internal Combustion Engines". In: *Energy Procedia* 101.September (2016), pp. 1264–1271. ISSN: 18766102. DOI: 10.1016/j.egypro.2016.11.142. URL: http://dx.doi.org/10.1016/j.egypro.2016.11.142.

[56] M. Niederkrüger, D. Steiner, and E.-U. Schlünder. "Horizontal flow boiling experiments of saturated pure components and mixtures of R846-R12 at high pressures". In: *International Journal of Refrigeration* 15.1 (1992), pp. 48–58. ISSN: 0140-7007. DOI: https://doi.org/10.1016/0140-7007(92)90067-5. URL: http://www.sciencedirect.com/science/article/pii/0140700792900675.

[57] Joseph Oyekale et al. "Thermo-economic evaluation of actively selected siloxane mixtures in a hybrid solar-biomass organic Rankine cycle power plant". In: *Applied Thermal Engineering* 165.July 2019 (2020), p. 114607. ISSN: 13594311. DOI: 10.1016/j.applthermaleng.2019.114607. URL: https://doi.org/10.1016/j.applthermaleng.2019.114607.

[58] Gholamreza Bamorovat Abadi and Kyung Chun Kim. "Investigation of organic Rankine cycles with zeotropic mixtures as a working fluid: Advantages and issues". In: *Renewable and Sustainable Energy Reviews* 73.April 2016 (2017), pp. 1000–1013. ISSN: 18790690. DOI: 10.

1016/j.rser.2017.02.020. URL: http://dx.doi.org/10.1016/j.rser.2017.02.020.

[59] Xiao Xia Xia et al. "A novel comprehensive evaluation methodology of organic Rankine cycle for parameters design and working fluid selection". In: *Applied Thermal Engineering* 143.July (2018), pp. 283–292. ISSN: 13594311. DOI: 10.1016/j.applthermaleng.2018.07.061.

[60] Shukun Wang et al. "Selection principle of working fluid for organic Rankine cycle based on environmental benefits and economic performance". In: *Applied Thermal Engineering* 178.June (2020), p. 115598. DOI: 10.1016/j.applthermaleng.2020.115598.

[61] Shukun Wang et al. "Carbon footprint analysis of organic rankine cycle system using zeotropic mixtures considering leak of fluid". In: *Journal of Cleaner Production* 239 (2019), p. 118095. ISSN: 09596526. DOI: 10.1016/j.jclepro.2019.118095. URL: https://doi.org/10.1016/j.jclepro.2019.118095.

[62] Gequn Shu et al. "Scan of working fluids based on dynamic response characters for Organic Rankine Cycle using for engine waste heat recovery". In: *Energy* 133 (2017), pp. 609–620. ISSN: 03605442. DOI: 10.1016/j.energy.2017.05.003. URL: http://dx.doi.org/10.1016/j.energy.2017.05.003.

[63] Martin White and Abdulnaser I. Sayma. "Improving the economy-of-scale of small organic rankine cycle systems through appropriate working fluid selection". In: *Applied Energy* 183 (2016), pp. 1227–1239. ISSN: 03062619. DOI: 10.1016/j.apenergy.2016.09.055. URL: http://dx.doi.org/10.1016/j.apenergy.2016.09.055.

[64] Rémi Dickes et al. "Charge-sensitive modelling of organic Rankine cycle power systems for off-design performance simulation". In: *Applied Energy* 212.December 2017 (2018), pp. 1262–1281. ISSN: 03062619. DOI: 10.1016/j.apenergy.2018.01.004. URL: https://doi.org/10.1016/j.apenergy.2018.01.004.

[65] Rémi Dickes, Olivier Dumont, and Vincent Lemort. "Experimental assessment of the fluid charge distribution in an organic Rankine cycle (ORC) power system". In: *Applied Thermal Engineering* 179.June (2020), p. 115689. ISSN: 13594311. DOI: 10.1016/j.applthermaleng.

2020.115689. URL: https://doi.org/10.1016/j.applthermaleng.2020.115689.

[66] Sylvain Quoilin et al. "Thermo-economic optimization of waste heat recovery Organic Rankine Cycles". In: *Applied Thermal Engineering* 31.14-15 (2011), pp. 2885–2893. ISSN: 13594311. DOI: 10.1016/j.applthermaleng.2011.05.014. URL: http://dx.doi.org/10.1016/j.applthermaleng.2011.05.014.

[67] Davide Di Battista et al. "On the limiting factors of the waste heat recovery via ORC-based power units for on-the-road transportation sector". In: *Energy Conversion and Management* 155.October 2017 (2018), pp. 68–77. ISSN: 01968904. DOI: 10.1016/j.enconman.2017.10.091. URL: https://doi.org/10.1016/j.enconman.2017.10.091.

[68] Muhammad Usman et al. "Impact of organic Rankine cycle system installation on light duty vehicle considering both positive and negative aspects". In: *Energy Conversion and Management* 112 (2016), pp. 382–394. ISSN: 01968904. DOI: 10.1016/j.enconman.2016.01.044. URL: http://dx.doi.org/10.1016/j.enconman.2016.01.044.

[69] Behrooz Mashadi, Amirhasan Kakaee, and Ahmad Jafari Horestani. "Low-temperature Rankine cycle to increase waste heat recovery from the internal combustion engine cooling system". In: *Energy Conversion and Management* 182.September 2018 (2019), pp. 451–460. ISSN: 01968904. DOI: 10.1016/j.enconman.2018.12.010. URL: https://doi.org/10.1016/j.enconman.2018.12.010.

[70] Fubin Yang et al. "Parametric optimization and performance analysis of ORC (organic Rankine cycle) for diesel engine waste heat recovery with a fin-and-tube evaporator". In: *Energy* 91 (2015), pp. 128–141. ISSN: 03605442. DOI: 10.1016/j.energy.2015.08.034. URL: http://dx.doi.org/10.1016/j.energy.2015.08.034.

[71] Chinedu K. Unamba et al. "Experimental Investigation of the Operating Point of a 1-kW ORC System". In: *Energy Procedia* 129 (2017), pp. 875–882. ISSN: 18766102. DOI: 10.1016/j.egypro.2017.09.211. URL: http://dx.doi.org/10.1016/j.egypro.2017.09.211.

[72] Muhammad Usman et al. "Experimental analysis of a micro-scale organic Rankine cycle system retrofitted to operate in grid-connected mode". In: *Applied Thermal Engineering* 180.March (2020), p. 115889. ISSN: 13594311. DOI: 10.1016/j.applthermaleng.2020.115889. URL: https://doi.org/10.1016/j.applthermaleng.2020.115889.

[73] Gholamreza Bamorovat Abadi, Eunkoo Yun, and Kyung Chun Kim. "Experimental study of a 1 kw organic Rankine cycle with a zeotropic mixture of R245fa/R134a". In: *Energy* 93 (2015), pp. 2363–2373. ISSN: 03605442. DOI: 10.1016/j.energy.2015.10.092. URL: http://dx.doi.org/10.1016/j.energy.2015.10.092.

[74] Eunkoo Yun et al. "Experimental investigation of an organic Rankine cycle with multiple expanders used in parallel". In: *Applied Energy* 145 (2015), pp. 246–254. ISSN: 03062619. DOI: 10.1016/j.apenergy.2015.02.022. URL: http://dx.doi.org/10.1016/j.apenergy.2015.02.022.

[75] J. Galindo et al. "Experimental and thermodynamic analysis of a bottoming Organic Rankine Cycle (ORC) of gasoline engine using swash-plate expander". In: *Energy Conversion and Management* 103 (2015), pp. 519–532. ISSN: 01968904. DOI: 10.1016/j.enconman.2015.06.085. URL: http://dx.doi.org/10.1016/j.enconman.2015.06.085.

[76] Liuchen Liu et al. "Experimental investigation on the effect of working fluid charge in a small-scale Organic Rankine Cycle under off-design conditions". In: *Energy* 174 (2019), pp. 664–677. ISSN: 03605442. DOI: 10.1016/j.energy.2019.03.013. URL: https://doi.org/10.1016/j.energy.2019.03.013.

[77] Rémi Dickes et al. "Modelling of organic Rankine cycle power systems in off-design conditions: An experimentally-validated comparative study". In: *Energy* 123 (2017), pp. 710–727. ISSN: 03605442. DOI: 10.1016/j.energy.2017.01.130.

[78] Steven Lecompte et al. "Experimental results of a small-scale organic Rankine cycle: Steady state identification and application to off-design model validation". In: *Applied Energy* 226.May (2018), pp. 82–106. ISSN: 03062619. DOI: 10.1016/j.apenergy.2018.05.103. URL: https://doi.org/10.1016/j.apenergy.2018.05.103.

[79] Fuhaid Alshammari and Apostolos Pesyridis. "Experimental study of organic Rankine cycle system and expander performance for heavy-duty diesel engine". In: *Energy Conversion and Management* 199.June (2019), p. 111998. ISSN: 01968904. DOI: 10.1016/j.enconman.2019.111998. URL: https://doi.org/10.1016/j.enconman.2019.111998.

[80] Antti Uusitalo, Juha Honkatukia, and Teemu Turunen-Saaresti. "Evaluation of a small-scale waste heat recovery organic Rankine cycle". In: *Applied Energy* 192 (2017), pp. 146–158. ISSN: 03062619. DOI: 10.1016/j.apenergy.2017.01.088. URL: http://dx.doi.org/10.1016/j.apenergy.2017.01.088.

[81] Davide Di Battista, Marco Mauriello, and Roberto Cipollone. "Effects of an ORC Based Heat Recovery System on the Performances of a Diesel Engine". In: *SAE Technical Papers* 2015-April.April (2015). ISSN: 01487191. DOI: 10.4271/2015-01-1608.

[82] Ludovic Guillaume and Vincent Lemort. "Comparison of different ORC typologies for heavy-duty trucks by means of a thermo-economic optimization". In: *Energy* 182 (2019), pp. 706–728. ISSN: 03605442. DOI: 10.1016/j.energy.2019.05.195. URL: https://doi.org/10.1016/j.energy.2019.05.195.

[83] Bin Xu et al. "Power Maximization of a Heavy Duty Diesel Organic Rankine Cycle Waste Heat Recovery System Utilizing Mechanically Coupled and Fully Electrified Turbine Expanders". In: (2016), V001T05A005. DOI: 10.1115/icef2016-9378.

[84] Talus Park et al. "A rankine cycle system for recovering waste heat from HD diesel engines - Experimental results". In: *SAE 2011 World Congress and Exhibition* (2011). ISSN: 2688-3627. DOI: 10.4271/2011-01-1337.

[85] Fubin Yang et al. "Performance analysis of waste heat recovery with a dual loop organic Rankine cycle (ORC) system for diesel engine under various operating conditions". In: *Energy Conversion and Management* 80 (2014), pp. 243–255. ISSN: 01968904. DOI: 10.1016/j.enconman.2014.01.036. URL: http://dx.doi.org/10.1016/j.enconman.2014.01.036.

[86] Enhua Wang et al. "A regenerative supercritical-subcritical dual-loop organic Rankine cycle system for energy recovery from the waste heat of internal combustion engines". In: *Applied Energy* 190 (2017), pp. 574–590. ISSN: 03062619. DOI: 10.1016/j.apenergy.2016.12.122. URL: http://dx.doi.org/10.1016/j.apenergy.2016.12.122.

[87] Gequn Shu et al. "Multi-approach evaluations of a cascade-Organic Rankine Cycle (C-ORC) system driven by diesel engine waste heat: Part A – Thermodynamic evaluations". In: *Energy Conversion and Management* 108 (2016), pp. 579–595. ISSN: 01968904. DOI: 10.1016/j.enconman.2015.10.084. URL: http://dx.doi.org/10.1016/j.enconman.2015.10.084.

[88] Guopeng Yu et al. "Multi-approach evaluations of a cascade-Organic Rankine Cycle (C-ORC) system driven by diesel engine waste heat: Part B-techno-economic evaluations". In: *Energy Conversion and Management* 108 (2016), pp. 596–608. ISSN: 01968904. DOI: 10.1016/j.enconman.2015.10.085. URL: http://dx.doi.org/10.1016/j.enconman.2015.10.085.

[89] Guopeng Yu et al. "Experimental investigations on a cascaded steam-/organic-Rankine-cycle (RC/ORC) system for waste heat recovery (WHR) from diesel engine". In: *Energy Conversion and Management* 129 (2016), pp. 43–51. ISSN: 01968904. DOI: 10.1016/j.enconman.2016.10.010. URL: http://dx.doi.org/10.1016/j.enconman.2016.10.010.

[90] Adriano Desideri et al. "An experimental analysis of flow boiling and pressure drop in a brazed plate heat exchanger for organic Rankine cycle power systems". In: *International Journal of Heat and Mass Transfer* 113 (2017), pp. 6–21. ISSN: 00179310. DOI: 10.1016/j.ijheatmasstransfer.2017.05.063.

[91] Junqi Dong, Xianhui Zhang, and Jianzhang Wang. "Experimental investigation on heat transfer characteristics of plat heat exchanger applied in organic Rankine cycle (ORC)". In: *Applied Thermal Engineering* 112 (2017), pp. 1137–1152. ISSN: 13594311. DOI: 10.1016/j.applthermaleng.2016.10.190. URL: http://dx.doi.org/10.1016/j.applthermaleng.2016.10.190.

[92] Omid Nematollahi et al. "Experimental study of the effect of brazed compact metal-foam evaporator in an organic Rankine cycle performance: Toward a compact ORC". In: *Energy Conversion and Management* 173.June (2018), pp. 37–45. ISSN: 01968904. DOI: 10.1016/j.enconman.2018.07.071. URL: https://doi.org/10.1016/j.enconman.2018.07.071.

[93] Hongchuang Sun et al. "Effect of flow losses in heat exchangers on the performance of organic Rankine cycle". In: *Energy* 172 (2019), pp. 391–400. ISSN: 03605442. DOI: 10.1016/j.energy.2019.01.131. URL: https://doi.org/10.1016/j.energy.2019.01.131.

[94] Xiaoya Li et al. "Organic Rankine cycle systems for engine waste-heat recovery: Heat exchanger design in space-constrained applications". In: *Energy Conversion and Management* 199.August (2019), p. 111968. ISSN: 01968904. DOI: 10.1016/j.enconman.2019.111968. URL: https://doi.org/10.1016/j.enconman.2019.111968.

[95] Mario Holik et al. "Optimization of an organic Rankine cycle constrained by the application of compact heat exchangers". In: *Energy Conversion and Management* 188.March (2019), pp. 333–345. ISSN: 01968904. DOI: 10.1016/j.enconman.2019.03.039.

[96] Manuel Jiménez-Arreola, Christoph Wieland, and Alessandro Romagnoli. "Direct vs indirect evaporation in Organic Rankine Cycle (ORC) systems: A comparison of the dynamic behavior for waste heat recovery of engine exhaust". In: *Applied Energy* 242.February (2019), pp. 439–452. ISSN: 03062619. DOI: 10.1016/j.apenergy.2019.03.011. URL: https://doi.org/10.1016/j.apenergy.2019.03.011.

[97] Muhammad Imran et al. "Dynamic modeling and control strategies of organic Rankine cycle systems: Methods and challenges". In: *Applied Energy* 276.March (2020), p. 115537. ISSN: 03062619. DOI: 10.1016/j.apenergy.2020.115537. URL: https://doi.org/10.1016/j.apenergy.2020.115537.

[98] Francesco Galuppo et al. "Organic Rankine Cycle based waste heat recovery modeling and control of the low pressure side using direct condensation and dedicated fans". In: *Energy* 216 (2021), p. 119074. ISSN: 03605442. DOI: 10.1016/j.energy.2020.119074. URL: https://doi.org/10.1016/j.energy.2020.119074.

[99] Bin Xu et al. "A comparative analysis of dynamic evaporator models for organic Rankine cycle waste heat recovery systems". In: *Applied Thermal Engineering* 165.October 2019 (2020), p. 114576. ISSN: 13594311. DOI: 10.1016/j.applthermaleng.2019.114576. URL: https://doi.org/10.1016/j.applthermaleng.2019.114576.

[100] Liuchen Liu et al. "Numerical predicting the dynamic behavior of heat exchangers for a small-scale Organic Rankine Cycle". In: *Energy Procedia* 129 (2017), pp. 419–426. ISSN: 18766102. DOI: 10.1016/j.egypro.2017.09.127. URL: http://dx.doi.org/10.1016/j.egypro.2017.09.127.

[101] Wolfgang R. Huster et al. "Validated dynamic model of an organic Rankine cycle (ORC) for waste heat recovery in a diesel truck". In: *Energy* 151 (2018), pp. 647–661. ISSN: 03605442. DOI: 10.1016/j.energy.2018.03.058. URL: https://doi.org/10.1016/j.energy.2018.03.058.

[102] Ludovic Guillaume et al. "Performance of a radial-inflow turbine integrated in an ORC system and designed for a WHR on truck application: An experimental comparison between R245fa and R1233zd". In: *Applied Energy* 186 (2017), pp. 408–422. ISSN: 03062619. DOI: 10.1016/j.apenergy.2016.03.012. URL: http://dx.doi.org/10.1016/j.apenergy.2016.03.012.

[103] Long Shao et al. "Experimental study of an organic Rankine cycle system with radial inflow turbine and R123". In: *Applied Thermal Engineering* 124 (2017), pp. 940–947. ISSN: 13594311. DOI: 10.1016/j.applthermaleng.2017.06.042. URL: http://dx.doi.org/10.1016/j.applthermaleng.2017.06.042.

[104] Fuhaid Alshammari et al. "Experimental study of a small scale organic Rankine cycle waste heat recovery system for a heavy duty diesel engine with focus on the radial inflow turbine expander performance". In: *Applied Energy* 215.January (2018), pp. 543–555. ISSN: 03062619. DOI: 10.1016/j.apenergy.2018.01.049. URL: https://doi.org/10.1016/j.apenergy.2018.01.049.

[105] Tomasz Z. Kaczmarczyk, Grzegorz Żywica, and Eugeniusz Ihnatowicz. "Experimental study of a low-temperature micro-scale organic Rankine cycle system with the multi-stage radial-flow turbine for do-

mestic applications". In: *Energy Conversion and Management* 199.May (2019). ISSN: 01968904. DOI: 10.1016/j.enconman.2019.111941.

[106] Hongchuang Sun et al. "Performance evaluation of a partially admitted axial turbine using R245fa, R123 and their mixtures as working fluid for small-scale organic Rankine cycle". In: *Energy Conversion and Management* 171.92 (2018), pp. 925–935. ISSN: 01968904. DOI: 10.1016/j.enconman.2018.06.048. URL: https://doi.org/10.1016/j.enconman.2018.06.048.

[107] Hongchuang Sun et al. "Performance analysis of low speed axial impulse turbine using two type nozzles for small-scale organic Rankine cycle". In: *Energy* 169 (2019), pp. 1139–1152. ISSN: 03605442. DOI: 10.1016/j.energy.2018.12.091. URL: https://doi.org/10.1016/j.energy.2018.12.091.

[108] Davide Di Battista and Roberto Cipollone. "Experimental analysis of an organic rankine cycle plant bottoming a heavy-duty engine using axial turbine as prime mover". In: *SAE International Journal of Engines* 10.4 (2017), pp. 1385–1397. ISSN: 19463944. DOI: 10.4271/2017-01-9279.

[109] Andreas P. Weiß et al. "Experimental characterization and comparison of an axial and a cantilever micro-turbine for small-scale Organic Rankine Cycle". In: *Applied Thermal Engineering* 140.January (2018), pp. 235–244. ISSN: 13594311. DOI: 10.1016/j.applthermaleng.2018.05.033. URL: https://doi.org/10.1016/j.applthermaleng.2018.05.033.

[110] Lorenzo Talluri et al. "Experimental investigation of an Organic Rankine Cycle Tesla turbine working with R1233zd(E)". In: *Applied Thermal Engineering* 174.February (2020), p. 115293. ISSN: 13594311. DOI: 10.1016/j.applthermaleng.2020.115293. URL: https://doi.org/10.1016/j.applthermaleng.2020.115293.

[111] Fabio Pantano and Roberto Capata. "Expander selection for an on board ORC energy recovery system". In: *Energy* 141 (2017), pp. 1084–1096. ISSN: 03605442. DOI: 10.1016/j.energy.2017.09.142. URL: https://doi.org/10.1016/j.energy.2017.09.142.

[112] Adriano Desideri et al. "Experimental campaign and modeling of a low-capacity waste heat recovery system based on a single screw expander". In: *22nd International Compressor Engineering Conference at Purdue* 2011 (2014), pp. 1–10. URL: http://docs.lib.purdue.edu/icec/2345/.

[113] Biao Lei et al. "Development and experimental study on a single screw expander integrated into an Organic Rankine Cycle". In: *Energy* 116 (2016), pp. 43–52. ISSN: 03605442. DOI: 10.1016/j.energy.2016.09.089. URL: http://dx.doi.org/10.1016/j.energy.2016.09.089.

[114] D. Ziviani et al. "Characterizing the performance of a single-screw expander in a small-scale organic Rankine cycle for waste heat recovery". In: *Applied Energy* 181 (2016), pp. 155–170. ISSN: 03062619. DOI: 10.1016/j.apenergy.2016.08.048. URL: http://dx.doi.org/10.1016/j.apenergy.2016.08.048.

[115] D. Ziviani et al. "Optimizing the performance of small-scale organic Rankine cycle that utilizes a single-screw expander". In: *Applied Energy* 189 (2017), pp. 416–432. ISSN: 03062619. DOI: 10.1016/j.apenergy.2016.12.070. URL: http://dx.doi.org/10.1016/j.apenergy.2016.12.070.

[116] D. Ziviani et al. "Comparison of a single-screw and a scroll expander under part-load conditions for low-grade heat recovery ORC systems". In: *Energy Procedia* 61 (2014), pp. 117–120. ISSN: 18766102. DOI: 10.1016/j.egypro.2014.11.920.

[117] Antonio Giuffrida. "Improving the semi-empirical modelling of a single-screw expander for small organic Rankine cycles". In: *Applied Energy* 193 (2017), pp. 356–368. ISSN: 03062619. DOI: 10.1016/j.apenergy.2017.02.015. URL: http://dx.doi.org/10.1016/j.apenergy.2017.02.015.

[118] Alexander Nikolov and Andreas Brümmer. "Investigating a small oil-flooded twin-screw expander for waste-heat utilisation in organic rankine cycle systems". In: *Energies* 10.7 (2017). ISSN: 19961073. DOI: 10.3390/en10070869.

[119] Ye Qiang Zhang et al. "Development and experimental study on organic Rankine cycle system with single-screw expander for waste heat

recovery from exhaust of diesel engine". In: *Energy* 77 (2014), pp. 499–508. ISSN: 03605442. DOI: 10.1016/j.energy.2014.09.034. URL: http://dx.doi.org/10.1016/j.energy.2014.09.034.

[120] Xu Ping et al. "Prediction and optimization of power output of single screw expander in organic Rankine cycle (ORC) for diesel engine waste heat recovery". In: *Applied Thermal Engineering* 182.100 (2021), p. 116048. ISSN: 13594311. DOI: 10.1016/j.applthermaleng.2020.116048. URL: https://doi.org/10.1016/j.applthermaleng.2020.116048.

[121] Iva Papes, Joris Degroote, and Jan Vierendeels. "New insights in twin screw expander performance for small scale ORC systems from 3D CFD analysis". In: *Applied Thermal Engineering* 91 (2015), pp. 535–546. ISSN: 13594311. DOI: 10.1016/j.applthermaleng.2015.08.034. URL: http://dx.doi.org/10.1016/j.applthermaleng.2015.08.034.

[122] Giuseppe Bianchi et al. "Two-phase chamber modeling of a twin-screw expander for Trilateral Flash Cycle applications". In: *Energy Procedia* 129 (2017), pp. 347–354. ISSN: 18766102. DOI: 10.1016/j.egypro.2017.09.208. URL: http://dx.doi.org/10.1016/j.egypro.2017.09.208.

[123] Giuseppe Bianchi et al. "Numerical modeling of a two-phase twin-screw expander for Trilateral Flash Cycle applications". In: *International Journal of Refrigeration* 88 (2018), pp. 248–259. ISSN: 01407007. DOI: 10.1016/j.ijrefrig.2018.02.001. URL: https://doi.org/10.1016/j.ijrefrig.2018.02.001.

[124] Panpan Song et al. "A review of scroll expanders for organic rankine cycle systems". In: *Applied Thermal Engineering* 75 (2015), pp. 54–64. ISSN: 13594311. DOI: 10.1016/j.applthermaleng.2014.05.094. URL: http://dx.doi.org/10.1016/j.applthermaleng.2014.05.094.

[125] Simon Emhardt, Guohong Tian, and John Chew. "A review of scroll expander geometries and their performance". In: *Applied Thermal Engineering* 141.June (2018), pp. 1020–1034. ISSN: 13594311. DOI: 10.1016/j.applthermaleng.2018.06.045. URL: https://doi.org/10.1016/j.applthermaleng.2018.06.045.

[126] Claudio Campana et al. "Experimental analysis of a small-scale scroll expander for low-temperature waste heat recovery in Organic Rankine Cycle". In: *Energy* 187 (2019), p. 115929. ISSN: 03605442. DOI: 10.1016/j.energy.2019.115929. URL: https://doi.org/10.1016/j.energy.2019.115929.

[127] Davide Ziviani et al. "Experimental and numerical analyses of a 5 kWe oil-free open-drive scroll expander for small-scale organic Rankine cycle (ORC) applications". In: *Applied Energy* 230.September (2018), pp. 1140–1156. ISSN: 03062619. DOI: 10.1016/j.apenergy.2018.09.025. URL: https://doi.org/10.1016/j.apenergy.2018.09.025.

[128] Tomasz Z. Kaczmarczyk, Grzegorz Żywica, and Eugeniusz Ihnatowicz. "Experimental research on scroll expanders operating in parallel in an organic Rankine cycle system with a biomass boiler". In: *Energy Conversion and Management* 224.May (2020). ISSN: 01968904. DOI: 10.1016/j.enconman.2020.113390.

[129] Zheng Miao, Jinliang Xu, and Kai Zhang. "Experimental and modeling investigation of an organic Rankine cycle system based on the scroll expander". In: *Energy* 134 (2017), pp. 35–49. ISSN: 03605442. DOI: 10.1016/j.energy.2017.06.001. URL: http://dx.doi.org/10.1016/j.energy.2017.06.001.

[130] Jie Zhu et al. "Effect of resistive load on the performance of an organic Rankine cycle with a scroll expander". In: *Energy* 95 (2016), pp. 21–28. ISSN: 03605442. DOI: 10.1016/j.energy.2015.11.048. URL: http://dx.doi.org/10.1016/j.energy.2015.11.048.

[131] Sébastien Declaye et al. "Experimental study on an open-drive scroll expander integrated into an ORC (Organic Rankine Cycle) system with R245fa as working fluid". In: *Energy* 55 (2013), pp. 173–183. ISSN: 03605442. DOI: 10.1016/j.energy.2013.04.003. URL: http://dx.doi.org/10.1016/j.energy.2013.04.003.

[132] Sylvain Quoilin, Vincent Lemort, and Jean Lebrun. "Experimental study and modeling of an Organic Rankine Cycle using scroll expander". In: *Applied Energy* 87.4 (2010), pp. 1260–1268. ISSN: 03062619. DOI: 10.1016/j.apenergy.2009.06.026. URL: http://dx.doi.org/10.1016/j.apenergy.2009.06.026.

[133] Gabriel Rossi Fanti et al. "Influence of flank clearance on the performance of a scroll expander prototype". In: *Energy* 193 (2020). ISSN: 03605442. DOI: 10.1016/j.energy.2019.116823.

[134] Vincent Lemort et al. "Testing and modeling a scroll expander integrated into an Organic Rankine Cycle". In: *Applied Thermal Engineering* 29.14-15 (2009), pp. 3094–3102. ISSN: 13594311. DOI: 10.1016/j.applthermaleng.2009.04.013. URL: http://dx.doi.org/10.1016/j.applthermaleng.2009.04.013.

[135] Cagri Kutlu et al. "Evaluate the validity of the empirical correlations of clearance and friction coefficients to improve a scroll expander semi-empirical model". In: *Energy* 202 (2020), p. 117723. ISSN: 03605442. DOI: 10.1016/j.energy.2020.117723. URL: https://doi.org/10.1016/j.energy.2020.117723.

[136] Antonio Giuffrida. "A theoretical study on the performance of a scroll expander in an organic Rankine cycle with hydrofluoroolefins (HFOs) in place of R245fa". In: *Energy* 161 (2018), pp. 1172–1180. ISSN: 03605442. DOI: 10.1016/j.energy.2018.07.146. URL: https://doi.org/10.1016/j.energy.2018.07.146.

[137] Jinwoo Oh et al. "Numerical and experimental investigation on thermal-hydraulic characteristics of a scroll expander for organic Rankine cycle". In: *Applied Energy* 278.July (2020), p. 115672. ISSN: 03062619. DOI: 10.1016/j.apenergy.2020.115672. URL: https://doi.org/10.1016/j.apenergy.2020.115672.

[138] A. Legros et al. *Investigation on a scroll expander for waste heat recovery on internal combustion engines*. Woodhead Publishing Limited, 2013, pp. 453–463. ISBN: 9781782421696. DOI: 10.1533/9781782421702.8.453. URL: http://dx.doi.org/10.1533/9781782421696.8.453.

[139] Jen Chieh Chang et al. "Experimental study and CFD approach for scroll type expander used in low-temperature organic Rankine cycle". In: *Applied Thermal Engineering* 73.2 (2014), pp. 1444–1452. ISSN: 13594311. DOI: 10.1016/j.applthermaleng.2014.08.050. URL: http://dx.doi.org/10.1016/j.applthermaleng.2014.08.050.

[140] Simon Emhardt et al. "CFD modelling of small scale ORC scroll expanders using variable wall thicknesses". In: *Energy* 199 (2020),

p. 117399. ISSN: 03605442. DOI: 10.1016/j.energy.2020.117399. URL: https://doi.org/10.1016/j.energy.2020.117399.

[141] Mingshan Wei et al. "Unsteady flow in the suction process of a scroll expander for an ORC waste heat recovery system". In: *Applied Thermal Engineering* 78 (2015), pp. 460–470. ISSN: 13594311. DOI: 10.1016/j.applthermaleng.2015.01.010. URL: http://dx.doi.org/10.1016/j.applthermaleng.2015.01.010.

[142] O. Badr, P.W. O'Callaghan, and S.D. Probert. "Multi-vane expanders: Geometry and vane kinematics". In: *Applied Energy* 19.3 (1985), pp. 159–182. ISSN: 0306-2619. DOI: https://doi.org/10.1016/0306-2619(85)90006-6. URL: http://www.sciencedirect.com/science/article/pii/0306261985900066.

[143] O. Badr, P.W. O'Callaghan, and S.D. Probert. "Multi-vane expander performance: Breathing characteristics". In: *Applied Energy* 19.4 (1985), pp. 241–271. ISSN: 0306-2619. DOI: https://doi.org/10.1016/0306-2619(85)90001-7. URL: http://www.sciencedirect.com/science/article/pii/0306261985900017.

[144] O. Badr, S.D. Probert, and P. O'Callaghan. "Multi-vane expanders: Vane dynamics and friction losses". In: *Applied Energy* 20.4 (1985), pp. 253–285. ISSN: 0306-2619. DOI: https://doi.org/10.1016/0306-2619(85)90018-2. URL: http://www.sciencedirect.com/science/article/pii/0306261985900182.

[145] O. Badr, S.D. Probert, and P.W. O'Callaghan. "Influences of vane design and lubricant on a multi-vane expander's performance". In: *Applied Energy* 22.4 (1986), pp. 271–298. ISSN: 0306-2619. DOI: https://doi.org/10.1016/0306-2619(86)90038-3. URL: http://www.sciencedirect.com/science/article/pii/0306261986900383.

[146] O. Badr, D. Probert, and P.W. O'Callaghan. "Selection of operating conditions and optimisation of design parameters for multi-vane expanders". In: *Applied Energy* 23.1 (1986), pp. 1–46. ISSN: 0306-2619. DOI: https://doi.org/10.1016/0306-2619(86)90049-8. URL: http://www.sciencedirect.com/science/article/pii/0306261986900498.

[147] O. Badr, S.D. Probert, and P.W. O'Callaghan. "Optimal design and operating conditions for a multi-vane expander". In: *Applied Energy* 24.1 (1986), pp. 1–27. ISSN: 0306-2619. DOI: https://doi.org/10.1016/0306-2619(86)90043-7. URL: http://www.sciencedirect.com/science/article/pii/0306261986900437.

[148] Piotr Kolasiński, Przemysław Błasiak, and Józef Rak. "Experimental investigation on multi-vane expander operating conditions in domestic CHP ORC system". In: *Energy Procedia* 129 (2017), pp. 323–330. ISSN: 18766102. DOI: 10.1016/j.egypro.2017.09.201. URL: http://dx.doi.org/10.1016/j.egypro.2017.09.201.

[149] Jakub Mascuch et al. "Experimental development of a kilowatt-scale biomass fired micro – CHP unit based on ORC with rotary vane expander". In: *Renewable Energy* 147 (2020), pp. 2882–2895. ISSN: 18790682. DOI: 10.1016/j.renene.2018.08.113. URL: https://doi.org/10.1016/j.renene.2018.08.113.

[150] Stefano Murgia et al. "Experimental investigation into an ORC-based low-grade energy recovery system equipped with sliding-vane expander using hot oil from an air compressor as thermal source". In: *Energy Procedia* 129 (2017), pp. 339–346. ISSN: 18766102. DOI: 10.1016/j.egypro.2017.09.204. URL: http://dx.doi.org/10.1016/j.egypro.2017.09.204.

[151] Stefano Murgia et al. "Optimization of sliding-vane expanders for a low-enthalpy ORC energy recovery system". In: *IOP Conference Series: Materials Science and Engineering* 604.1 (2019). ISSN: 1757899X. DOI: 10.1088/1757-899X/604/1/012042.

[152] Roberto Cipollone et al. "Mechanical energy recovery from low grade thermal energy sources". In: *Energy Procedia* 45 (2014), pp. 121–130. ISSN: 18766102. DOI: 10.1016/j.egypro.2014.01.014. URL: http://dx.doi.org/10.1016/j.egypro.2014.01.014.

[153] Worakit Suankramdee, Tongchana Thongtip, and Satha Aphornratana. "Experimental study of a sliding vane expander in a micro-scale ORC system for utilizing low-grade heat". In: *Energy Procedia* 138 (2017), pp. 823–828. ISSN: 18766102. DOI: 10.1016/j.egypro.2017.10.085. URL: https://doi.org/10.1016/j.egypro.2017.10.085.

[154] Worakit Suankramdee, Tongchana Thongtip, and Satha Aphornratana. "Development of a sliding vane expander in a micro-scale ORC system for utilizing low-grade heat". In: *Energy Procedia* 138 (2017), pp. 817–822. ISSN: 18766102. DOI: 10.1016/j.egypro.2017.10.078. URL: https://doi.org/10.1016/j.egypro.2017.10.078.

[155] Giuseppe Bianchi et al. "Numerical CFD simulations on a small-scale ORC expander using a customized grid generation methodology". In: *Energy Procedia* 129 (2017), pp. 843–850. ISSN: 18766102. DOI: 10.1016/j.egypro.2017.09.199. URL: http://dx.doi.org/10.1016/j.egypro.2017.09.199.

[156] Gianluca Montenegro et al. "Evaluating the performance of a rotary vane expander for small scale organic rankine cycles using CFD tools". In: *Energy Procedia* 45 (2014), pp. 1136–1145. ISSN: 18766102. DOI: 10.1016/j.egypro.2014.01.119. URL: http://dx.doi.org/10.1016/j.egypro.2014.01.119.

[157] Fanghua Ye, Jianqiang Deng, and Kai Liu. "CFD simulation on cavitation in a rotary vane energy recovery device". In: *Energy Procedia* 158 (2019), pp. 4785–4790. ISSN: 18766102. DOI: 10.1016/j.egypro.2019.01.720. URL: https://doi.org/10.1016/j.egypro.2019.01.720.

[158] Vaclav Vodicka et al. "Impact of major leakages on characteristics of a rotary vane expander for ORC". In: *Energy Procedia* 129 (2017), pp. 387–394. ISSN: 18766102. DOI: 10.1016/j.egypro.2017.09.249. URL: http://dx.doi.org/10.1016/j.egypro.2017.09.249.

[159] Vaclav Vodicka et al. "Theoretical and experimental investigations on the radial and axial leakages within a rotary vane expander". In: *Energy* 189 (2019), p. 116097. ISSN: 03605442. DOI: 10.1016/j.energy.2019.116097. URL: https://doi.org/10.1016/j.energy.2019.116097.

[160] Fabio Fatigati, Marco Di Bartolomeo, and Roberto Cipollone. "On the effects of leakages in Sliding Rotary Vane Expanders". In: *Energy* 192 (2020), p. 116721. ISSN: 03605442. DOI: 10.1016/j.energy.2019.116721. URL: https://doi.org/10.1016/j.energy.2019.116721.

[161] Jiayao Yan et al. "Performance investigation of a novel expander coupling organic Rankine cycle: Variable expansion ratio rotary vane expander for variable working conditions". In: *Applied Thermal Engineering* 152.December 2018 (2019), pp. 573–581. ISSN: 13594311. DOI: 10.1016/j.applthermaleng.2019.02.103. URL: https://doi.org/10.1016/j.applthermaleng.2019.02.103.

[162] Fabio Fatigati, Giuseppe Bianchi, and Roberto Cipollone. "Development and numerical modelling of a supercharging technique for positive displacement expanders". In: *Applied Thermal Engineering* 140.May (2018), pp. 208–216. ISSN: 13594311. DOI: 10.1016/j.applthermaleng.2018.05.046. URL: https://doi.org/10.1016/j.applthermaleng.2018.05.046.

[163] Fabio Fatigati, Marco Di Bartolomeo, and Roberto Cipollone. "Experimental and numerical characterization of a positive displacement vane expander with an auxiliary injection port for an ORC-based power unit". In: *Energy Procedia* 148 (2018), pp. 830–837. ISSN: 18766102. DOI: 10.1016/j.egypro.2018.08.114. URL: https://doi.org/10.1016/j.egypro.2018.08.114.

[164] Fabio Fatigati, Marco Di Bartolomeo, and Roberto Cipollone. "Dual intake rotary vane expander technology: Experimental and theoretical assessment". In: *Energy Conversion and Management* 186.March (2019), pp. 156–167. ISSN: 01968904. DOI: 10.1016/j.enconman.2019.02.026. URL: https://doi.org/10.1016/j.enconman.2019.02.026.

[165] Jorrit Wronski et al. "Experimental and numerical analysis of a reciprocating piston expander with variable valve timing for small-scale organic Rankine cycle power systems". In: *Applied Energy* 247.March (2019), pp. 403–416. ISSN: 03062619. DOI: 10.1016/j.apenergy.2019.04.028. URL: https://doi.org/10.1016/j.apenergy.2019.04.028.

[166] Jian Li et al. "Performance analysis of a single-piston free piston expander-linear generator with intake timing control strategy based on piston displacement". In: *Applied Thermal Engineering* 152.100 (2019), pp. 751–761. ISSN: 13594311. DOI: 10.1016/j.applthermaleng.

2019.02.121. URL: https://doi.org/10.1016/j.applthermaleng.2019.02.121.

[167] Xin Shi et al. "Analysis on operation characteristic and output performance of free piston expander-linear generator based on displacement control strategy". In: *Applied Thermal Engineering* 182.August 2020 (2021), p. 116146. ISSN: 13594311. DOI: 10.1016/j.applthermaleng.2020.116146. URL: https://doi.org/10.1016/j.applthermaleng.2020.116146.

[168] Fubin Yang et al. "Experimental study and artificial neural network based prediction of a free piston expander-linear generator for small scale organic Rankine cycle". In: *Energy* 175 (2019), pp. 630–644. ISSN: 03605442. DOI: 10.1016/j.energy.2019.03.099. URL: https://doi.org/10.1016/j.energy.2019.03.099.

[169] S. Gusev et al. "Variable volume ratio free-piston expander: Prototyping and experimental campaign". In: *International Journal of Refrigeration* 98 (2019), pp. 70–79. ISSN: 01407007. DOI: 10.1016/j.ijrefrig.2018.10.004. URL: https://doi.org/10.1016/j.ijrefrig.2018.10.004.

[170] Yongqiang Han et al. "Experimental study and energy loss analysis of an R245fa organic Rankine cycle prototype system with a radial piston expander". In: *Applied Thermal Engineering* 169.December 2019 (2020), p. 114939. ISSN: 13594311. DOI: 10.1016/j.applthermaleng.2020.114939. URL: https://doi.org/10.1016/j.applthermaleng.2020.114939.

[171] M. Bianchi et al. "Performance prediction of a reciprocating piston expander with semi-empirical models". In: *Energy Procedia* 158 (2019), pp. 1737–1743. ISSN: 18766102. DOI: 10.1016/j.egypro.2019.01.403. URL: https://doi.org/10.1016/j.egypro.2019.01.403.

[172] M. Bianchi et al. "Application and comparison of semi-empirical models for performance prediction of a kW-size reciprocating piston expander". In: *Applied Energy* 249.January (2019), pp. 143–156. ISSN: 03062619. DOI: 10.1016/j.apenergy.2019.04.070. URL: https://doi.org/10.1016/j.apenergy.2019.04.070.

[173] A. M. Pantaleo et al. "Thermoeconomic optimisation of small-scale organic Rankine cycle systems based on screw vs. piston expander maps in waste heat recovery applications". In: *Energy Conversion and Management* 200.May (2019), p. 112053. ISSN: 01968904. DOI: 10.1016/j.enconman.2019.112053. URL: https://doi.org/10.1016/j.enconman.2019.112053.

[174] Olivier Dumont et al. "Experimental investigation and optimal performance assessment of four volumetric expanders (scroll, screw, piston and roots) tested in a small-scale organic Rankine cycle system". In: *Energy* 165 (2018), pp. 1119–1127. ISSN: 03605442. DOI: 10.1016/j.energy.2018.06.182.